NTNU

Norwegian University of
Science and Technology

Numerical Simulation of Viscous Flow Past A Curved Cylinder

Christoffer Skjulstad

Marine Technology
Submission date: June 2018
Supervisor: Bjørnar Pettersen, IMT
Co-supervisor: Fengjiang Jiang, IMT

Norwegian University of Science and Technology
Department of Marine Technology

MASTER'S THESIS IN MARINE HYDRODYNAMICS

SPRING 2018

FOR

Stud.techn. Christoffer Skjulstad

NUMERICAL SIMULATION OF VISCOUS FLOW PAST CURVED CYLINDERS

Background There exist detailed results from Direct Numerical Simulation (DNS) studies of wake flow behind curved circular cylinders with another software tool (MGLET). Investigation of how the simulation tool OpenFOAM handles similar flow problems is of interest.

Objective The candidate shall use the same flow parameters and compare results from the two simulation tools.

Scope of Work

- The candidate shall investigate viscous flow around a curved circular cylinder using numerical simulation with OpenFOAM.
- Focus of the study shall be on the near wake flow details. The results obtained should be discussed. Proper visualization of results are important.
- With OpenFOAM, the effect of shear current inflow shall be demonstrated.
- The candidate's choice of flow parameters should be argued for. Computational parameters shall be investigated and documented. The proper parameters and detailed settings of the numerical simulations (including pre- and post-processing) should be documented for later use.

Presentation of the Work

In the thesis the candidate shall present his personal contribution to the resolution of the problem within the scope of the thesis work. Theories and conclusions should be based on mathematical derivation and logic reasoning identifying the various steps in the deduction. The original contribution of the candidate and material taken from other sources shall be clearly defined. Work from other

sources shall be properly referenced. The candidate should utilize the existing possibilities for obtaining relevant literature.

The thesis should be organized in a rational manner to give a clear exposition of results, assessments and conclusions. The text should be brief and to the point, with a clear language.

The thesis shall contain the following elements: A text defining the scope, preface, list of contents, summary, main body of thesis, conclusions with recommendations for further work, list of symbols and acronyms, references and appendices. All figures, tables and equations shall be numerated.

It is supposed that Department of Marine Technology, NTNU, can use the results freely in its research work by referring to the student's thesis.

The thesis shall be submitted June 25th, 2018, in two copies.

Bjørnar Pettersen
Professor/supervisor

Co-supervisor: Postdoc Fengjian Jiang

Preface

This Master Thesis is a presentation of my work conducted in the spring of 2018 as a part of my M.Sc. degree in Marine Hydrodynamics from the Department of Marine Technology at the Norwegian University of Science and Technology NTNU. The present work is a follow up of a project thesis carried out in the fall of 2017.

My personal goal for this thesis was to get familiar with practical computational fluid dynamics (CFD) as I find the exploration of fluid flow quite intriguing. The choice of using the third party open source CFD code OpenFOAM let me focus on the complex three-dimensional flow past a curved circular cylinder in various flow conditions. The open source code and minimalistic user interface ensures that one has complete control over what the program is doing and so it is good for academic research, however also a great learning tool for me as a beginner in CFD.

The work has been challenging at times, but it has taught me a lot about numerical research, both its limitations and also its many possibilities, about working with large data sets and about the complex nature of fluid flow. In addition the construction of a scientific report has proven to be more demanding than anticipated.

Trondheim, June 25, 2018

Christoffer Skjulstad.

Blank Page

Acknowledgements

I would like to express my deepest gratitude to my supervisor Professor Bjørnar Pettersen and my co-supervisor Postdoc. Fengjian Jiang at NTNU for our regular and always motivating meetings, and superb guidance on this subject during the semester. I would like to thank Associate Professor Håvard Holm and research fellow Håkon Strandenes for practical guidance on CFD and practical use of computational resources.

Further I want to thank fellow student from the Department of Computer Science NTNU Håvard Ola Eggen for kindly lending me a server to play with during this semester.

The work has also received support from the Research Council of Norway (Program for Supercomputing, under project nn9191k) through a grant of computing time. Without parallel computing this study would not have been possible.

Last, but not least, I want to thank all the guys in office A1.007 at Tyholt for excellent company throughout this last year of our studies and the guys in A2.025 for providing fresh quality coffee.

Blank Page

Summary

In the present Master thesis three-dimensional viscous flow simulations of flow past a curved circular cylinder is investigated by utilization of the open source Computational Fluid Dynamics (CFD) code OpenFOAM. The focus of the present study has been to establish a basic setup for analysing the curved cylinder flow problem in OpenFOAM by verification with recent unpublished Direct Numerical Simulations (DNS) of the same problem.

The geometry considered is defined by three parts; a curved quarter-of-ring cylinder with a radius of curvature of 12.5D, a horizontal straight extension of length 10D and a vertical straight extension of 24D, where D is the cylinder diameter. Straight extension lengths are chosen to eliminate free-end effects according to recent research. The plane of curvature is aligned with the incoming flow and directed towards the concave face of the curved part.

Uniform inflow at $Re = 200$ and 500 is considered and the solution is compared to DNS results by means of analysing near wake flow details. The OpenFOAM solution captures overall wake topology similar to the DNS. Shedding frequencies are close to DNS however reduced slightly due to a stronger spanwise flow. Details in the transitional region around the intersection between the curved and vertical parts for $Re = 500$ are not captured correctly by the present study. Mean and root-mean-square values of drag and lift forces are overpredicted by the OpenFOAM solution. The tendency increases for larger Re and is owed to the relatively low grid resolution near the cylinder compared to DNS.

Three variants of sheared inflow conditions are investigated. A linear shear profile is considered both for positive and negative shear rate with Reynolds number extrema of $Re = 200$ and $Re = 500$. An additional negative shear is considered for extrema of $Re = 700$ and $Re = 200$. Three-dimensionalities in the freestream introduces additional spanwise flow leading to different wake topologies for negative and positive shear. Positive shear exhibits cellular vortex shedding along the vertical extension as seen for straight cylinders in shear flow. Interactions between upwash from the curved part and downwash from shear results in a high-frequency shedding region placed along the span of the vertical extension.

Blank Page

Sammendrag

I denne masteroppgaven utforskes tredimensjonal viskøs strømning rundt en kurvet sirkulær sylinder med diameter D ved hjelp av numerisk strømningsberegning og "open source"-programmet OpenFOAM. Fokuset har vært å etablere en fungerende modell for analyse av en kurvet sylinder for å danne et grunnlag for videre arbeid. Modellen blir verifisert med eksisterende data fra DNS (Direct Numerical Simulation) studier.

Geometrien er definert av en kvartsirkelformet sylinder med konstant krumningsradius $12.5D$ påmontert rette sylinderendestykker der en horisontal del av lengde $10D$ begynner i strømningsinnløpet av beregningsdomenet og en vertikal del av lengde $24D$ ender i øverste ytterpunkt av domenet. Endestykkene skal sørge for at effekter fra grensebetingelser elimineres. Strømningen er parallel med krumningsplanet og rettet mot den konkave flaten av den kurvede delen.

Uniform innstrømning ved Reynoldstall $Re = 200$ og 500 sammenliknes med DNS- resultater i kjølvannet nært sylinderen. Den implementerte modellen fanger opp de generelle trendene i strømningen godt men detaljer blir mer utydelige ved høyere Re. Virvelavløsningsfrekvenser er nære DNS men noe redusert grunnet høyere hastigheter aksielt langsmed sylinderen. Krefter på sylinderen blir overestimert av OpenFOAM-modellen og trenden øker for økende Re, noe som trolig skyldes lav grid-oppløsning nært sylinderen.

Tre varianter av innkommende skjærstrøm presenteres. Lineært varierende skjærstrømsprofiler utbredt i sylinderens vertikale spenn for positiv og negativ skjærrate sammneliknes, samt effekten av sterkere negativ skjærrate. Tredimensjonale effekter i innstrømningen fører til en økning i aksialhastighet langs nedstrømssiden av den vertikale delen for positiv skjærrate. En negativ aksialhastighet langs nedstrømssiden indusert av negativ skjærrate møter den positive aksialstrømmen fra kurven og danner et område langs vertikaldelen med høy virvelavløsningsfrekvens. Høyfrekvensområdet flyttes nedover med økende negativ skjærrate.

Blank Page

Contents

Nomenclature

Abbreviations

CAD Computer Aided Design

CylRefLvl Refinement level in SHM used for approximating the cylinder surface.

ffRefLvl Refinement level in SHM used in the farfield wake region grid.

FLUENT Commercial CFD software by ANSYS

FVM Finite Volume Method

IP Independence Principle.

L Laminar state.

nfRefLvl Refinement level in SHM used in the nearfield wake region grid.

PISO Pressure Implicit with Splitting of Operators

SHM SnappyHexMesh

SIMPLE Semi-Implicit Method for Pressure-Linked Equations.

STAR-CCM+ Commercial CFD software by Siemens

TrSL Transition-in-Shear-Layer.

TrW Transition-in-wake state.

VIV Vortex Induced Vibration.

Symbols

a Wake domain length. Distance from trailing edge of the vertical cylinder to the end of the domain. $[m]$

α Angle of incidence.

A_{ref} Cylinder face area projected in the inflow direction. $[m^2]$

b Distance from bottom of horizontal extension to lower domain boundary. $[m]$

β Angle of non-orthogonality between cells.

c Total computational domain width (along y-axis). $[m]$

C_L Cylinder lift force coefficient. $F_y/\frac{1}{2}\rho U_0^2 S$ $[-]$

$C_{L,rms}$ Root mean square of the cylinder lift force coefficient. $[-]$

$\overline{C_D}$ Mean of the cylinder drag coefficient. $[-]$

C_D Cylinder drag force coefficient. $F_x/\frac{1}{2}\rho U_0^2 S$ $[-]$

Co Courant number.

Co_{mean} Mean Courant number in the domain.

Co_{max} Max Courant number in the domain.

D Cylinder diameter. $[m]$

Δt Finite time step. $[s]$

t^* Non-dimensional time.

Δt^* Non-dimensional finite time step.

$\partial\Omega$ The boundary surface of control volume Ω. $[m^2]$

$\boldsymbol{e_1}$, $\boldsymbol{e_2}$, $\boldsymbol{e_3}$ Unit vectors in standard cartesian coordinate system, for x, y, and z respectively.

$\mathbf{f}$ Acceleration vector of arbitrary volume force on control volume. $[m/s^2]$

F_x Integrated force component on the cylinder in x-direction. $[N]$

F_y Integrated force component on the cylinder in y-direction. $[N]$

f_c^* Non-dimensional frequency based on median inflow velocity. fD/U_c $[-]$

f_{peak}^* Non-dimensional peak frequency obtained in frequency spectrum of lift force. $[-]$

f_l^* Local non-dimensional frequency based on local inflow velocity. $fD/U_0(z)$ $[-]$

f^* Non-dimensional frequency based on free-stream velocity. fD/U_0 $[-]$

h Total domain height. (In introduction: horizontal extension length.) $[m]$

K Non-dimensional shear steepness. $[-]$

Λ Cylinder yaw angle.

L_h Length of horizontal extension. $[m]$

L_{nF} Length (along x-axis) of the nearfield wake grid. $[m]$

L_x, L_y, L_z Domain dimension in each coordinate direction. $[m]$

L_v Height of vertical extension. $[m]$

$\mathbf{n}$ Fluid control volume outward normal vector $[n_1, n_2, n_3]$.

$N_{cellsTot}$ Total number of finite volume cells in the domain.

N_x, N_y, N_z Number of cells in x-, y- and z-direction for the background mesh.

N_{layers} Number of boundary layer elements outwards from the cylinder surface.

Ω A general finite control volume. $[m^3]$

ω Vorticity vector.

P^* Non-dimensional fluid pressure, $P/\rho U_0^2$. $[-]$

P Fluid pressure. $[N/m^2]$

p Kinematic fluid pressure as solved by OpenFOAM, P/ρ. $[m^2/s^2]$

R Radius of curvature from origin to leading edge of curved cylinder. $[m]$

Re Cylinder diameter Reynolds number based on uniform free-stream $Re = U_0 D/\nu$ $[-]$

Re_{bottom} Local Reynolds number at the bottom of the domain. $[-]$

Re_c Reynolds number according to median velocity. $[-]$

$Re_l(z)$ Local Reynolds number. $[-]$

Re_{top} Local Reynolds number at the top of the domain. $[-]$

ρ_{sim} Fluid mass density used by OpenFOAM in calculations. $\rho_{sim} = 1\ [kg/m^3]$

S Spanwise ordinate. $[m]$

$\Delta x_{refined}$ Cell size in x-direction after refining by SHM according to N_{refLvl}. $[m]$

$\Delta x_{background}$ Background cell size in x-direction as defined in BlockMesh.

N_{refLvl} Refinement level set in SHM for grid refinement.

δ_{final} Thickness of the layer farthest from the geometry when adding layers in SHM.

Δ Size of nearest cell outside layer mesh region.

ζ Size ratio of final layer cell to nearest non-layer cell δ_{final}/Δ.

er Expansion ratio of boundary layer grid cell size.

t^* Dimensionless time variable, tU_0/D. $[-]$

t Time variable. $[s]$

$\underline{\boldsymbol{\tau}}$ $\mu\boldsymbol{\nabla U}$, viscous stress tensor for a Newtonian fluid. $[N/m^2]$

t_{BL} Thickness of the boundary layer grid along the cylinder. $[m]$

θ Angular ordinate along teh curved part.

$\mathbf{U}^*$ Non-dimensional velocity vector $[u^*, v^*, w^*] = \mathbf{U}/U_0$. $[-]$

U_0 Inflow velocity. [m/s]

$U_0(z)$ Variable inflow velocity. $[m/s]$

$\mathbf{U}$ Velocity vector $[u, v, w]$. $[m/s]$

$\hat{\mathbf{U}}(t)$ Spatial average of $\mathbf{U}(x, y, z)$ over a control volume cell. $[m/s]$

U_{ax} Velocity component along the cylinder span. $[m/s]$

U_{bottom} Inflow velocity at bottom of the domain. $[m/s]$

U_c Median velocity in case of shear flow. $[m/s]$

$U_{concave}$ Definition of concave flow direction used in introduction section.

U_{convex} Definition of convex flow direction used in introduction section.

U_n Component of the inflow velocity which is normal to the cylinder axis

U_n Flow normal to cylinder axis. $[m/s]$

U_s Component of the inflow velocity which is parallell to the cylinder axis

U_s Spanwise velocity component for yawed cylinders.

U_{top} Inflow velocity at top of domain. $[m/s]$

u^*, v^*, w^* Non-dimensional velocity components, $u/U_0, v/U_0, w/U0$. $[-]$

u, v, w Velocity components in x-, y- and z-direction respectively. $[m/s]$

φ Scalar flow variable.

W_{fF} Width (along y-axis) of the farfield wake grid. $[m]$

W_{nF} Width (along y-axis) of the nearfield wake grid. $[m]$

x^*, y^*, z^* Non-dimensional cartesian coordinates, $x/D, y/D, z/D$. $[-]$

x, y, z Cartesian coordinates. $[m]$

Blank Page

1 Introduction

Flow past cylinders with circular cross-section is a widely studied subject in research due to its practical importance in engineering application on typical marine structures exposed current and waves. Typical examples in marine engineering are marine risers, offshore platform legs, underwater cables for transport of oil, gas and electricity, however also underwater vehicles such as submarines. Most of the research is conducted on two-dimensional cylinders and three-dimensional straight cylinders including both experimental and numerical research. Next in amount of research is the inclined straight cylinder where flow features have been compared to that of the straight cylinder. A rather recent area of research is the flow past curved cylinders, where only a handful of researchers have stepped in so far.

In this section the basic flow phenomena governing flow past circular cylindrical structures are summarized in section (1.1) and flow around inclined cylinders in section (1.2) as they define important apsects also related to curved cylinders. The specific research conducted on the flow past curved cylinders is summarized in section (1.3). Regarding the flow past straight and inclined cylinders, the presentation is limited to most important aspects relevant for the present study. This applies also to the range of Reynolds numbers considered.

Following sections are presented in the outline below:

- **Section 2: Governing Equations and Numerical Treatment.** Presents the governing fluid flow equations and the assumptions of the flow. Then the discretization in a Finite Volume Method of the resulting equations are explained and related to the model applied in OpenFOAM.
- **Section 3: Computational Grid and Domain.** Describes the generation of a computational grid in the tool SnappyHexMesh supplied with OpenFOAM and the resulting grid and domain layout applied in the present study. Flow variables and normalization practices are explained and boundary conditions are outlined.
- **Section 4: Grid Independence Study.** Describes the analysis that lead to the choice of a computational grid.
- **Section 5: Simulations - DNS Comparisons.** Verification with existing results from a previous DNS study.

- **Section 6; Simulations - Effect of Shear Inflow.** Results of a sheared inflow are presented.
- **Section 7: Conclusions.** A conclusion summary of the main findings.
- **Section 8: Appendix.** Additional plots and data which were not discussed in the main body.

Additional scripts and files developed are included along this thesis in a Zip-directory. These include:

- **H10V24R12 template:** A template OpenFOAM case-directory with homemade (be aware!) shell-scripts for running the shear-flow case. It is easy modifiable to run other cases as well on the same grid.
- **OF ANALYSIS:** MATLAB scripts for loading and post-processing of OpenFAOM data. MATLAB script and excel-sheet for preparing numerical probes. MATLAB script for preparing inflow velocity fields (shear profiles).

The template is not in working order as it requires a grid. A more complete set of data, details for simulations settings on Vilje and a working template for pre-processing, simulations and post-processing in OpenFAOM and SnappyHexMesh will be included on a harddrive to my supervisor Bjørnar Pettersen for further work.

1.1 Flow Past Circular Cylinders

The main characteristics of viscous fluid flow is often categorized in terms of the Reynolds number. Flow past bluff bodies, such as the circular cylinder, is no exception and the flow regimes occurring is often characterized by some range of the Reynolds number for the cylinder defined by (1).

$$Re = \frac{U_0 D}{\nu} \tag{1}$$

Where U_0 is the incident flow velocity, D is the cylinder diameter and ν is the kinematic viscosity of the fluid. As the Reynolds number is increased from zero, the flow around the cylinder experiences large changes. There are many definitions on the different regimes in the literature (especially regarding the Reynolds number range), however this text will consider the definitions of (Zdravkovich 1997), where the rough outline is according to table (1) below.

Table (1): Rough Reynolds number ranges for flow regimes around a circular cylinder in uniform flow. According to (Zdravkovich 1997)

.

State	Characteristic stages	Reynolds number range
Laminar state L	Creeping flow, steady separation, laminar vortex shedding.	$0 < Re < 200$
Transition-in-wake state TrW	Transition of laminar eddies in the wake, moving upstream with Re until transition during eddy formation.	$180 < Re < 400$
Transition-in-shear-layers TrSL	Transition waves, transition eddies, burst to turbulence.	$350 < Re < 2 \times 10^5$

The laminar state of flow (L) represents first the creeping flow range $0 < Re < 4-5$ where the flow remains symmetric about both an axis parallell and perpen-

dicular to the free stream flow direction, hence the shear layers remains symmetrical and attached and there is no wake behaviour. The next range considered is the steady laminar separation for $4-5 < Re < 30-48$ where the shear layers separate and forms a closed wake near the cylinder body. The so-called free shear layers meet at a distance downstream, which is gradually increasing with Re (Çengel 2014), leaving this closed loop of two recirculating regions of opposite direction. The steady behaviour reaches an end when the elongated near-wake becomes unstable. Instability in the wake causes the periodic laminar regime to commence and it lasts through $30-48 < Re < 180-200$. The instability in the wake initializes a wave-like oscillatory motion of the shear layers which amplitude increases with Re (Zdravkovich 1997) until the shear layers roll up in the "crests" and "troughs" when $Re > 45-65$, at which the wake flow is known as *Karman-Benard eddy street* (Zdravkovich 1997) after the French physicist *Henri Benard* and the Hungarian physicist *Theodore von Karman*. The phenomenon of eddies being formed on alternating sides of the cylinder and then convected downstream is also referred to as *vortex shedding*.

The range $180 < Re < 400$ is the transition-in-wake state (TrW) where the laminar eddies in the wake transitions to turbulence far downstream and the transition moves upstream as Re is increased. When $220-250 < Re < 350-400$ the transition happens during the formation of the eddies.

Transition-in-shear-layers (TrSL) state develops during a rather large range of Re as indicated in table (1). Three phases of this regime is used by (Zdravkovich 1997). First off in the range $350-400 < Re < 1-2\times10^3$ there is a development of *transition waves* in the shear layers which roll up into discrete eddies along the free shear layers as Re is increased. The small discrete eddies roll up into alternate eddies downstream once becoming turbulent. A burst to turbulence occurs in the free shear layers somewhere in the range $20\times10^3 < Re < 2\times10^5$ and the formation of alternate eddies takes place close to the rear of the cylinder.

1.2 Flow Past Inclined Circular Cylinders

Describing only the flow past a straight circular cylinder would be insufficient considering that many engineering applications will involve that cylindrical members are inclined in some way relative to the direction of inflow. A problem involving some certain *yaw angle* defining the relative angle between the cylinder axis normal and the free stream direction is convenient. This text will follow the nomenclature proposed by (Ramberg 1983) and according to figure (1). According to the figure, the component of the inflow velocity U_0 which is normal to the cylinder axis is defined by U_n in equation (2)

$$U_n = U_0 \cos \Lambda \tag{2}$$

Where Λ is the *yaw angle*. In figure (1) the angle of incidence α, spanwise velocity component U_s and the cylinder coordinate system (x', z') relation to global axis systems (x, z) are indicated.

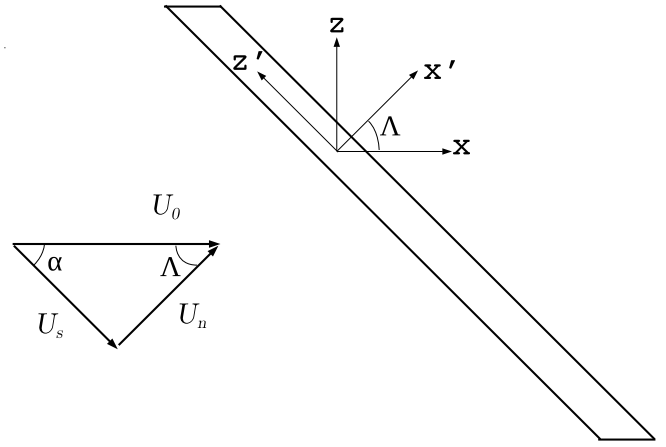

Figure (1): Definition sketch and nomenclature of the inclined cylinder problem.

A few initial observations of the problem can be made according to (Zdravkovich 2003):

- The cross-section of the circular cylinder becomes elliptical relative to the inflow U_0, and the ratio of major-to-minor axis of the ellipse is proportional to the yaw angle Λ.
- The free stream velocity has two components: one normal to the cylinder axis and one parallel to the cylinder span.
- It may be argued that U_n has a major effect on the flow, while U_s should have a minor effect.
- For $\Lambda = 45°$, $U_n = U_s$, while for $\Lambda > 45°$, $U_s > U_n$. Intuitively a larger Λ will contribute to a change in flow dynamics near the cylinder, and the U_n should become insignificant at some point.

A tempting solution to the problem is to regard the yawed cylinder as a straight cylinder only with an inflow velocity of $U_n = U_0 \cos\Lambda$. This is a convenient and widely applied method in engineering, and it is named the *independence principle* or the *cosine law* (Zdravkovich 2003). A theoretical confirmation for this velocity decomposition was given by (Sears 1948). He simplified the Navier-Stokes equations of motion for viscous fluids and applied the same order of magnitude analysis done by Prandtl in 1904 (see e.g. (White 2006)) for the laminar boundary layer equations, applying them to the special case of a yawed cylinder of infinite length. He found that $U_0 \cos\Lambda$ for the yawed cylinder follows the same equations as the U_0 for an unyawed cylinder. He also found that the spanwise boundary layer flow can be found by integration of a linear second-order differential equation. Combined this yields independence of normal flow and yaw angle, and hence the basis of the *Independence Principle*. However, several limitations must be mentioned for the use of this principle:

- Laminar boundary layer theory becomes invalid beyond flow separation, limiting the theory's applicability to within the stagnation and separation lines. This implies that base pressure and drag force might not be accurately described.
- By the infinite span approximation a 2D flow is implied and the theory will not account for end-effects.

- Flow disturbances introduced by spanwise flow is responsible for transition around separation for unyawed cylinders. The spanwise flow is likely to modify the disturbances and the value of Re at which transition around separation occurs for yawed cylinders.

1.2.1 Some Remarks in the TrSL state

Some interesting findings in research are reported for inclined cylinders in the TrSL state. The Reynolds number range is somewhat outside the target range in this study, however research on cylinders are historically mostly experimental and thus often at higher Reynolds numbers.

As the IP is not valid beyond separation, it is not expected to correlate vortex formation length and width in terms of Λ (Zdravkovich 2003). (Ramberg 1983) studied somewhat larger Reynolds numbers of $Re = 550$ and $Re = 750$. He scaled the vortex formation length and also the base pressure coefficient according to IP, and the results were not coinciding with the unyawed case.

In the range of $1 \times 10^3 < Re < 52 \times 10^3$ (Shirakashi, Wakiya, and Hasegawa 1986) tested the validity of using equivalent elliptical straight cylinders for describing the inclined cylinder problem. The elliptical cylinder are less bluff than circular cylinders implying a narrower wake and higher St, however the case for a yawed cylinder is exactly the opposite (Zdravkovich 2003). (Shirakashi, Wakiya, and Hasegawa 1986) verified this concluding that the analogy between elliptic cylinders and the yawed circular cylinder does not hold.

(Tournier and Py 1978) conducted experiments measuring surface velocity gradients along the circumference and the span of a circular cylinder tested at $Re = 13.9 \times 10^3$ for $\Lambda = 0°$, $10°$, $20°$and $30°$. Time-averaged velocity gradients from each yaw angle projected normal to the flow was found to coincide with the friction coefficient curve for an unyawed cylinder, proving the validity of the IP. The IP scaling was however not appropriate for the spanwise velocity gradient which is zero for a straight cylinder.

(Shirakashi, Ueno, et al. 1984) measured eddy shedding frequency in a wide

range of $50 < Re < 1.2 \times 10^4$ for $\Lambda = 39°$. In the L3 (lanminar vortex shedding) and TrSL1 (transition waves in shear layers) regimes experimental points were found to collapse onto the empirical curve. However in TrW (transition in wake) and TrSL2 (transition eddies in shear layers) a notable scatter was observed, indicating complex interference between the inclined cylinder geometry and the transitional three-dimensional wake.

(Hayashi et al. 1992) measured extended the measurement of shedding frequencies to along the span of a cylinder inclined to $\Lambda = 10°$ and $\Lambda = 20°$ at a single $Re = 2 \times 10^4$ with and without end plates. He found three notable features:

- Eddy shedding is not uniform along the span. A variation in shedding frequency along span was observed.
- Addition of end plates for $\Lambda = 10°$ improves the uniformity of eddy shedding.
- At $\Lambda = 10°$ the frequency density is irregularly distributed along the span and narrow-banded. At $\Lambda = 20°$ peaks are lowered by an order of magnitude, spectrum is more broad-banded and the spanwise distribution is more regular.

(Hayashi et al. 1992) further plotted St along the span for each cylinder ($\Lambda = 0°$, $10°$, $20°$, with and without end plates) and found evidence of distinct eddy shedding cells along the span with different frequencies. Without end plates, the St variation along the span was found to be similar for the straight and inclined case. For $\Lambda = 10°$ the St is preserved. However for end plates two eddy shedding cells was indicated for $\Lambda = 10°$ and three shedding cells for $\Lambda = 20°$. It appears that the weakening of eddy shedding is associated with shedding cells at different frequencies (Zdravkovich 2003).

(Shirakashi, Wakiya, and Hasegawa 1986) found that partition plates placed behind the inclined cylinder at $\phi = 180°$ prevented secondary flow in the spanwise direction, thereby limiting interference with the vortex shedding mechanism and providing a recovery of strong vortex shedding.

(Smith, Moon, and Kao 1972) confirmed the invalidity of the IP for determining

the base pressure, thus also rendering the IP useless for evaluating the drag coefficient for inclined cylinders.

1.3 Flow Past Curved Cylinders

Considering marine hydrodynamics application, the geometry of a curved cylinder becomes equally important as inclined cylinders. Examples are flexible risers, pipelines for transport of oil and gas, and components of subsea production systems. Although the amount of research conducted on straight and inclined cylinders are enormous, the documentation on flow past curved circular cylinders is more limited. However since the beginning of the 2000s there has seemed to become an increasing interest in gaining knowledge on curved cylinders as well. A few numerical studies as well as some experimental studies have been done so far on the curved cylinder, and the most common arrangement is according to the sketch in figure (2).

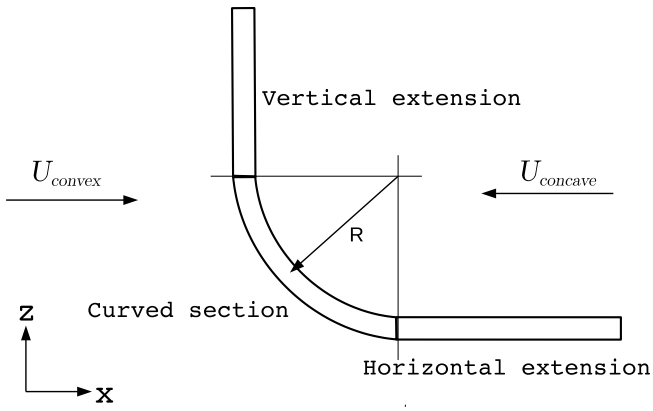

Figure (2): Sketch of the most common idea of arrangements so far when dealing with the curved cylinder problem.

In figure (2) above the general geometry is indicated by the constant curvature section *curved section* as well as the two extensions *vertical extension* and *hori-*

zontal extension. For the flow being parallel to the plane of curvature (i.e. the (x, z)- plane) there has been two main cases of study; the inflow being in towards the convex part of the geometry, denoted here by U_{convex}, and the inflow being in towards the concave geometry, denoted by $U_{concave}$.

1.3.1 Experimental Studies

(Assi et al. 2014) cunducted model experiments with two degrees of freedom for a rigid curved cylinder in the Reynolds number range of $750 < Re < 1.5 \times 10^4$. Both convex and concave configurations were considered and compared to the response of a typical straight cylinder. It was shown that the curved cylinder has lower peak vibration amplitude than a comparable straight cylinder. Although the peak amplitude was reduced, the curved cylinder may still present signigicant levels of vibration that are sustained for a wider range of reduced velocity than the typical synchronization range. Streamwise vibration was also observed for very high reduced velocity (up to $V_r = 18$). Overall response showed little dependency on the vertical section of length $h = 0$ to $h = 10D$. Different flow interactions in the concave and convex configuration was observed, and it is proposed that this could be related to buffeting, galloping, disturbed VIV or geometric instability.

1.3.2 Numerical Studies

In the extensive report by (Miliou et al. 2007) results of flow past a stationary curved cylinder in both convex and concave configuration was given for $Re = 100$ and $Re = 500$. The flow was found to be highly three-dimensional for each flow configuration, and also very dependent on the geometry. Flow visualization was confirmed by towing the curved cylinder according to the straight cylinder experiments by (Slaouti and Gerrard 1981). For both convex and concave geometry, the flow at the stagnation face in spanwise direction was found to be significant of magnitude up to 30% of free stream velocity. In the concave configuration spwanwise flow was observed also immediately behind the cylinder. In the convex configuration vortex shedding was driven mainly by the shedding from the vertical section, resulting in a single shedding frequency occurring along the span,

in contrast to what would be expected from an independence principle analysis. Vortex shedding was completely suppressed at $Re = 100$ for concave geometry, and a lower shedding frequency than expected was observed for $Re = 500$ at the top of the cylinder. The vortex suppression resulted in a reduction in total drag. The effect of the artificial boundary condition at the top (considering no vertical extension) was investigated for the concave geometry by introducing a vertical extension of 6D in length. The impact was tremendous as the flow went from nearly non-interacting shear layers to a strong interaction due to axially aligned flow in the near wake of the cylinder.

(Vecchi, Sherwin, and Graham 2008) studied the fundamental mechanism of vortex shedding past a curved cylinder in both convex and concave configuration at $Re = 100$. Two different kinds of oscillatory motion was tested; transverse oscillation of the whole cylinder setup and a roll oscillation about the horizontal cylinder axis. For the transverse oscillation of the convex configuration it was found that vortices are shed more in phase along the span making the vortex cores curve along the cylinder, while as (Miliou et al. 2007) found for the stationary curved cylinder the phase of vortex shedding is shifted such that vortex cores are straight. (Miliou et al. 2007) also found that for a stationary cylinder in the concave configuration vortex shedding was suppressed, however by (Vecchi, Sherwin, and Graham 2008) the transversely oscillating cylinder in concave configuration exhibits the same curved vortex core shedding. A hydrodynamic damping force was found due to the transverse oscillation of the horizontal section. For the case of the rotation oscillation about the horizontal cylinder axis, the damping was no longer present and the wake was completely different exhibiting out-of-phase vortex shedding however twisted spanwise farther downstream.

(Canabes 2010) studied in his masters thesis the convex geometry by direct numerical simulation at $Re = 100$ and $Re = 500$. Two inflow boundary conditions, one uniform and one a linear shear profile. Stagnation line area, recirculation region, vortical structures in the wake and shedding frequencies were investigated. The normalized pressure coefficient was calculated along the front and rear stagnation lines indicating that the Independence Principle may be used for the stagnation lines up to an angle of 45°measured from the top plane. A

favourable pressure gradient induced a significant axial flow along the leading edge of the cylinder for both Reynolds numbers. The presence of shear flow increased this effect in the upper part of the cylinder, as well as exhibiting a region of almost zero pressure gradient along the rear stagnation line affecting the recirculation zone. For uniform flow vortices were shed at one single frequency. The increase of radius of curvature was found to have no effect on the Strouhal number, in contrast to earlier research. Some Strouhal dependence on domain size was also reported. For uniform shear flow, two distinct vortex shedding cells were observed for both Reynolds numbers. Vortical structures were in good agreement with the studies by (Miliou et al. 2007).

(José P Gallardo, Bjørnar Pettersen, and Helge I Andersson 2011) investigated the turbulent wake of the convex configuration at $Re = 3900$ finding similar periodic vortex pattern to studies at lower Re (Miliou et al. 2007), however some tilting of vortices was observed. Stronger influence from secondary flow along the span was found to increase the degree of flow instability. Also influence of the top symmetry boundary condition was found to suppress instability in shear layers. Top boundary conditions are further investigated in (José P. Gallardo, Bjørnar Pettersen, and Helge I. Andersson 2013).

In (José P Gallardo, Helge I Andersson, and Bjørnar Pettersen 2014) the convex configuration at $Re = 3900$ is studied including a vertical extension to separate effects of free-slip top boundary condition. Slightly lower vortex shedding fequency was found in the upper straight section compared to the dominant curved section. A mild axial flow in the lee side of the cylinder was found to displace the recirculation region in the very near wake as well as impacting the wake behind the vertical extension. A *lower wake* and *upper wake* was suggested due to the distinct enhanced three-dimensionality and less vigorous shedding in the lower wake. Turbulence properties was found to be essentially unaffected by axial curvature. Shear layer instabilities were significantly greater in the lower part compared to the upper part. (José P Gallardo, Helge I Andersson, and Bjørnar Pettersen 2014) also suggests that enhanced scrambling in the lower wake at $Re = 3900$ tends to decorrelate the vortex dynamics in the lower part of the wake from the shedding further up, reducing the risk of VIV.

Further investigations of the turbulent wake for a curved circular cylinder was conducted in (José P. Gallardo, Bjørnar Pettersen, and Helge I. Andersson 2014) with the aim to investigate the possibilities of analyzing the curved cylinder problem without the use of a full 3D approach as DNS (Direct Numerical Simulation) or LES (Large Eddy Simulation). Simplified methods discussed are RANS (Reynolds-Averaged Navier-Stokes) and ROM (Reduced Order Modelling). Especially for the use of RANS, a turbulence model capable of representing highly anisotropic flow dynamics should be selected for curved cylinders. This is due to the large variations in different Reynolds stress components along the depth.

(Xu and Cater 2016) studied the curved cylinder geometry numerically simulating a marine riser in ocean currents at $Re = 1.5 \times 10^5$ in a logarithmic velocity profile. The geometry was defined by a constant radius of $R = 12.5D$, there was only a straight extension of aspect ratio $L/D = 20$. The diameter of the cylinder was $D = 0.3m$ according to full scale, sea water properties at 15°C were used, and thus the maximum velocity in the logarithmic flow profile was set to $0.6m/s$ to obtain the required reynolds number. Both the convex and concave configurations were studied in both uniform and logarithmic inflow, as well as a straight cylinder of same height and diameter.

(Xu and Cater 2016) used the commercial software ANSYS Fluent solving the time-averaged Navier-Stokes equations. Wall function was used with a constraint for the non-dimensional wall distance $y^+ < 30$. A mesh refinement study of intervals around the cylinder resulted in converged solutions for C_D, $C_{L,RMS}$ and St at 180-200 angular elements. 180 angular elements was found accpetable. This was used for both straight and curved cylinder. Multiple closure models were tested and the realizable $k - \epsilon$ model was used since it was found to be the best match with experimental data for straight cylinders. In both uniform and logarithmic flow, the concave configuration was found to have the lowest value of C_L. For both cases it was argued that the reduction in drag was due to suppression of vortex shedding due to the geometry altering the local velocities. Regular vortex shedding in concave configuration is suppressed more than in the convex configuration. For the uniform inflow case, this effect is naturally larger than for the logarithmic inflow, since the logarithmic profile introduce

lower velocities around the curved section in any case. In both inflow conditions, the cylinder experiences the smallest $C_{L,RMS}$ in the concave configuration, while the straight cylinder experiences the largest $C_{L,RMS}$.

Further for the uniform flow case (Xu and Cater 2016) found the convex configuration to have a similar vortex structure as a straight cylinder in the wake, and the concave configuration showed less vorticity shed in the lower section. In logarithmic flow the concave configuration generated less circulation, and had a smaller re-circulation zone compared to the convex configuration. Significant limitations of the study is that fully turbulent flow has been assumed and turbulent transition processes is not modelled. Also no matching experimental data exist for these Reynolds numbers.

The concave problem for the curved cylinder configuration was studied by (F. Jiang, B. Pettersen, and H. I. Andersson 2018) with a focus on the influences of the horizontal extension. The unsteady three dimensional Navier-Stokes equations were solved directly for Reynolds number $Re = 100$. Due to the flow direction, the interaction between the inlet boundary and cylinder is unavoidable. The boundary layer development along the horizontal extension was studied and the boundary layer was found to be thinner than for the Blasius solution given in ((White 2006), p.232). Configurations with horizontal extensions of length $h = 5D$ and $h = 10D$ were tested as well as one where $h = 0$. It was found that the flow conditions entering the curved part of the cylinder is very different whether a horizontal extension is considered or not. Streamwise velocity drops abruptly over the first 2-3D and a further reduction is observed along the 5D or 10D extension. The boundary layer profile reaching the curved cylinder is considerably thicker when horizontal extensions are considered, meaning that the inflow boundary condition alone (exponential boundary layer profile) provides a too thin boundary layer at the curved cylinder. Local peaks in streamwise and vertical velocity was found using horizontal extensions, however only a vertical velocity peak was found when no horizontal extension was included. Due to the very different flow conditions, a minimum horizontal extension of $h = 5D$ was recommended, however $h = 10D$ is preferred for numerical studies of the concave problem.

Recent unpublished studies of direct numerical simulations (F. Jiang, B. Pettersen, H. I. Andersson, et al. 2018) at the Institute for Marine Technology, NTNU[1] considers the effect of the length of vertical extensions, and thus the top boundary, in the concave flow configuration. Reynolds numbers in the range of $Re = 100 - 500$ are considered so far with vertical extension lengths spanning up to 24 cylinder diameters. The spanwise flow has proven very strong with a value of $\sim 20\%$ of the incident flow velocity even as far as ~ 20 diameters vertically. There is a tendency of a complex transitional region occurring at the intersection between the curved part and vertical extension. This region is more prominent as Reynolds number increases.

[1] Norwegian University of Science and Technology

Blank Page

2 Governing Equations and Numerical Treatment

This section describes the different aspects of solving the governing equations for viscous flow known as the Navier-Stokes equations. Assumptions made about the flow are listed and a resulting form of the governing equations are obtained. A background on numerical treatment of the equations in a finite volume method (FVM) formulation are reviewed and related to the settings used in OpenFOAM.

This section follows to some extent the reasoning of FVM methods compiled in the excellent reviews on the subject given in (Versteeg 2007), (Ferziger 2002) and (Pletcher 2013).

2.1 The Navier-Stokes Equations

The general set of equations to be solved for viscous flow are the Navier-Stokes equations. They exist in various forms however they can be represented in general as a set of four (in three spatial dimensions) equations consisting of three momentum equations and one equation for mass conservation. The momentum equations are represented by the vector integral equation (3) depicting Newtons 2^{nd} law of motion for forces acting on a fluid control volume Ω of boundary $\partial\Omega$. Newtonian fluid is assumed.

$$\int_{\Omega} \frac{\partial \rho \mathbf{U}}{\partial t} dV + \int_{\partial\Omega} \rho \mathbf{U}(\mathbf{U} \cdot \mathbf{n}) dA = -\int_{\partial\Omega} P\mathbf{n} dA + \int_{\partial\Omega} \underline{\boldsymbol{\tau}} \cdot \mathbf{n} dA + \int_{\Omega} \rho \mathbf{f} dV \quad (3)$$

Here $\underline{\boldsymbol{\tau}} = \mu \boldsymbol{\nabla} \mathbf{U}$ is the viscous stress tensor for a newtonian fluid [2], $\mathbf{U} = [u, v, w]$ the velocity vector with its respective cartesian components in x, y and z directions, $\mathbf{n}$ is the control volume outward normal vector along $\partial\Omega$, P is the fluid pressure on the control volume boundary and $\mathbf{f}$ represents an acceleration vector of an arbitrary volume force acting on Ω.

[2] strictly a general deformation law for a linear newtonian fluid involves the *coefficient of bulk viscosity* "λ", however it is omitted already here as it disappears for incompressible flow (White 2006)

The mass conservation for a control volume Ω with boundary $\partial\Omega$ is expressed as in equation (4).

$$\int_{\Omega} \frac{\partial \rho \mathbf{U}}{\partial t} dV + \int_{\partial\Omega} \rho \mathbf{U} \cdot \mathbf{n} dA = 0 \tag{4}$$

The flow assumptions below are imposed to obtain the governing equations for this present study, that is the momentum equations (5),

Flow assumptions:

- Density $\rho = \text{const.}$ (i.e. incompressible)
- Viscosity $\nu = \text{const.}$
- No external body forces. (i.e. gravity is neglected.)
- Single component fluid.
- Newtonian fluid.

$$\int_{\Omega} \frac{\partial \mathbf{U}}{\partial t} dV + \int_{\partial\Omega} \mathbf{U}(\mathbf{U} \cdot \mathbf{n}) dA = -\frac{1}{\rho} \int_{\partial\Omega} P\mathbf{n} dA + \int_{\partial\Omega} \mu \boldsymbol{\nabla}^2 \mathbf{U} dA \tag{5}$$

as well as the continuity equation (6).

$$\int_{\partial\Omega} \mathbf{U} \cdot \mathbf{n} dA = 0 \tag{6}$$

Equations (5) and (6) are now the equations that needs to be modelled, i.e. discretized in a FVM formulation.

2.2 Accuracy and Numerical Stability

CFD methods are numerical methods which in general aim at approximating the solution of partial differential equations (PDEs) describing the physics of fluids in motion. The most general case will involve three dimensions in space and one in time. With discretization schemes and computer calculations follows mainly

two sources of error from the exact solution: round-off error in the computations and a truncation error inherent in the discretization scheme used. For every time step, iterations on flow variables u, v, w and p must be performed and the criteria set for when to stop the iterations are also sources of error. The stopping criterion must be specified either by *maximum number of iterations* or a limit for maximum change in a variable from one iteration to the next, i.e. *convergence criterion*.

OpenFOAM utilizes a finite volume method (FVM) for discretization in space, meaning a discretization of the computational space (domain) in small volumes of finite size, then using some method of advancing the solution in timesteps. For the FVM to obtain accuracy it must be *consistent*, i.e. it must approximate the PDE such that the truncation error $TE = FVM - PDE$ goes to zero as the discretization is refined in space and time (Ferziger 2002). Furthermore by the well known Lax Equivalence Theorem for linear PDEs (Pletcher 2013, pp. 53), the FVM is assumed to *converge* if it is also *stable*.

Stability analysis is in general quite complex and is based on analysing whether the FVM solution stays bounded to the properties of the exact PDE as one marches in time. However important work was done by Courant and Friedrichs in the 1920s finding dimensionless numbers influencing the stability of the solution. A simple case involving unsteady convection-diffusion resulted in a criterion for the finite time step Δt to ensure stability. The dimensionless *Courant number* is given in equation (7). As the number has significance in each coordinate direction it is defined in this thesis with index i. u_i and Δx_i represents the velocity component and a finite length in each coordinate direction $i \in 1, 2, 3$ representing Δx, Δy and Δz respectively.

$$Co_i = \frac{u_i \Delta t}{\Delta x_i} \tag{7}$$

If one considers convection transport to be dominant, the stability criterion in equation (8) is obtained for an explicit time scheme by setting $Co < 1$ (Ferziger 2002). It is known as the CFL-condition.

$$\Delta t < \frac{\Delta x_i}{u_i} \tag{8}$$

The logic behind the criterion is that the combination of time step and discretization in space must be such that no information in the domain travels faster in one time step Δt than what the grid Δx_i is able to capture during Δt.

In the present study an implicit time scheme was used, known as the Crank-Nicolson scheme (discussed in section (2.4)). The CFL-condition is a simplified stability and convergence criterion based on an explicit time scheme, however it has proven useful in practice as a rule of thumb.

2.3 Spatial Finite Volume Discretization

As for numerical discretization the Navier-Stokes equations are complicated. Each term needs to be treated with care, and the choices of discretizations are many, even in OpenFOAM. In particular the spatial discretization is described in this section. As a cell-centered method is used, the finite volume method relies on conservation of flow variables locally in control volumes and the use of cell average values. Introducing the cell average of the velocity vector $\hat{\mathbf{U}}(t)$ such that equation (9) holds,

$$\hat{\mathbf{U}}(t) = \frac{1}{|\Omega|} \int_{\Omega} \mathbf{U}(x, y, z, t) dV \tag{9}$$

where $|\Omega| = \int_{\Omega} dV$ is the volume of cell Ω, we can express the Navier-Stokes vector equation as equation (10).

$$|\Omega| \frac{d\hat{\mathbf{U}}(t)}{dt} + \int_{\partial\Omega} \mathbf{U}(\mathbf{U} \cdot \mathbf{n}) dA = -\frac{1}{\rho} \int_{\partial\Omega} P\mathbf{n} dA + \int_{\partial\Omega} \mu \boldsymbol{\nabla}^2 \mathbf{U} dA \tag{10}$$

By the use of Gauss' Divergence Theorem, we can go back to the volume integral equation (11) for conservation of fluid momentum.

$$|\Omega| \frac{d\hat{\mathbf{U}}(t)}{dt} + \int_\Omega \underbrace{(\boldsymbol{\nabla} \cdot \mathbf{U})\mathbf{U}}_{1} dV = -\frac{1}{\rho} \int_\Omega \underbrace{\boldsymbol{\nabla} P}_{2} dV + \int_\Omega \mu \underbrace{\boldsymbol{\nabla}^2(\mathbf{U})}_{3} dV \tag{11}$$

2.3.1 OpenFOAM Numerical Schemes

In OpenFOAM the spatial discretizations get their name from the terms marked in equation (11) as 1, 2 and 3, and these have different scheme settings. The different options will not be discussed, however the settings used in the present study is presented in table (2).

Table (2): OpenFOAM spatial FVM discretization.

OpenFOAM Setting	Type	Affected term
gradSchemes	Gauss, Linear	2
divSchemes	Gauss, Linear	1
laplacianSchemes	Gauss, Linear, Corrected	3
snGradSchemes	Corrected	3

The settings available have very compact names and need some explanation so that the meaning of them are clear. As the name indicates, “gradSchemes” defines the treatment of terms associated with the gradient operator, “divSchemes” handles convective terms (divergence operator) and “laplacianSchemes” are used for diffusive terms (laplace operator).

The settings are “Gauss, Linear” indicating that standard Gaussian integration over cell faces is used on the area integrals in equation (5) and the interpolation of cell centre averages to cell faces are linear. Otherwise the “Linear” setting states that central differences are used for approximating derivatives in the diffusion term 3 in equation (11).

Consequences of the settings are investigated by simplifying the governing equations, applying the discretization and observing the mathematical behaviour of the solution. By removing the time dependency, the pressure link and considering a scalar flow property, equation (3) becomes equation (12). It describes a scalar conservation law for convection-diffusion problems for a general property φ.

$$\int_{\partial\Omega} \mathbf{n} \cdot (\rho\varphi\mathbf{U}) dA = \int_{\partial\Omega} \mathbf{n} \cdot (\nu \boldsymbol{\nabla}\varphi) dA + \int_{\Omega} \rho \mathbf{f} dV \tag{12}$$

Considering the absence of volume forces and only one-dimensional flow in the x-direction, equation (12) reduces to the simple equation (13)

$$\frac{d(\rho u \varphi)}{dx} = \frac{d}{dx}(\nu \frac{d\varphi}{dx}) \tag{13}$$

In figure (3) a one-dimensional grid is sketched along with a distribution of the variable φ. A cell with centre node P and its West and East neighbour cells are illustrated with their common cell faces. The linearly interpolated value of φ at the cell faces are marked as φ_w and φ_e, and fluid velocity at the cell faces are termed similarly as u_w and u_e.

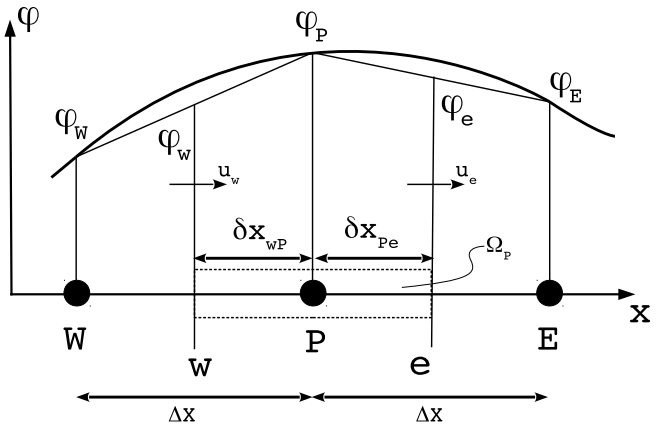

Figure (3): A FVM cell with centre node P and its two neighbour cells W(est) and E(ast) in one dimension. Cell faces are indicated by little "w" and "e". The actual distribution of a variable φ across the three cells are marked with its corresponding linearly interpolated values at the cell faces. Convective velocities across cell faces indicated by u_w and u_e, and Ω_P is the volume of cell P.

Gaussian integration of equation (13) over the control volume in figure (3) yields equation (14), where ρ is the fluid density, u the convective fluid velocity, A is the cell face area, ν is the fluid kinematic viscosity and φ is the transported property.

$$(\rho u A\varphi)_e - (\rho u A\varphi)_w = \left(\nu A\frac{d\varphi}{dx}\right)_e - \left(\nu A\frac{d\varphi}{dx}\right)_w \tag{14}$$

Knowing only the cell centre values, it is now evident that the net convective flux on the left hand side requires interpolated values on cell faces and the net diffusion flux on the right hand side requires that gradients are approximated across cell faces. The linear interpolation to cell faces on a uniform grid results in equations (15)

$$\varphi_w = \frac{\varphi_W + \varphi_P}{2} \tag{15a}$$

$$\varphi_e = \frac{\varphi_E + \varphi_P}{2} \tag{15b}$$

and the central differencing scheme for gradients at cell faces on a uniform grid yields equations (16).

$$\left(\frac{d\varphi}{dx}\right)_e = \frac{\varphi_E - \varphi_P}{\Delta x} \tag{16a}$$

$$\left(\frac{d\varphi}{dx}\right)_w = \frac{\varphi_P - \varphi_W}{\Delta x} \tag{16b}$$

The accuracy analysis of the central difference scheme is well documented in literature. One example is found in (Versteeg 2007) and by Taylor series development the spatial accuracy is shown to be $\mathcal{O}(\Delta x^2)$ on a uniform smooth grid.

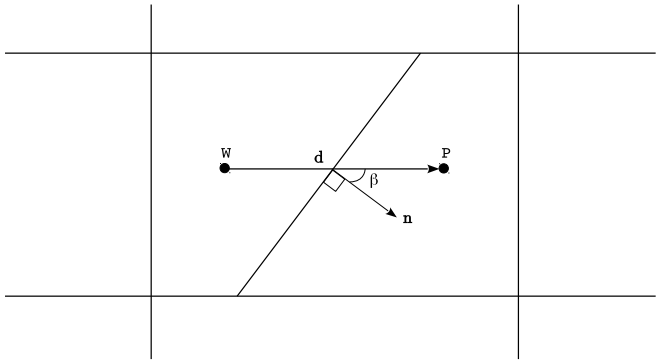

Figure (4): Level of non-orthogonality between cells P and W denoted by the angle β. β is the angle between the cell-to-cell distance vector $\boldsymbol{d}$ and the cell face normal vector $\boldsymbol{n}$.

In figure (4) the level of non-orthogonality between two cells P and W is illustrated as the angle β, which is the angle between the cell-to-cell distance vector $\boldsymbol{d}$ and the cell face unit normal vector $\mathbf{n}$. The surface-normal gradient of flow variable φ between the two cells is just a projection of the cell-to-cell gradient along $\mathbf{n}$, which will mathematically look like equation (17).

$$\boldsymbol{\nabla}_{fn}(\varphi) = \mathbf{n} \cdot (\boldsymbol{\nabla}\varphi)_f \tag{17}$$

Where now $\boldsymbol{\nabla}_{fn}(\varphi)$ is the face normal component of the cell-to-cell gradient of φ, and $\boldsymbol{\nabla}(\varphi)_f$ the cell-to-cell gradient of φ.

The "Corrected" setting indicates the non-orthogonal correction of cell-to-cell gradients. As discussed the central difference scheme for gradients is second order in space, however any non-orthogonality between cells will degrade this behaviour. The snGradSchemes "Corrected" applies correction to cell-to-cell gradients' face normal components with the aim of preserving second order accuracy. The level of non-orthogonality in the present study is low, however the corrected scheme is in general recommended (OpenFOAM 2018b) for any grid not fully orthogonal.

Equation (18) describes the implicit 1 and the explicit 2 correction made to the surface normal gradient.

$$\boldsymbol{\nabla}_{fn}(\varphi) = \underbrace{\alpha \frac{\varphi_P - \varphi_W}{|\mathbf{d}|}}_{1} + \underbrace{(\mathbf{n} - \alpha\hat{\mathbf{d}}) \cdot (\boldsymbol{\nabla}\varphi)_f}_{2} \tag{18}$$

Where $\alpha = 1/\cos(\beta)$ is the parameter increasing the corrections with increasing angle of non-orthogonality β, $|\mathbf{d}|$ is the distance between cells P and W as in figure (4) and $\hat{\mathbf{d}}$ is the unit distance vector.

2.4 Time Integration

After looking at the spatial discretization it is natural to look into the treatment of the temporal discretization as the flow around circular cylinders are highly unsteady depending on the Reynolds number[3] and in fact even oscillatory. The spatial descretization is unaffected, however the time derivative term of equation (11) must be discretized and the governing equations must be integrated over a finite time step Δt.

The spatial discretization can now be collected in the residuals vector $\mathbf{R}(\mathbf{\Phi}(t))$ such that the transient equation to be discretized and solved in time takes the form of equation (19). Now $\mathbf{\Phi}(t)$ is the vector of conserved flow variables to be solved for, such that

$$\frac{\partial \mathbf{U}}{\partial t} = \mathbf{R}(\mathbf{\Phi}(t)) \tag{19}$$

is the system of equations. Where for three-dimensional problems $\mathbf{R}(\mathbf{\Phi}(t))$ is a vector of residual vectors as a function of the conserved variables.

The general equation for the flow problem at hand will take the form of equation (20) when integrating in time.

$$\frac{\hat{\mathbf{U}}^{n+1} - \hat{\mathbf{U}}^{n}}{\Delta t} = \frac{1}{|\Omega|} \int_{t}^{t+\Delta t} \left[- \int_{\partial\Omega} \mathbf{U}(\mathbf{U} \cdot \mathbf{n}) dA - \frac{1}{\rho} \int_{\partial\Omega} P\mathbf{n} dA + \int_{\partial\Omega} \mu \boldsymbol{\nabla}^2 \mathbf{U} dA \right] \tag{20}$$

Where $n+1$ represents the solution at the next time level and n represents the current time level.

In the present study a time differencing scheme known as the Crank-Nicolson scheme is applied. The scheme is accurate to $\mathcal{O}(\Delta t)^2$ as it uses a trapezoidal rule approach in time (Ferziger 2002). For a scalar conservation law of a convection-diffusion problem in one dimension (equation (21)),

[3] onset of laminar vortex shedding for $Re > 40$, (Sumer 2006)

$$\frac{d(\rho\varphi)}{dt} + \frac{d(\rho u\varphi)}{dx} = \frac{d}{dx}\left(\nu\frac{d\varphi}{dx}\right) \tag{21}$$

a general time scheme is given as equation (22).

$$\varphi_P^{n+1} = \varphi_P^n + \Delta t\left[\Psi D^{n+1} + (1-\Psi)D^n\right] \tag{22}$$

Where D^{n+1} and D^n represent the spatial discretization evaluated at the new time step and the present time step respectively. The $\Psi \in [0,1]$ is a weighting parameter where $\Psi = 0$ and $\Psi = 1$ represent the explicit and fully implicit time scheme respectively. To obtain the pure Crank-Nicolson scheme, a $\Psi = 1/2$ is used.

In OpenFOAM the Crank-Nicolson scheme uses an "off-centering" parameter between 0 and 1. The off-center parameter controls a blend between the pure Crank-Nicolson scheme (parameter is 0) and the fully implicit Euler scheme (parameter is 1), i.e. the off-centering parameter is equivalent to adjusting Ψ between 1/2 and 1 in equation (22).

In the present study an off-centering parameter in OpenFOAM at 0.9 is used as a good compromise between accuracy and stability according to recommendations in (OpenFOAM 2018b).

2.5 Pressure-Velocity Coupling

The occurence of the pressure term (term 2 in equation (11)) in the Navier-Stokes equations poses difficulties for incompressible flows as there is no independent equation governing the pressure. However the momentum equations depend on the gradient of the pressure, so it must be dealt with. A way of tackling the problem is to construct the pressure field so that continuity is guaranteed (Ferziger 2002). This is done by introducing a pressure-correction equation based on the continuity equation (Ferziger 2002).

(Patankar 1980) reviews the implementation of a pressure-correction equation

in the SIMPLE[4] algorithm. It is an algorithm for solving the steady Navier-Stokes equations by iterating on the pressure to enforce continuity. The algorithm iteration sequence in short is as follows (Patankar 1980):

- Guess the pressure field.
- Solve discretized momentum equations to obtain preliminary velocity field.
- Solve pressure-correction equation.
- The pressure correction is added to the pressure field.
- Velocities are corrected according to corrected pressure field.
- The new pressure field is used as a guess in the first step.

The iterations continue until some quantity described as the "mass source" is sufficiently small. The mass source formula is directly derived from the discretized continuity equation (Patankar 1980). It is a measure of the magnitude of divergence error and thus continuity error.

A further issue related to the pressure is discussed in (Patankar 1980) and relates to how the pressure is discretized on the grid. The problem is that certain pressure gradients might not be felt by the momentum equations if e.g. a "checker-board" type pressure field emerges. This is illustrated in figure (5).

[4]Semi-Implicit Method for Pressure-Linked Equations

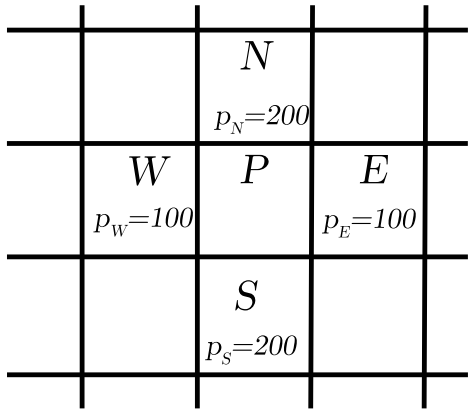

Figure (5): A pressure field causing difficulties in calculating the net pressure force on cell P when a conventional collocated grid is used. Neighbour cells W, E, N and S containing pressure values p_W, p_E, p_N and p_S. N and S, and W and E might contain similar pressure values resulting in a net zero pressure force on P.

The problem mainly arises when pressure and velocity both are defined in the same cell centres, i.e. when a *collocated grid* is used. Pressure force on the control volume P is then found by the gradient between cell W and E, which in the illustrated case gives a net zero pressure forcing in cell P.

A remedy was proposed by (Harlow and Welch 1965) with the *staggered grid* approach, where the "main grid" keeps the pressure values stored in cell centres. Velocities are defined on cell centres in individual grid systems such that they appear on the cell faces of the "main grid". This is illustrated for a cell P in figure (6).

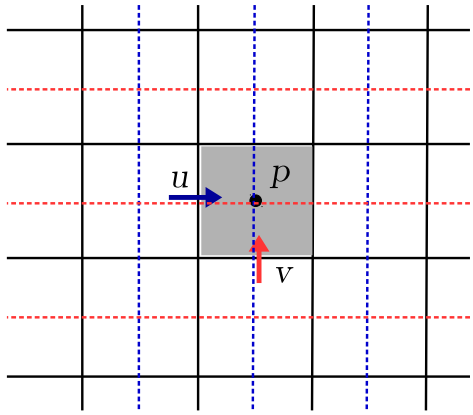

Figure (6): Illustration of a *staggered* arrangement where pressure is defined on the main grid (—), and velocities located at cell faces for u (- - -) and v (- - -).

OpenFOAM does not strictly utilize the staggered grid approach, as both velocities and pressure are located in the cell centres. However during pressure calculations the velocities are interpolated to cell faces and included as face fluxes (OpenFOAM 2018a).

The PISO[5] (Issa 1986) algorithm is considered an extension of the SIMPLE algorithm by including a predictor step for velocities and a second corrector step (Versteeg 2007). The transient version of the PISO algorithm is used for unsteady flows in OpenFOAM and it requires the number of corrector steps set to 2 or more (OpenFOAM 2018b). It is obtained by including transient terms in the discretized momentum equations and the pressure equation. Otherwise the algorithm sequence is the same. In OpenFOAM there is a choice to include multiple extra corrector steps in the PISO algorithm, however typically more than 4 is not required (OpenFOAM 2018b).

As will be discussed later, it is preferable to have the ability of adjustable time steps. The PISO solver in OpenFOAM does not support the ability to use adjustable time steps during the simulation, so the solver *pimpleFoam* (OpenFOAM 2018b) is used in the present study utilizing 2 corrector steps. The PIMPLE algorithm is what OpenFOAM calls a combination of PISO and SIMPLE. By setting

[5]Pressure Implicit with Splitting of Operators

number of corrector steps to 2 however retains the behaviour of the PISO solver (OpenFOAM 2018b).

Blank Page

3 Computational Grid and Domain

There are several possibilities for mesh generation for use in OpenFOAM as mesh converters exist for a variety of formats. Popular commercial mesh formats as produced by STAR-CCM+, ANSYS FLUENT have convenient mesh converters to OpenFOAM format. Although these software packages are available, the mesh generator of choice was the SnappyHexMesh utility supplied with OpenFOAM. This section is included in the thesis to clarify concepts and parameters relevant to the computational grid in the present numerical study of flow past curved cylinders.

3.1 Grid Generation in SnappyHexMesh

The SnappyHexMesh utility is quite flexible and intended as an automatic mesh generator for an arbitrary geometry. With great generality comes a control file with many control parameters to be set by the user. Different geometrical setups often require tweaking of control parameters on an experimental basis until an acceptable mesh is achieved. For the curved cylinder geometry investigated here, once a good control setup is achieved for one case, SnappyHexMesh is quite predictable and stable for alterations like additions of straight cylinder extensions or changing radius of curvature.

A discussion of every detail of SHM is not included in the present study as proper documentation lacks and SHM is very complex. An important goal with this thesis is to provide a basis for further work with the tools used, and this will still be possible. The most important overall aspects of how SHM works and some challenges related to the present problem are discussed. Further the configuration file containing the best obtained settings for the curved cylinder is included in the attached files for easy continuation of the work, along with PDFs of online resources.

The input for SnappyHexMesh is a background mesh (a hexahedral mesh confining the whole domain to be investigated) and geometry parts defined by a triangulated approximation to the actual analytical surface of the geometry, in

Stereolithography format also known as the .stl file format. The background mesh is simply made with the OpenFOAM utility BlockMesh, and the cylinder gemoetry is designed in the CAD software Rhinoceros. Any CAD software able to export .stl will do, as long as one can specify the refinement of the exported geometry mesh, which should be rather fine.

The CAD-model is designed in three separate parts, i.e. the vertical extension, horizontal extension and the curved cylinder are defined separately, even though SHM supposedly have the ability to split up .stl-geometries (OpenFOAM 2018b). The geometry is divided so that forces can be tracked on each part separately in OpenFOAM. Figure (7) illustrates the cylinder CAD model, visualized in ParaView.

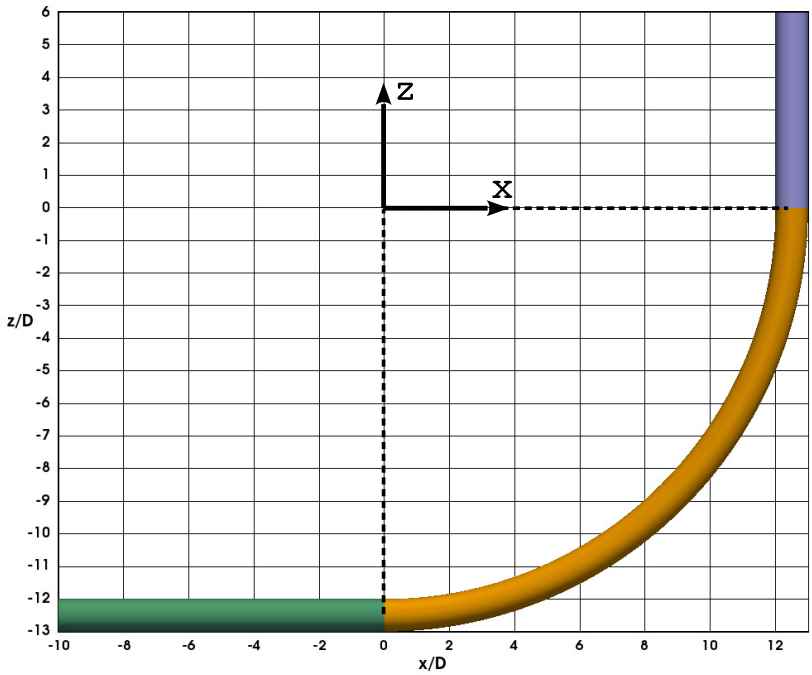

Figure (7): CAD model of the divided geometry of the curved cylinder configuration. Curved part ( ); horizontal part ( ); vertical part ( ).

Another advantage of this separation is that cylinder parts can be put together

to define any configuration of horizontal extension lengths, vertical extension lengths and radius of curvature. This is convenient for fast design of various configurations, making the investigation of different geometrical parameters more efficient.

A prerequisite for the SnappyHexMesh to work is that there exists a background mesh consisting of hexahedral elements. For stable performance of SHM, the background mesh must be approximately cubic in the whole domain, or at least near the geometry. The idea of a background mesh covering the computational domain and the cylinder geometry is visualized in figure (8). The cylinder horizontal and vertical extension is defined all the way to the inlet and the top boundary respectively.

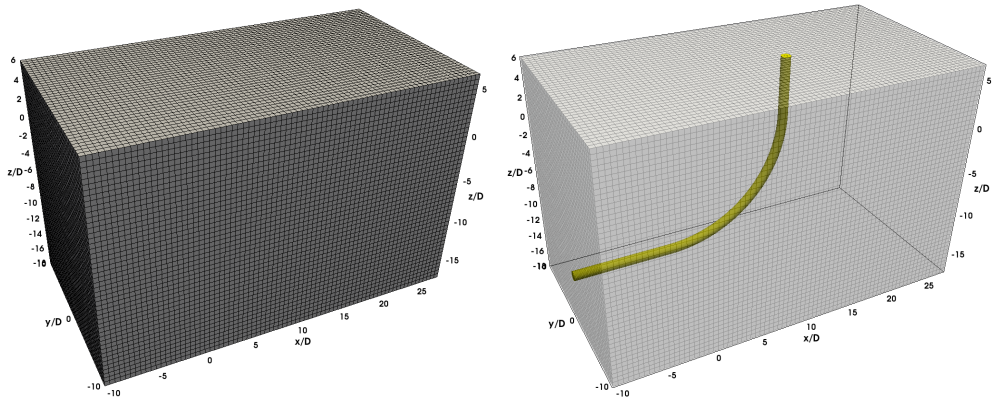

Figure (8): **Left:** Overview of the background mesh defining the boundaries of the computational domain. **Right:** Overview of background mesh confining the whole cylinder geometry.

From the geometry and background mesh, SnappyHexMesh works with its input in three steps, given below.

- Castellation step.
- Snap step.
- Add layers step.

3.1.1 Step 1: Castellated Mesh

The castellated mesh is the first approximation of mesh generation close to the surface geometry. The background mesh cells are split in half in x-, y- and z-direction inside and around the geometry-background mesh intersection a number of times specified by the user. This number, say N_{refLvl}, defines the near geometry refinement level. The background mesh is then refined or split according to equation (23) given for the x-direction.

$$\Delta x_{refined}(N_{refLvl}) = \Delta x_{background} \cdot (\frac{1}{2})^{N_{refLvl}} \tag{23}$$

Where $\Delta x_{refined}$ is the cell size in x-direction after refining the background mesh cell $\Delta x_{background}$ to level N_{refLvl}. Figure (9) illustrates how the level refinement works from the background BlockMesh to, in this example, a refinement level of $N_{refLvl} = 3$. The resulting castellated mesh is shown in practice for the domain top boundary of a curved cylinder with a vertical straight extension indicated in transparent yellow.

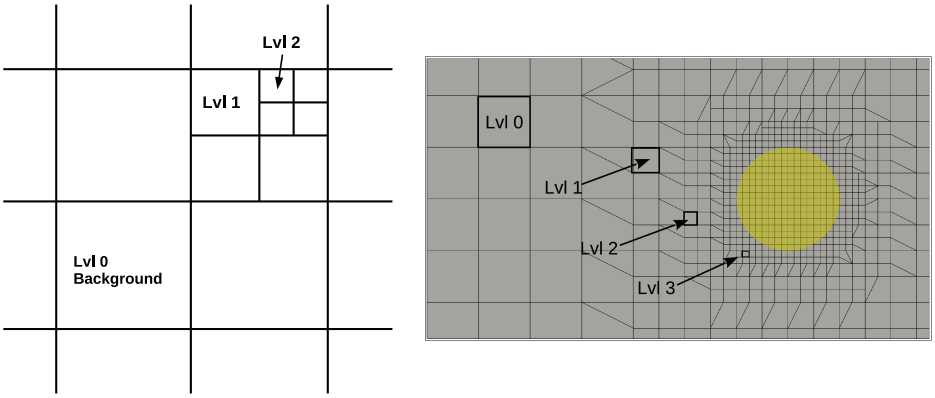

Figure (9): **Left:** Illustration of cell refinement in the castellation step. N_{refLvl} is indicated by "Lvl". **Right:** Castellated mesh around a circular cylinder. Cylinder geometry indicated in yellow.

This level of refinement will obviously result in a quite coarse representation of the geometry, and in turn a bad boundary layer mesh later.

3.1.2 Step 2 and 3: Snapping and Layer Mesh

The next two steps involves the operation of **step 2**; geometrically altering the cells made close to the geometry in **step 1** to obtain a better fit to the geometry ("snapping" to geometry), and **step 3**; add more cells close to and following the geometry in a smooth fashion with multiple layers radially outwards from the cylinder ("layer mesh" generation).

The "snapped" mesh and the resulting mesh after the addition of three mesh layers around the cylinder is shown in figure (10). It is evident that the castellated and snapped mesh highly influences the regularity of the boundary layer mesh, which in this case is quite rough as it poorly represents the geometry and is somewhat irregular. The number of cells left around the circumference of the straight cylinder parts are now very much countable and apparently the level 3 refinement amounts to 48 cells around the circumference. Keep in mind that the relation between refinement levels and circumferential resolution also is dependent on the size of the background mesh size, which in this case is $[\Delta x, \Delta y, \Delta z]_{background} = [0.5, 0.5, 0.5]D$.

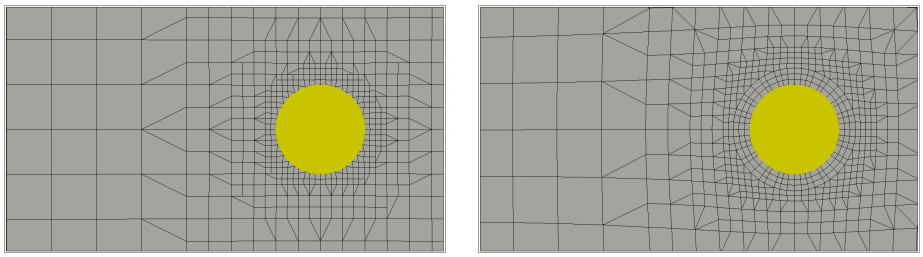

Figure (10): **Left:** Castellated mesh "snapped" to cylinder geometry. Cylinder geometry indicated in yellow. **Right:** Insertion of layer mesh around the cylinder.

Both the snapping and layer addition alters the grid cells nearby. The snapping utility "stretches" and "squeezes" cells close to the geometry such that a nice fit is obtained, whereas the layer addition actually makes room for the layers by pushing the snapped cells (as well as other surrounding cells) outwards from the geometry. This process was found to be the main contributor to non-

orthogonality and skewness in the grid, as especially the squeeze of cells from the snapping process is further increased. This is viewed in the figure (11) below. The squeezing of cells may easily trigger SHM to collapse the boundary layer mesh when cells become too deformed.

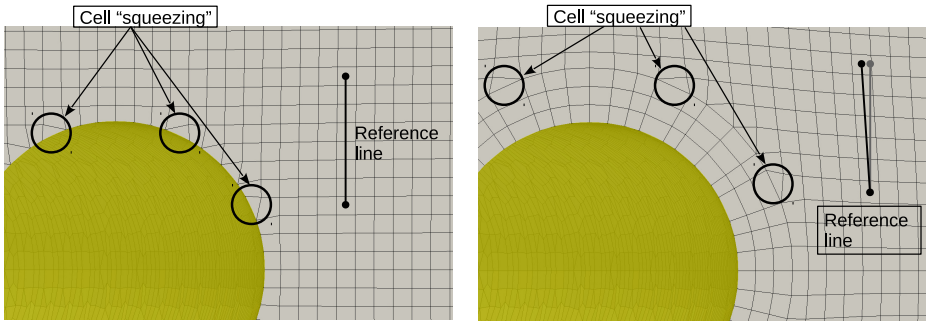

Figure (11): **Left:** Cell squeezing during **step 2**, where the most affected cells are indicated by O. A reference line extending vertically with endpoints in two cells are indicated. **Right:** The same cells further squeezed in **step 3** and reference lines showing cell-to-cell path before (—●) and after (—●) layer addition. Notice the distortion of cells.

The main parameters controlling the layer addition are: number of layers radially, the layer thickness in the layer farthest from the geometry and cell size expansion ratio. Either the closest layer size or the farthest layer size can be used as a reference when including cell expansion in the layers, and the reference cell size may be specified relative to the closest non-layer cell (*relativeSizes* = *true*) or as an absolute size (*relativeSizes* = *false*). The combination of specifying the farthest layer size (*finalLayerThickness*) using relative sizes was found to be the most stable, as one is guaranteed that δ_{final} is in a reasonable size relative to Δ and the collapsing of layers is less likely to happen (definitions in figure (12)).

An illustration of layers added close to a geometry and the different layer thicknesses using a cell expansion away from the body is shown in figure (12).

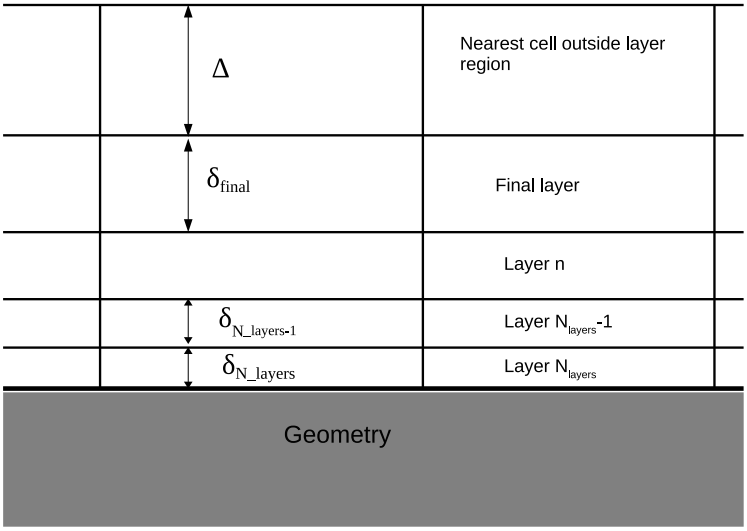

Figure (12): Illustration sketch of the layer sizes with respect to outer mesh. δ_{final} defines the outermost layer thickness according to equation (24), Δ is the nearest non-layer grid cell and δ_N is the layer closest to the geometry.

The equation for the final layer thickness δ_{final} (farthest from the geometry) is defined as in equation (24), where Δ is the size of the cell nearest to the final layer and ζ is the ratio between them.

$$\delta_{final} = \zeta \cdot \Delta \tag{24}$$

Further the cell expansion ratio er in the layers is used to determine the thickness δ_n of each layer n as n increases towards the geometry. This is illustrated in figure (12). Equation (25) defines the thickness of each cell where $n \in 1, 2, 3, ..., N_{layers} - 2, N_{layers} - 1$. Where N_{layers} is the total number of layers specified including the final layer.

$$\delta_n = \delta_{final} \cdot \frac{1}{er^n} \tag{25}$$

The layer addition was found to be most stable for low expansion ratios $er \in$

$[1.01, 1.1]$, and a good starting point for the layers was $\zeta = \delta_{final}/\Delta \in [0.8, 1.0]$.

3.1.3 Refinement Regions

SnappyHexMesh also offers the possibility of defining regions in the domain where user specified refinement levels are applied, and this functionality is strictly speaking a part of **step 1** as it appears under the same control section in the snappyHexMeshDict. The same definitions for refinement as discussed in (3.1.1) is applied in the refinement regions. In figure (13) the different regions are illustrated for the refinement in the near wake, far wake, and in the layer mesh close to the cylinder. The background mesh is also visible in the bottom domain and near the inlet. The layer mesh and the refinement region at the horizontal extension (bottom left of figure (13)) appears exactly the same, since in this case the refinement level of the refinement region is the same as that used for resolving the geometry and the horizontal part is parallell with the cells.

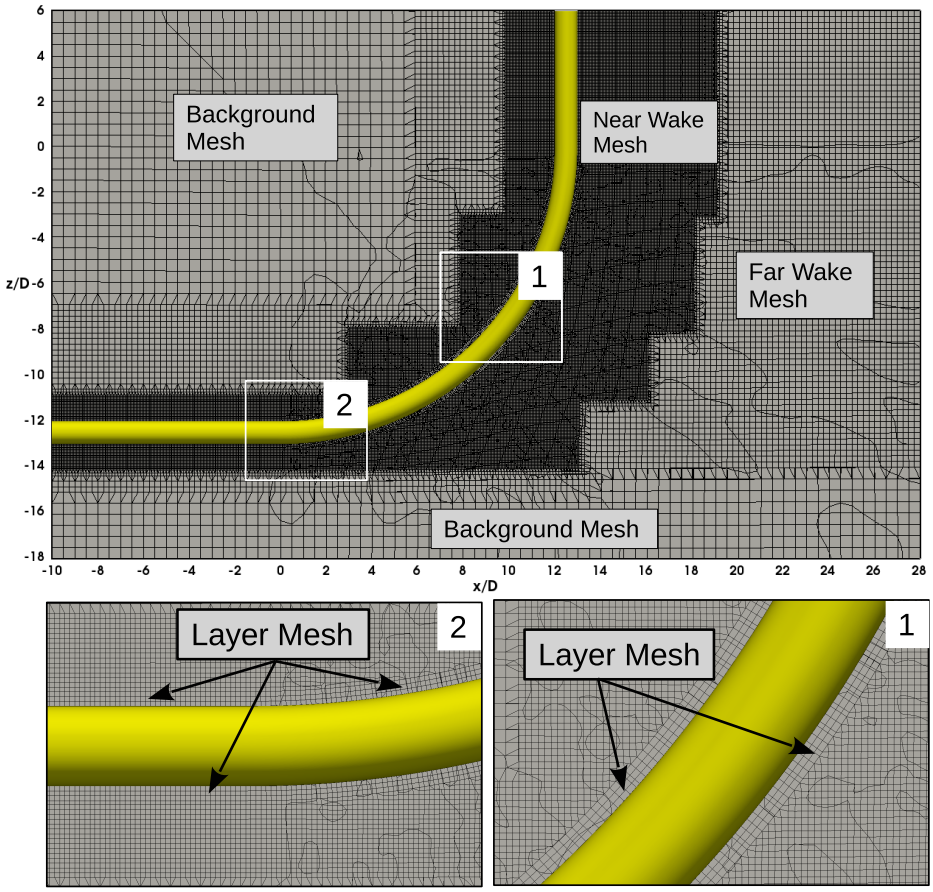

Figure (13): **Top:** The plane $(x, y, z) = (x, 0, z)$ showing the refinement regions in the near and far wake of the cylinder. **Bottom:** Close up view of the layer mesh as it turns out in the straight extensions and the curved part.

3.2 Simulation Parameters and Numerical Setup

Now that the grid generator is known, the parameters used in the numerical setup is introduced in this section for later reference. Geometrical parameters are presented in section (3.2.1), definitons of variables as well as the normalization practices are given in (3.2.2) and the implementation of boundary conditions is found in section (3.2.3).

3.2.1 Geometrical Parameters

The overall picture of the domain is presented in figure (14), an overview of the grid and refinement regions in figure (15) and an explanation of parameters found in the figures are given in table (3). The layout presented here establishes the "template" for all simulations in the present thesis.

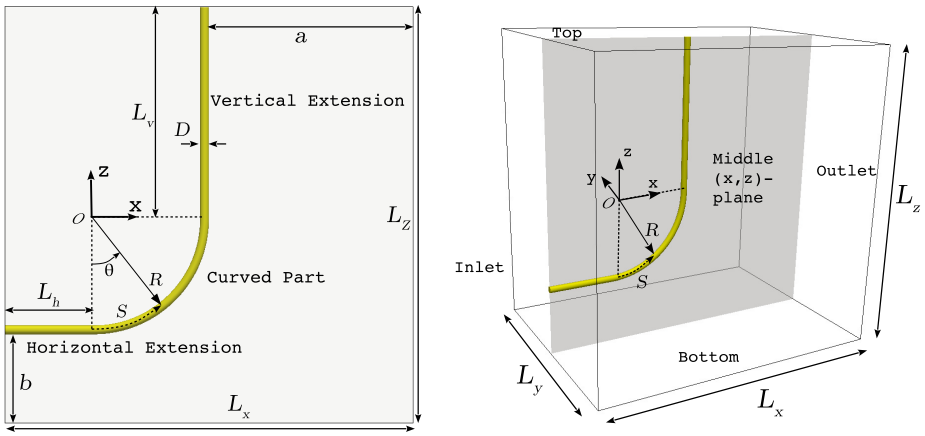

Figure (14): **Left:** Geometrical configuration and definitions in the centre (x, z)-plane. **Right:** Perspective view of the three-dimensional computational domain indicating centre (x, z)-plane.

Table (3): Explanations of parameters related to domain, grid and geometry.

Parameter	Explanation
L_h	Length of horizontal cylinder extension.
L_v	Length of vertical cylinder extension.
R	Radius of curvature of curved cylinder part.
D	Cylinder diameter.
L_x	Domain length in x-direction.
L_y	Domain width in y-direction.
L_z	Domain Height in z-direction.
θ	Angular ordinate along the curved part.
S	Spanwise ordinate along the curved part.
L_{nF}	Downstream length of the nearfield grid resolution.
W_{nF}	Width along y-axis of the nearfield grid resolution.
a	Downstream length of the wake/farfield grid resolution.
W_{fF}	Width along y-axis of the farfield grid resolution.
b	Distance from cylinder bottom to lower domain boundary.
N_{layers}	Number of boundary layer elements radially.
t_{BL}	Total boundary layer mesh thickness.
$N_{cellsTot}$	Total number of cells in the domain.
$N_x/N_y/N_z$	Number of cells in x-, y- and z-direction.
cylRefLvl	Refinement level around the cylinder.
nfRefLvl	Refinement level in the nearfield grid.
ffRefLvl	Refinement level in the farfield grid.

In figure (15) a visual overview is given of how the refinement regions are defined according to table (3). Notice that the total wake length a is the same as what would be the farfield wake region length, since the farfield refinement is chosen to always extend to the end of the domain. The top domain boundary face, the (x, z) centre plane, the inlet boundary face and the outlet boundary face can be seen.

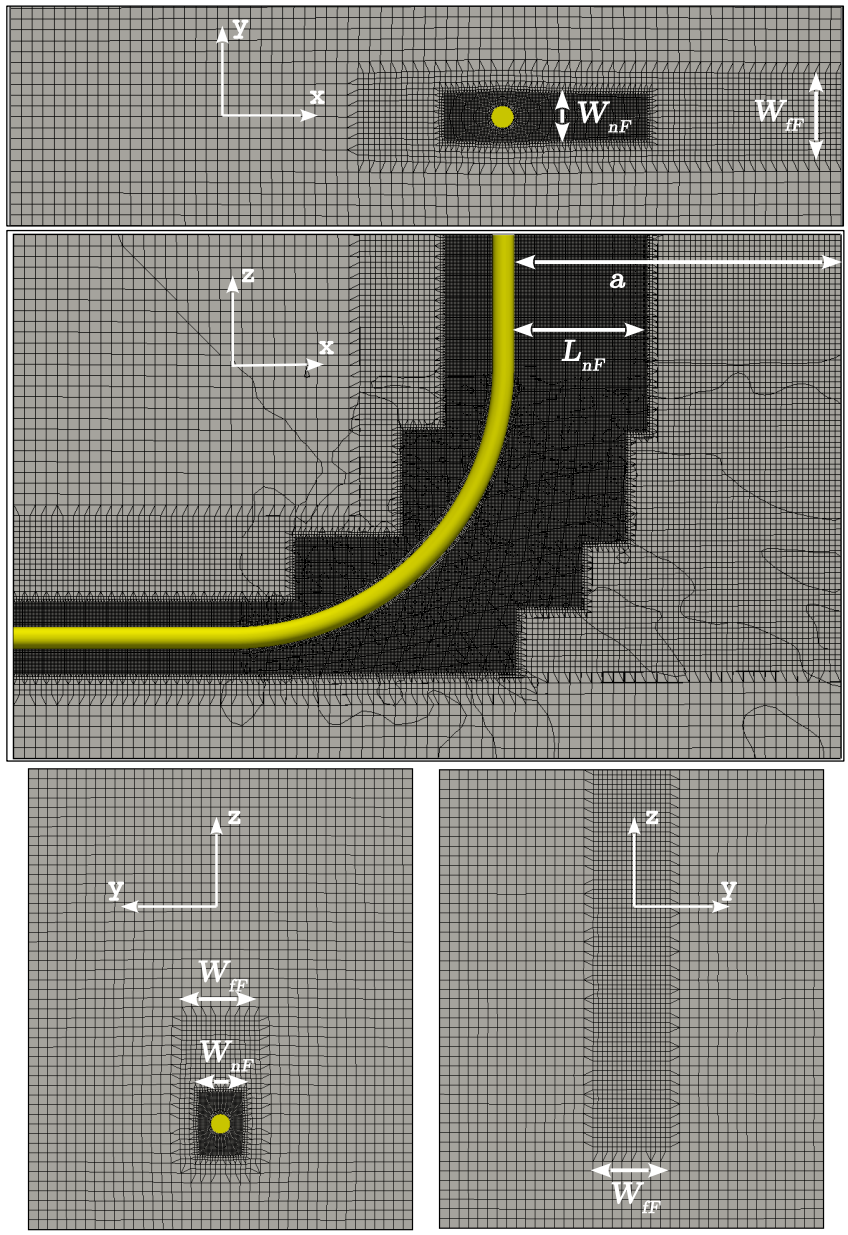

Figure (15): **Top:** Part of the top boundary indicating nearfield and farfield mesh widths, W_{nF} and W_{fF}. **Middle:** Centre (x, z)-plane showing the nearfield length L_{nF} and total wake length a. **Bottom Left:** Inlet plane indicating W_{nF} and W_{fF}. **Bottom Right:** Outlet plane indicating W_{fF}.

3.2.2 Variables and Normalization

The raw data outcome of the CFD-solutions are u, v, w and p. For clarity in results and comparison purposes flow variables are normalized on characteristic constant properties of the numerical setup. The normalization of the variables may take different forms depending on the configuration studied in this thesis (mainly depending on inflow velocity).

The **inflow velocity** is given by the constant uniform free stream U_0. In case of the shear flow the linearly varying free stream $U_0(z)$ is defined. We have in addition the median of the velocity profile U_c and the velocities at the ends of the profile given by U_{bottom} and U_{top}. This is further illustrated in section (6).

The overall flow Reynolds number is defined as equation (26)

$$Re = U_0 D/\nu \tag{26}$$

based on the uniform free stream and equation (27)

$$Re_c = U_c D/\nu \tag{27}$$

based on the centre median velocity in a shear profile. The kinematic viscosity is now $\nu = \mu/\rho$ $[m^2/s]$, where μ is the dynamic viscosity and $\rho = 1000$ $[kg/m^3]$ is the mass density of the fluid. To obtain the required Re for each case, viscosity is adjusted to $\nu = 0.01$ and the inflow velocity is set according to the Re wanted, e.g. $\nu = 0.01$ and $U_0 = 3.5$ giving a $Re = 350$. It is important to notice that OpenFOAM uses a mass density $\rho = 1$ in the computations. A spanwise varying local Reynolds number in equation (28) is defined for the shear flows.

$$Re_l(z) = U_0(z) D/\nu \tag{28}$$

Velocities output from the simulations are further normalized with respect to either U_0 or U_c during post-processing. Regarding the **pressure**, OpenFOAM

solves for a kinematic pressure p $[m^2/s^2]$ as in equation (29)

$$p = P/\rho \tag{29}$$

relative to a reference pressure calculated near the inlet (user specified), where P $[N/m^2]$ is the fluid pressure. During post-processing this p is normalized such that a non-dimensional pressure is obtained as in equation (30) or of course equation (31) for shear flow. Notice that many normalizations utilize the fractor of "1/2" in the denominator, however this is absent for the pressure term in the present study.

$$P^* = p/U_0^2 = P/\rho U_0^2 \tag{30}$$

$$P^* = p/U_c^2 = P/\rho U_c^2 \tag{31}$$

During post-processing other kinematic properties of the solution flow field are calculated to obtain a fuller picture of the flow structure. An essential property is the **vorticity field $\boldsymbol{\omega}$** defined as twice the angular velocity field (White 2006). In vector calculus vorticity is related to the curl of the velocity field by equation (32).

$$\boldsymbol{\omega} = \boldsymbol{\nabla} \times \mathbf{U} \tag{32}$$

The vorticity field vector is given as (33)

$$\boldsymbol{\omega} = [\omega_x, \omega_y, \omega_z] \tag{33}$$

where equations (34a), (34b) and (34c) defines the components in x, y and z.

$$\omega_x = \frac{\partial w}{\partial y} - \frac{\partial v}{\partial z} \tag{34a}$$

$$\omega_y = \frac{\partial u}{\partial z} - \frac{\partial w}{\partial x} \tag{34b}$$

$$\omega_z = \frac{\partial v}{\partial x} - \frac{\partial u}{\partial y} \tag{34c}$$

The vorticity components identifies vortices in its respective direction, however to get a broader view of the vortex structures in the flow field, the method of identifying vortex cores of a certain strength no matter direction is adopted in this study. The method was developed by (Jeong and Hussain 1995) and is based on extracting vortex cores directly from the instantaneous velocity field. The velocity gradient tensor is given on tensor notation as equation (35) (White 2006), where i, j are any two coordinate directions.

$$U_{i,j} = \frac{\partial U_i}{\partial x_j} = \underbrace{\frac{1}{2}(U_{i,j} + U_{j,i})}_{symmetric} + \underbrace{\frac{1}{2}(U_{i,j} - U_{j,i})}_{anti-symmetric} \tag{35}$$

Letting $\epsilon_{i,j}$ represent the strain rate tensor (*symmetric*) part and $\dot{\Omega}_{i,j}$ represent the angular velocity (*anti-symmetric*) part of equation (35) (Jeong and Hussain 1995) found that vortices are well-represented by connected regions where the second-largest eigenvalue λ_2 of the tensor $\epsilon_{i,j}\epsilon_{j,i} + \dot{\Omega}_{i,j}\dot{\Omega}_{j,i}$ is negative.

Further derived quantities include forces on the cylinder configuration. Force coefficients are calculated by OpenFOAM from the integrated pressure over the cylinder surface and normalized. The force in x- and y-direction F_x and F_y respectively are normalized according to equation (36) and (37). The coefficients represent drag (C_D) and lift (C_L) force on the cylinder configuration.

$$C_D = \frac{F_x}{\frac{1}{2}\rho U_0^2 A_{ref}} \tag{36}$$

$$C_L = \frac{F_y}{\frac{1}{2}\rho U_0^2 A_{ref}} \tag{37}$$

Where U_0 is the free stream velocity (U_c is used for shear flow) and A_{ref} is the projected area of the cylinder in the direction of the free stream. The projected area is calculated as $A_{ref} = (R + D/2 + L_v)$.

Simple statistical quantities are calculated for the force coefficients. The time average of the drag and lift coefficient is given as equation (38) and (39) respectively.

$$\overline{C_D} = \frac{1}{N_T} \sum_{i=1}^{N_T} C_{D,i} \tag{38}$$

$$\overline{C_L} = \frac{1}{N_T} \sum_{i=1}^{N_T} C_{L,i} \tag{39}$$

Where the summation runs from the first element of the time series of the coefficients to the total number of elements in the time series N_T. The C_L oscillates around a mean of $\overline{C_L} \approx 0$ depending on the length of the time series, so a reasonable statistic for the oscillating lift coefficient is the root-mean-square $C_{L,rms}$ calculated as equation (40).

$$C_{L,rms} = \sqrt{\frac{1}{N_T} \sum_{i=1}^{N_T} \left(C_{L,i} - \overline{C_L}\right)^2} \tag{40}$$

3.2.3 Boundary Conditions

To solve the Navier-Stokes equations on a computational grid, boundary conditions (BCs) are required for the flow variables at all boundaries of the domain. Here the implemented boundary conditions are presented with respect to the boundary names given in figure (14). The Finite Volume Method requires that the boundary fluxes either be known or expressed in terms of known quantities

and interior nodal values (Ferziger 2002). Boundary conditions differ by whether a flow variable is prescribed on the boundary directly (Dirichlet BC) or that the rate of change of the variable (or the gradient) across the boundary is specified (Neumann BC).

Inlet and Outlet

Inlet and oulet boundaries are the most complicated to specify since usually all values must be known and prescribed at inlets and it is hard to say much apriori about the flow at the outlet. Another issue is the pressure-velocity coupling and the interaction with inlet and oulet conditions. A common approach for incompressible flows are to prescribe a velocity inlet and extrapolate to the outlet (Ferziger 2002). This method is applied here.

The *outlet* BCs implemented are:

- Neumann condition for velocity:

$$\frac{\partial u}{\partial x} = \frac{\partial v}{\partial x} = \frac{\partial w}{\partial x} = 0 \tag{41a}$$

- and zero-pressure condition:

$$p = 0 \tag{41b}$$

The *inlet* BCs implemented are:

- Dirichlet condition for uniform velocity:

$$u = U_0 \tag{42a}$$

- or a Dirichlet condition for a shear velocity profile:

$$u(z) = U_0(z) \tag{42b}$$

Top, Bottom and Vertical Sides

The top, bottom and sides are all given slip-type boundary conditions, i.e. a symmetry condition for all flow variables. This means physically that the boundaries are impermeable to mass-flow/velocities and pressure, however the flow is allowed to run tangentially along the boundary.

Mathematically the conditions implemented on the horizontal *top* and *bottom* planes are:

- Free-slip condition for velocity:

$$w = 0 \text{ and } \frac{\partial u}{\partial z} = \frac{\partial v}{\partial z} = 0 \tag{43a}$$

- Neumann pressure condition:

$$\frac{\partial p}{\partial z} = 0 \tag{43b}$$

The *vertical sides* at $(y/D = \pm L_y/2)$:

- Free-slip condition for velocity:

$$v = 0 \text{ and } \frac{\partial u}{\partial y} = \frac{\partial w}{\partial y} = 0 \tag{44a}$$

- Neumann pressure condition:

$$\frac{\partial p}{\partial y} = 0 \tag{44b}$$

Cylinder Surface

The cylinder surface is modelled as a "solid wall", i.e. impermeable and imposed no-slip condition at the surface. The implementation reads as follows:

- No-slip and impermeability condition for velocity:

$$\mathbf{U} = \mathbf{0} \tag{45a}$$

- Neumann pressure condition (where n_s is the surface normal):

$$\frac{\partial p}{\partial n_s} = 0 \tag{45b}$$

3.3 General Thoughts and Comments On This Chapter

- The boundary layer mesh might be improved significantly by creating a thicker boundary layer mesh. This might be accomplished by the same expansion ratio and increased number of layer cells. This will rapidly increase the total cell count in the domain and might not be beneficial in the end.
- Another way to increase layer thickness without a huge increase in cell numbers, is to use absolute sizes and a higher expansion ratio. This way the cell closest to the body could be specified sufficiently small to get a good layer thickness at a reasonable number of cells. The problem with standard SHM is that when the layer thickness and/or layer cells become too large, the algorithm for moving the outer mesh away from the body fails. The result is usually a collapse of the layer mesh. The reason is that the deformation (cell squeezing) of outer mesh cells becomes too severe and SHM "fixes" the bad cell problem by collapsing the layer mesh rather than removing bad cells.
- A version of OpenFOAM with the suffix "+" as in "OpenFOAM v1612+" exists. This version is supposed to include SHM with a better algorithm for moving cells when making room for the boundary layer elements. Supposedly SHM is able to prioritize the layer mesh and rather remove other bad cells causing trouble. This might be worth trying to create a higher quality boundary layer mesh without severely increasing total cell count.
- Another tool for creating body-fitted grids to complex geometries is called CF-Mesh which works in a similar way as SHM. This is not investigated further in the present study and the benefit of this software is unknown to the author.
- Possible mesh generators are of course the ones issued with ANSYS Fluent,

and with STAR-CCM+.

- Notice that the the built-in post-processor in OpenFOAM calculates and outputs $-\lambda_2$.

4 Grid Independence Study

The choice of a computational domain and the generation of a grid is essential for a CFD study, and the quality of a CFD solution is highly dependent on the quality of the grid (Çengel 2014). Therefore it is necessary to have a certain confidence about the chosen grid setup before proceeding to the solution of the actual problem.

This procedure of deciding on a computational grid is in the literature often termed a *grid independence study*. Grid refinements locally where high gradients in the flow are expected, overall cell refinement in the domain and increase of domain size are common focus points of the grid study.

High flow gradient areas typically include boundary layer regions near solid walls where the flow velocities range from zero at the wall to the free stream velocity outside the boundary layer. Flow past bluff bodies exhibit large flow gradients in the wake as well, due to flow separation. In the present study natural refinement regions are therefore in the near and far wake of the cylinder configuration, and in the boundary layer across the whole cylinder geometry. The effect of domain size on the flow solution is an important issue in CFD as well as in experimental fluid dynamics and the concept usually goes by the name of "blockage". For CFD blockage depends on the choice of conditions set on the domain boundaries and the size of the domain. The effect of boundary conditions vanish when the boundaries are sufficiently far from the main flow dynamics.

Important domain size parameters in the present study not defined by cylinder geometry are the width along the y-direction L_y, the gap b between the lower domain boundary and the horizontal extension, and the wake length a. Domain parameters associated with the cylinder geometry are inlet length (horizontal extension) and the vertical height (vertical extension).

The horizontal and vertical extensions should be included for relevance to practical offshore and subsea engineering as the curved part rarely exist isolated. As the cylinder has a free end in two boundaries, i.e. the inlet and the top boundary, it is beneficial to include a long enough horizontal extension to ensure a fully

developed boundary layer flow before reaching the curved part. The vertical extension ends in the top boundary, which limits any vertical velocity component that might be present. (F. Jiang, B. Pettersen, and H. I. Andersson 2018) found that a horizontal extension of $L_h = 10D$ prevents any disturbances from the inlet/cylinder intersection from reaching the curved part. Unpublished DNS data from the same author (F. Jiang, B. Pettersen, H. I. Andersson, et al. 2018) indicates strong axial flow along the cylinder span which is still up to 20% of the free stream velocity even at $z/D = 20$, depending on the Reynolds number. The strength of the axial flow along the concave cylinder was also indicated in (Miliou et al. 2007) where only $L_v = 6D$ was used. A suppression of the vortex shedding in the vertical extension compared to a regular straight cylinder was found. The axial flow becomes parallel to the free stream when it reaches the slip wall top boundary and acts as a base bleed mechanism similarly as investigated by (Bearman 1967).

In addition, grid cell quality and non-orthogonality are important parameters for assessing the grid effect on the solution, however due to little control over these parameters in SHM these parameters are not investigated.

4.1 Measure of the Flow Solution

As problems in CFD rarely have exact analytical solutions, the grid independence study should aim at finding the numerical setup where the solution is approximately unaffected by further refinements. Flow variables u, v, w and p are natural measures of the solution. Derived quantities such as the forces acting on the cylinder (pressure and viscous stresses integrated over the cylinder surface) and statistics related to them are also good indicators of the overall solution.

This present grid study measures and assesses the overall solution defined by:

Velocity

- Time averaged axial flow in the near wake along the cylinder span U_{ax} measured along a concentric arc of the curved cylinder, with radius of $14D$, and along the vertical extension at $x/D = 14$. I.e. the flow is measured at

$1D$ behind the cylinder trailing edge.

- Vortex shedding frequency distribution along the vertical extension measured as oscillations in v velocity signal at $x/D = 16$, i.e. $3D$ behind the trailing edge of the cylinder.

Forces

- Root-mean-square of the lift force coefficient $C_{L,rms}$.
- Time averaged drag force coefficient $\overline{C_D}$.
- Normalized lift force oscillation frequency f^*_{peak}.

4.2 M-series

The M-series are defined in the following tables (4) and (5) and are simulation cases made of the base setup given below:

Parameter	
Configuration	Concave
L_h	$10D$
R	$12.5D$
L_v	$6D$
Inflow	Uniform $Re = 500$

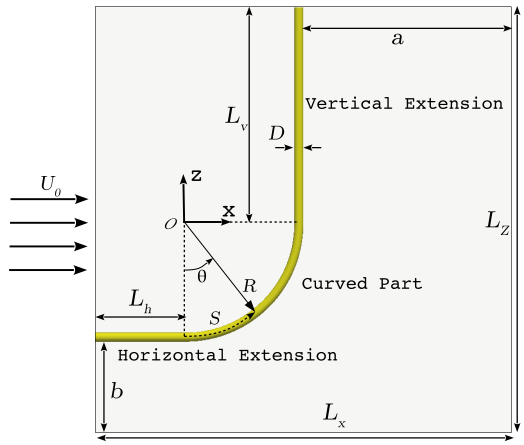

Figure (16): Basis flow configuration used in the grid study (M-series) simulations. All tests are derived from this setup.

The horizontal extension is chosen based on (F. Jiang, B. Pettersen, and H. I. Andersson 2018). The vertical extension is chosen for minimizing the computational efforts while having a comparable case to earlier studies by (Miliou et al. 2007) and (F. Jiang, B. Pettersen, and H. I. Andersson 2018).

The aim here is not to catch any meaningful flow physics (although one could argue that the setup resembles a curved cylinder near a free surface), but to carefully investigate grid parameters to find a grid and domain setup that is reasonably accurate and not too computationally demanding. The Renyolds number of $Re = 500$ is chosen for the grid study, since this is the upper limit to be investigated in the present study. It is thus assumed that the final grid is sufficient to capture relevant flow dynamics in all cases below and including this Re.

The simulations were each run $t^* = 100U_0/D$ dimensionless time units to ensure a developed flow. Then data was gathered every $\Delta t^* = 0.05U_0/D$ for $1000U_0/D$

time units, yielding 20000 data points for each variable in the time series.

4.2.1 Grid Parameters and Definitions

Table (4) describes the main parameters defining the geometry of the computational domain and refinement regions. All parameters are described in section (3.2).

M01, M02 and M03 are equivalent with respect to domain and region sizes, while M04 represents an extension of these domains by making the size of the wake regions larger. That is nearfield region width, farfield region width and wake length are extended considerably. Further M05 is also equivalent to the first three domains, except that the distance from the lower part of the cylinder to the lower boundary is increased from $5D$ to $10D$. Finally the M06 and M07 represents a wake region extension from M05, in the same manner as M04 was constructed.

Table (4): Geometrical parameters of various M-series setups. Horizontal extension length L_h/D; vertical extension length L_v/D; radius of curvature R/D; nearfield length L_{nF}/D; nearfield width W_{nF}/D; farfield width W_{fF}/D; total wake length a/D; distance to lower boundary b/D; domain width c/D

Case	L_h/D	L_v/D	R/D	L_{nF}/D	W_{nF}/D	W_{fF}/D	a/D	b/D	L_y/D
M01	10	6	12	6	3	5	15	5	24
M02	10	6	12	6	3	5	15	5	24
M03	10	6	12	6	3	5	15	5	24
M04	10	6	12	6	4	6	23	5	36
M05	10	6	12	6	3	5	15	10	24
M06	10	6	12	6	4	6	23	10	36
M07	10	6	12	6	4	6	23	10	36

It is further elaborated on M-series differences in table (5). The different M-series cases are differentiated with respect to refinement levels in the different regions, number of cells in total, boundary layer mesh thickness and the distribution of elements in the background mesh.

Table (5): Number of cells and refinement levels used in M-series. Refinement level around the cylinder *CylRefLvl*; refinement level in nearfield wake *nfRefLvl*; refinement level in farfield wake *ffRefLvl*; number of boundary layer elements outwards from the cylinder N_{layers}; total boundary layer mesh thickness t_{BL}/D; total amount of cells in domain $N_{cellsTot}$; N_x, N_y and N_z number of cells in x-, y- and z-direction for the background mesh.

Case	CylRefLvl	nfRefLvl	ffRefLvl	N_{layers}	t_{BL}/D	$N_{cellsTot}$	$N_x/N_y/N_z$
M01	5	3	2	15	0.222	$9.3 \cdot 10^6$	70/40/44
M02	4	3	2	12	0.366	$4.2 \cdot 10^6$	70/40/44
M03	4	2	1	12	0.366	$1.9 \cdot 10^6$	70/40/44
M04	4	3	2	12	0.366	$7.2 \cdot 10^6$	92/72/48
M05	4	3	2	12	0.366	$5.8 \cdot 10^6$	76/48/58
M06	5	3	2	12	0.169	$12.5 \cdot 10^6$	92/72/58
M07	4	3	2	12	0.366	$7.2 \cdot 10^6$	92/72/58

From table (5) the refinement level around the cylinder surface is held at either $CylRefLvl = 4$ (in M02, M03, M04, M05 and M07) or at $CylRefLvl = 5$ (in M01 and M06). The refinements in the wake are set at $nfRefLvl = 3$ and $ffRefLvl = 2$ for all cases except M03. This is because a higher level increases the total cell count considerably and becomes very computationally demanding, while a lower level is simply too coarse (as will be evident for M03 later). The total cell count effect is visible by comparing $N_{cellsTot}$ in M06 and M07 which differs only in *CylRefLvl* by 1 level and $N_{cellsTot}$ differ by $\sim 5.3 \cdot 10^6$ cells.

The $CylRefLvl = 5$ of M01 and M06 makes the refined cell size so small that a greater number of layers is required for the same layer thickness as obtained in the cases of $CylRefLvl = 4$.

The number of cells in the background mesh is chosen on the basis of having a sufficient number of cells in the z-direction. (H. Jiang et al. 2016) used $N_z/D = 10$ for their wake transition study of a straight cylinder in $Re \leq 300$, and in the present study the aim is to be at atleast $N_z/D \approx 20$ within the near field refinement region. The number of background cells in z-direction is then chosen to fulfill that requirement. The number of cells in x- and y-direction is chosen to get approximately cubic cells in the entire domain as discussed in section (3). The cylinder surface refinement level of 4 and 5 is equivalent to 186 and 364 elements around the cylinder circumference respectively. As the background mesh

is approximately cubic and $\Delta z_{background} \approx 0.5$, the result are the minimum grid sizes of $\Delta z_{refined}(N_{refLvl} = 4) = 0.03125$ and $\Delta z_{refined}(N_{refLvl} = 5) = 0.01563$.

The grids are not grouped in a very intuitive manner and the changes to the grid parameters are chaotic at first glance. Therefore a definition of three *paths* are given in figure (17). The paths represent three ways that one can move from grid M03 (coarsest) to either M06 or M07. Each next step in each path is supposedly an improved grid to the former. The grids M06 (extended domain and wake region, and *CylRefLvl* = 5) and M07 (extended domain and wake region, and *CylRefLvl* = 4) are then supposedly the "best" grids tested.

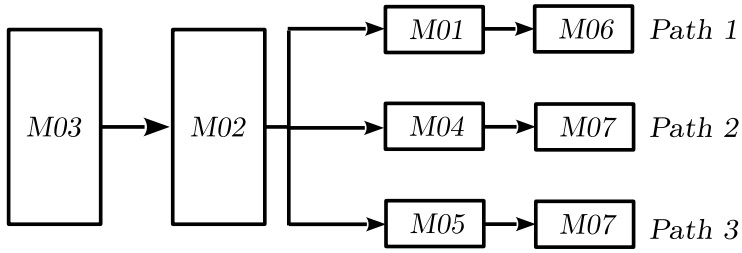

Figure (17): The *path* definition for tracking the effect of the various grids tested. M03 is the coarsest grid and hence the starting point. By moving to the right, "better" grids are obtained.

4.2.2 Force Coefficients

The force coefficients given as the root-mean-square of the lift force coefficient $C_{L,rms}$ and the time averaged drag coefficient $\overline{C_D}$ are presented in table (6) for the various grids tested. The dominating frequencies of oscillation in the time series of C_L are also presented as the normalized frequency $f^*_{peak} = f_{peak}D/U_0$. Coefficients and frequencies represent those of the forces on the total configuration.

Table (6): Results from the M-series force coefficient statistics and lift force frequency. $C_{L,rms}$ is the root-mean-square of the oscillating lift-force coefficient, $\overline{C_D}$ is the time averaged drag coefficient and f^*_{peak} is the dominating frequency of oscillation for the lift-force.

Case	$C_{L,rms}$	$\overline{C_D}$	f^*_{peak}
M01	0.0378	0.8523	0.1247
M02	0.0384	0.8776	0.1214
M03	0.0079	0.8043	0.1146
M04	0.0389	0.8683	0.1214
M05	0.0430	0.8835	0.1216
M06	0.0375	0.8500	0.1256
M07	0.0386	0.8672	0.1214

An immediate observation is that the results of the coarsest grid M03 deviates significantly from the other grids. The most affected quantity seems to be the $C_{L,rms}$ which for M03 lies $\sim 80\%$ below the average $C_{L,rms}$ of the other grids. The mean drag $\overline{C_D}$ lies $\sim 7\%$ below the average among the other grids.

For further differentiating the other grids the *path* definition is used in figure (18). Paths are arranged in columns where the three parameters investigated are listed below in rows. By moving from left to right along a row, the effect each path has on the chosen parameter can be followed. In addition values of the parameters for M06 and M07 are given explicitly in the plot.

The essence of figure (18) seems to be that there is a convergence towards the grids M06 and M07. However there is still a difference between the two, which then should be only the effect of the refinement around the cylinder and hence in the boundary layer. Both $C_{L,rms}$ and $\overline{C_D}$ are reduced from M07 to M06 while the frequency has increased. The absolute percentage change from M07 to M06 reads: $\sim 2.9\%$ for $C_{L,rms}$; $\sim 2.0\%$ for $\overline{C_D}$; $\sim 3.5\%$ for f^*_{peak}.

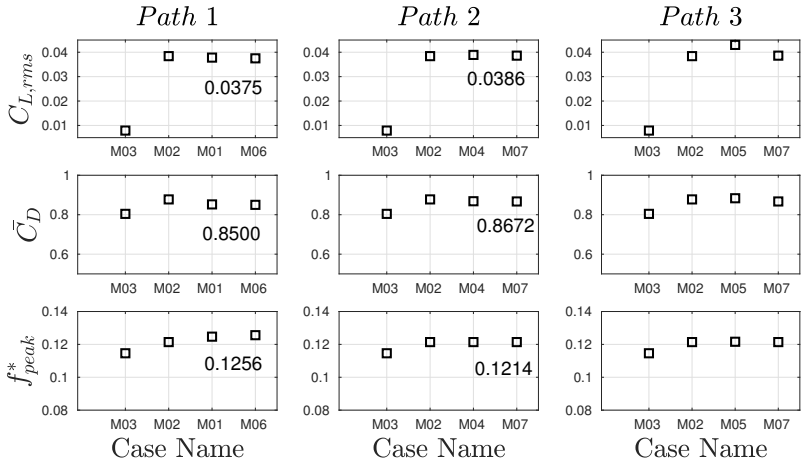

Figure (18): Plot matrix indicating the grid effect on the $C_{L,rms}$, $\overline{C_D}$ and $f^*_{peak} = f^*_{peak}D/U_0$. The path system of distinguishing each grids effect on the parameters is used. Each path is found column-wise, while the parameters are listed below in rows. In each subplot in the matrix the "better" grid lies to the right on the lower axis. The value of each parameter also stated in table (6) is given explicitly in the plot for M06 and M07.

The M06 simulation was run on 160 CPUs yielding ~ 78125 cells per process. With the current setup each time step is calculated in $\mathcal{O}(1)$ seconds (real time). The time step was $\Delta t^* = 0.002U_0/D$, which means that 500000 time steps must be calculated. This amounts to a total runtime of ~ 139 hours (real time), and a computational effort of 22240 CPU-hours.

The M07 grid was run on 96 CPUs with ~ 75000 cells/process. A time step of $\Delta t^* = 0.005U_0/D$ yielding 200000 time steps and a total runtime of ~ 45 hours, with a computational effort of 4320 CPU-hours.

4.2.3 Velocity Analysis

The v-component of velocity was logged in 7 points along the vertical extension. Starting at $z/D = 0$ and every $1D$ up to $z/D = 6$. The probes were placed at $x/D = 16$, i.e. $3D$ behind the trailing edge of the vertical cylinder. The dominating frequency component f^* was extracted from the time series of v with

a DFT approach and the distribution along the vertical span was found to be uniform[6] for all grids tested.

The figure (19) reveals that M03 is the only grid where small variations in f^* were found along the span. It is furthermore evident that the M-series are divided in roughly three groups with respect to dominant frequencies. M01 and M06 ($CylRefLvl = 5$) shows the highest frequencies in the test, while M03 shows the lowest frequency which is far from the other grids. M02, M04 and M05 (all $CylRefLvl = 4$) ends up around the same frequency in the middle. This is the same trend as observed in the lift force frequency f^*_{peak}, which is natural as the lift force was found to follow the shedding frequency exactly. Figure (19) indicates that shedding frequency is heavily influenced by the grid-refinement around the cylinder.

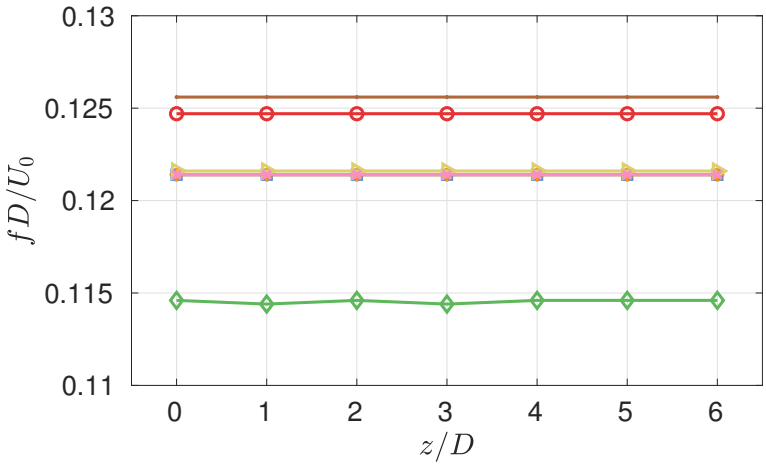

Figure (19): Spanwise distribution of shedding frequencies extracted from time series v at $3D$ behind the vertical extension. The distribution in each grid is shown: (), M01; (), M02; (), M03; (), M04; (), M05; (), M06; (), M07.

The direct comparison of dominating wake frequency f^* for each grid M01-M07 is found in figure (20).

[6] or approximately uniform in M03

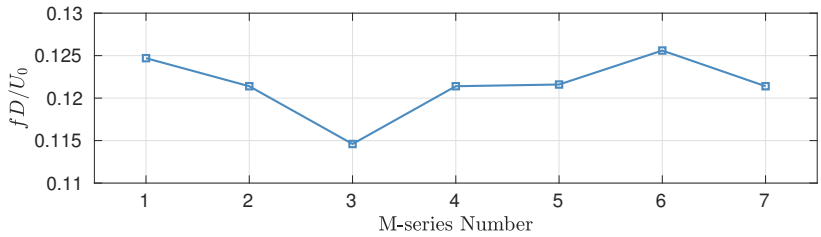

Figure (20): The dominating frequency in the wake of simulation M01-M07 obtained from a discrete Fourier transform of v at $3D$ behind the cylinder trailing edge. The frequency of v matches the lift-force oscillation frequency on the configuration exactly.

The velocity was logged by numerical probes along a concentric arc of the curved part in the centre plane which radius is $14D$ and a vertical line along the vertical extension at $x/D = 14$. The velocity component U_{ax}/U_0 which runs tangentially to the cylinder $1D$ downstream of the cylinder trailing edge was calculated from the velocity field by equation (46).

$$\frac{U_{ax}}{U_0} = \frac{u}{U_0}\cos(\theta) + \frac{w}{U_0}\sin(\theta) \tag{46}$$

Where U_0 is the free stream velocity and θ is the angular ordinate running along the curved cylinder part as depicted in figure (16).

The time averaged U_{ax}/U_0 along the curved part is presented in figure (21) for the various grids. The solution of grid M03 is once again clearly unable to capture even the overall trend correctly. The other grids however exhibit the same overall trends. The differences appear in the area around $\theta \approx 80° - 90°$, that is the intersection between the curved cylinder part and the vertical extension. The flow clearly is more complex around this intersection as the various grids capture different tendencies.

In the intersection area, the wake experiences a transition from a non-shedding regime to a shedding regime, as later will be shown in figure (33), and deemed to be computationally challenging. In other words, the transitional wake in this area can be very grid sensitive. This is why descrepancies among the grids are observed in this area.

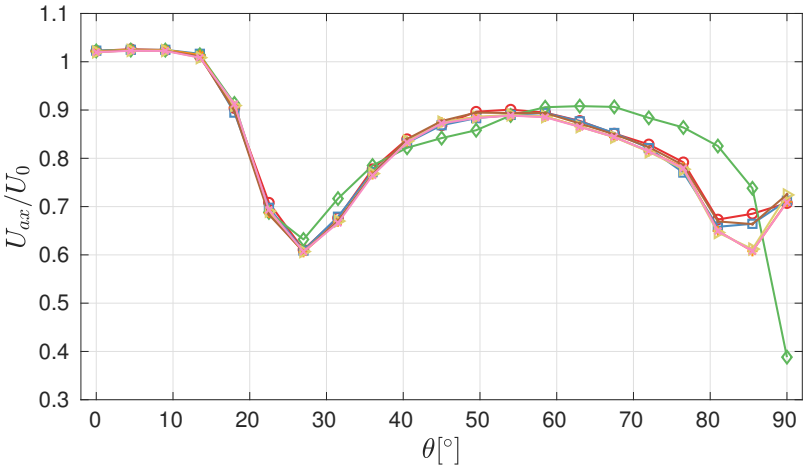

Figure (21): Variation of the time averaged axial velocity component U_{ax}/U_0 along a concentric arc of the curved part whose radius is $14D$, i.e. $1D$ behind the trailing edge of the curved cylinder. (—○—), M01; (—□—), M02; (—◇—), M03; (—✳—), M04; (—▷—), M05; (—■—), M06; (—×—), M07.

Additional 21 probes were placed in the region of $\theta \in [80°, 90°]$ leading to a finer resolution of $\Delta\theta = 0.5°$ compared to a $\Delta\theta = 4.5°$ in figure (21). U_{ax}/U_0 in the finer resolved region is presented in figure (22).

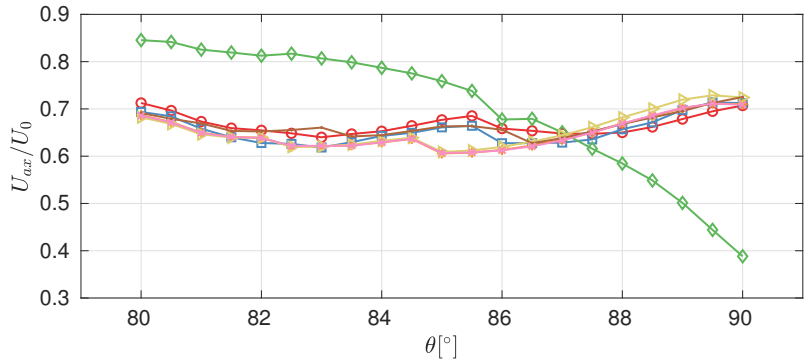

Figure (22): Variation of the time averaged axial velocity component U_{ax}/U_0 along the curved part for all grids. Probes located in $\theta \in [80°, 90°]$. (—○—), M01; (—□—), M02; (—◇—), M03; (—✳—), M04; (—▷—), M05; (—■—), M06; (—×—), M07.

All grids in this intersection region seems to have a small drop in axial velocity around the are region $\theta \approx 84.5° - 86.5°$ though the drop is shifted between the various grids. M05, M07 and M04 follows almost the exact same profile, then a shift to the right is observed for M02 with a slightly higher peak velocity. M01 is shifted further to the right of M02 with an even higher peak. M06 is shifted most to the right but has the same peak value as M02. The coarse M03 keeps a higher overall velocity until $\theta = 87°$ where it drops fast towards $\theta = 90°$ and ends up at a value of U_{ax}/U_0 about 40% lower than the other grids.

Going from M02 to M04, M05 and M07 represent all domain and refinement region enlargements that was made. Going from M02 to M01 represents an increase in surface refinement, and further going from M01 to M06 is a domain and region enlargement. Therefore it seems that the effect of enlarging the domain in the (x, y)-plane is shifting the drop to the left and decreasing the peak. While a surface refinement level produces the opposite effect. It is clear that information in this small intersection region is to some degree lost in M07 compared to M06. Keep in mind that the surface level refinement is closely related to the boundary layer resolution (section (3)).

Figure (23) shows an overview of the axial velocity profiles discussed along the curved part. In the lower bottom plot figure (22) is zoomed in without regard to M03, as to obtain a clearer view of the trends discussed above. In the top plot figure (21) is reused along with close-up views of $\theta \in [0°, 14°]$ and $\theta \in [80°, 90°]$. Observe the starting velocity at $\theta = 0°$ for the various grids. All starting slightly above $U_{ax}/U_0 = 1$ and reads in decreasing order of magnitude: M02, (M01 and M03), M04, M05, M06, M07. Domain enlargements seem to play a major role in this arrangement, which supports the phenomenon of blockage effects as discussed in the beginnning of this section.

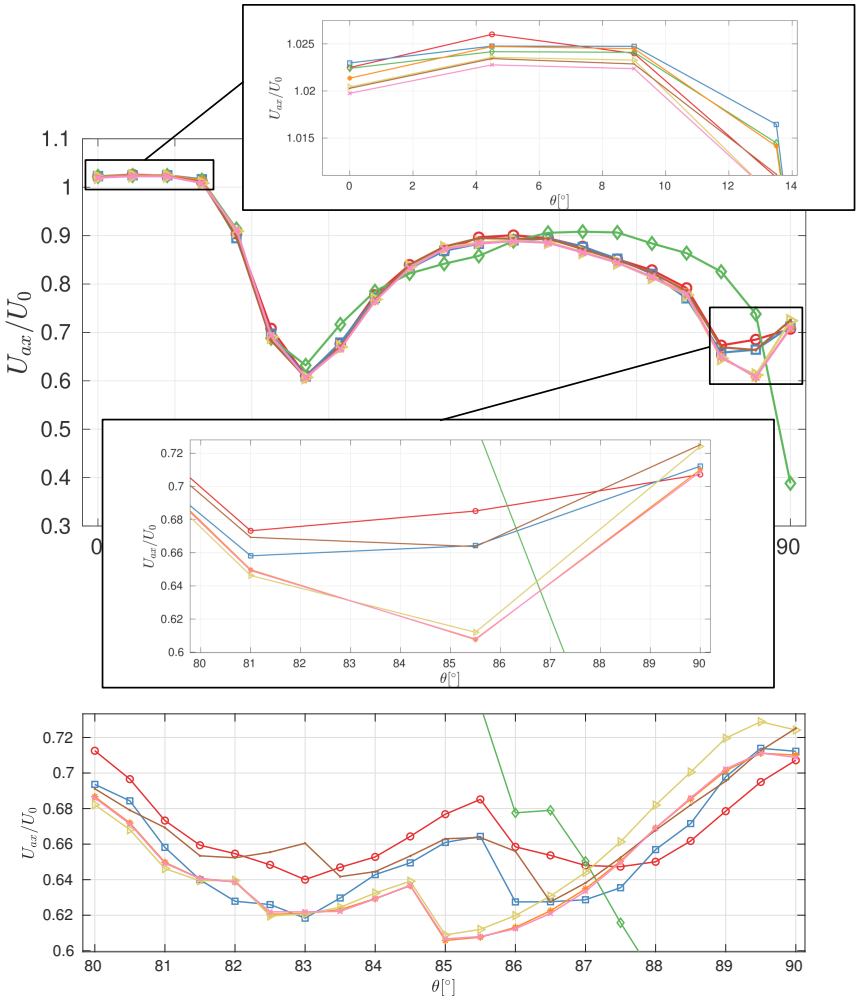

Figure (23): Time averaged axial velocity U_{ax}/U_0 along the curved cylinder with **Top:** close-up views at $\theta \in [0°, 14°]$ as well as $\theta \in [80°, 90°]$. Showing the slight differences between grids. **Bottom:** Close up view of $\theta \in [80°, 90°]$ where a finer distribution of numerical probes were used. (—○—), M01; (—□—), M02; (—◇—), M03; (—✳—), M04; (—▷—), M05; (—■—), M06; (—✕—), M07.

In figure (24) the time averaged U_{ax}/U_0 profile obtained along the span of the vertical extension is presented. An important trend captured only by M07, M01 and M06 is the slight average negative flow occurring in $z/D \approx 2.5 - 4.5$. Only

M01 and M06 tracks the full extent of this region, while M07 turns to $U_{ax}/U_0 = 0$ at $z/D \approx 4.2$. Further M07 turns negative again before reaching the boundary condition of zero vertical velocity at $z/D = 6$.

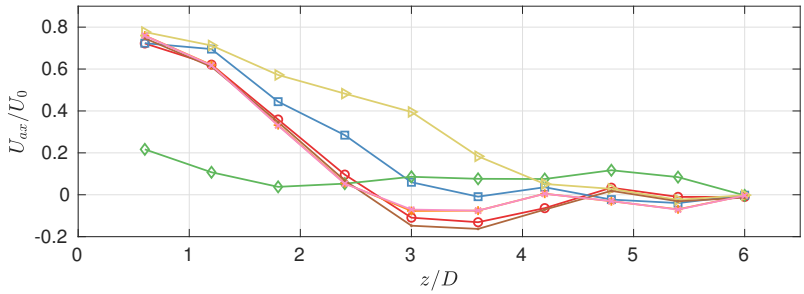

Figure (24): Variation of the time averaged axial velocity component U_{ax}/U_0 along the vertical extension for all grids. Probes are located along a vertical line at $x/D = 14$, i.e. $1D$ downstream of the cylinder trailing edge. (—○—), M01; (—□—), M02; (—◇—), M03; (—✳—), M04; (—▷—), M05; (—■—), M06; (—✕—), M07.

Although there are a few apparent limits to the M07 grid compared to the most refined M06, the computational efforts demanded by M06 compared to M07 is considered too costly in the present study. It seems reasonable to believe that the M07 type setup will be more than adequate for establishing a numerical basis for the curved cylinder problem in OpenFOAM at this stage. This grid study is however important to know in which aspects the current grid might give poorer results.

4.3 Effect of Time Step

As the semi-implicit Crank-Nicolson scheme used is rather robust with respect to larger time steps, it is tempting to use as large time step as possible to save computational time. Although the solver can handle larger time steps without diverging, the order of accuracy of the solution might be degraded.

Schemes with the weighting parameter $1/2 \leq \Psi \leq 1$ are said to be unconditionally stable for all values of the time step (Fletcher 1991). However it is more important to ensure that all coefficients are positive for physically realistic and bounded results (Versteeg 2007). By investigating the scalar conservation law for unsteady convection-diffusion the positive coefficient criterion was found to be according to equation (47) for one-dimensional flow in x-direction (Versteeg 2007).

$$\Delta t < \frac{\rho_{sim}(\Delta x)^2}{\nu} \tag{47}$$

Where $\rho_{sim} = 1$ is used as the flow Re is defined in this study by specifying kinematic viscosity and inflow velocity.

Equation (47) sets an upper limit on the time step Δt, where ρ is the fluid mass density, ν is the fluid kinematic viscosity and Δx is the grid cell size. For a grid of $CylRefLvl = 4$ and $CylRefLvl = 5$ it is obtained a positive coefficient criterion for the time step of $\Delta t^* < 0.098 U_0/D$ and $\Delta t^* < 0.024 U_0/D$ respectively.

As stated in the beginning of section (4.2) simulations were run for $100 U_0/D$ dimensionless time units before gathering data for statistics. In this first interval an automatic regulation of time step was used. A maximum Courant number was specified in OpenFOAM to never exceed $Co_{max} = 5$, and time step was adjusted accordingly. This allowed to get an estimation of a constant time step for the second simulation interval. Data was still sampled each 0.05 time steps in all simulations. A constant time step is essential for statistics, especially as the discrete Fourier transform is very sensitive to irregularities in sampling period.

In this section the simulation M07 is compared to a simulation C04 utilizing the same grid. C04 however utilizes a time step set so that a $Co_{max} = 0.79$ is

never exceeded in the domain. A mean Courant number of $Co_{mean} = 0.014$ was preserved. In comparison M07 ran on a time step which ensured a $Co_{max} = 3.86$ and $Co_{mean} = 0.07$. The computational time required for a full $1000U_0/D$ simulation is about 200 hours and 45 hours for C04 and M07 respectively.

The resulting time averaged spanwise flow profiles are given in figure (25).

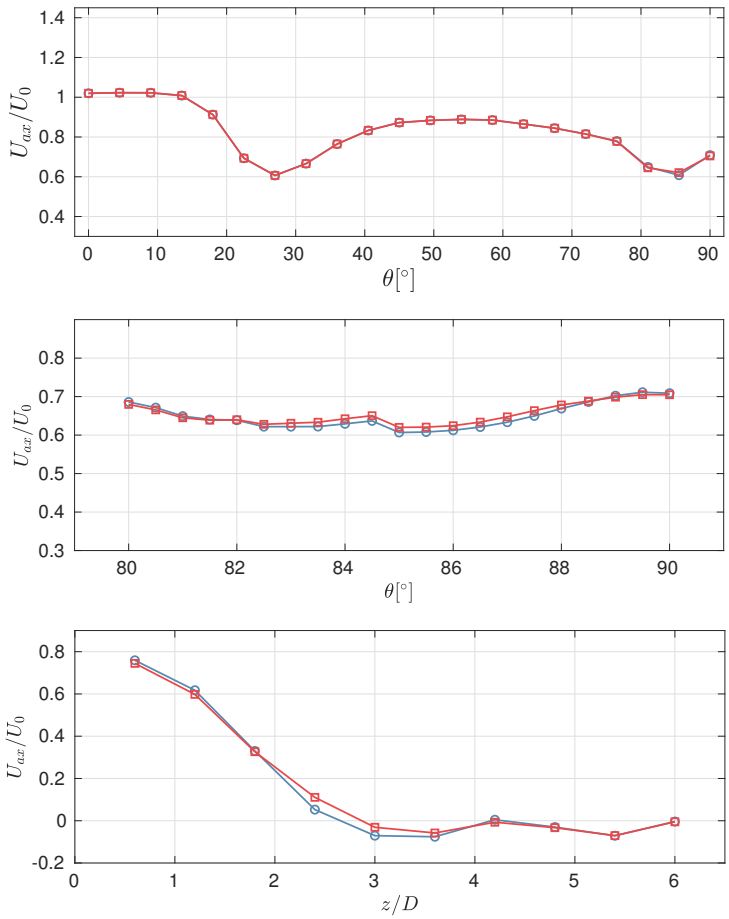

Figure (25): Variation of the time average of the axial velocity component U_{ax}/U_0 for two cases, illustrating the effect of time step on the solution. (—○—), M07; (—□—), C04. **Top:** Along the curved part. **Middle:** Close up view of $\theta \in [80°, 90°]$ where a finer distribution of numerical probes was used. **Bottom:** Along the vertical extension.

It can be seen that there actually are some slight differences in the obtained profiles, and the deviations are found in the same locations that separated the different grids in the M-series. Comparing quantitative data of the two cases we can see in table (7) that some of the trends observed for the grid and domain study persist. Frequency and drag is reduced, while the RMS of the lift has increased when refining the time step.

Table (7): Force coefficient statistics and lift force frequency for M07 and C04. $C_{L,rms}$ is the root-mean-square of the oscillating lift-force coefficient, $\overline{C_D}$ is the time averaged drag coefficient and f^*_{peak} is the dominating frequency of oscillation for the lift-force.

Case	$C_{L,rms}$	$\overline{C_D}$	f^*_{peak}
M07	0.0386	0.8672	0.1214
C04	0.0391	0.8646	0.1236

The results are still very close, and the increase in computational effort required is rather large. Thus it is considered in the present study that a M07 type grid and domain setup utilizing a larger time step is sufficient. However a lot has been learned about the effects of the simulation setup on the quality of the solution.

4.4 General Thoughts On This Chapter

- A more focused grid study might be performed especially with respect to the quality of the boundary layer mesh. (See section 3.3 for thoughts on layer mesh.)
- A targeted grid study utilizing similar parameters as in the present study might be beneficial. As can be seen in section 5, the velocity field and overall wake dynamics of the present study seems to agree with DNS simulations, however integrated forces are somewhat off. A grid study with a base in the M07-type grid could be performed with the aim of obtaining a better boundary layer mesh setup and investigating the effect on integrated force coefficients.

5 Simulations - DNS Comparisons

After establishing a numerical setup through grid generation and grid independence testing, it is of interest to establish a common ground with DNS data. The process in this section is that of verifying the simulation setup, i.e. establish to what degree the "equations are solved right" (Roache 1998) by verification with unpublished DNS data (F. Jiang, B. Pettersen, H. I. Andersson, et al. 2018).

It is important to know what the present OpenFOAM setup does right and what are its shortcomings so that a continuation of the work in this thesis have a starting point. In addition, the effect of shear inflow is discussed later in section (6), of which there are no previously published results in the literature (at least to the knowledge of the author). This section then establishes a basis for comparison in later sections.

Comparisons are made with respect to near wake flow dynamics. Aspects of comparison include: the overall wake vortical structures obtained by λ_2 (Jeong and Hussain 1995); profiles of time averaged axial flow along the cylinder span and frequency components in the wake; as well as integrated forces on the cylinder.

5.1 Problem Description

The flow configuration follows that of the DNS study (F. Jiang, B. Pettersen, H. I. Andersson, et al. 2018) and in accordance with the numerical issues discussed in (4). The configuration is summarized in figure (26) and noticable properties are $L_h/D = 10$, $L_v/D = 24$ and the standard radius of curvature $R/D = 12.5$. The grid properties are directly derived from the M07-grid obtained in section (4) only extending the vertical extension. The uniform inflow condition U_0 is imposed in the positive x-direction.

Parameter	
Configuration	Concave
L_h	$10D$
R	$12.5D$
L_v	$24D$
Inflow (C01)	Uniform $Re = 200$
Inflow (C02)	Uniform $Re = 500$

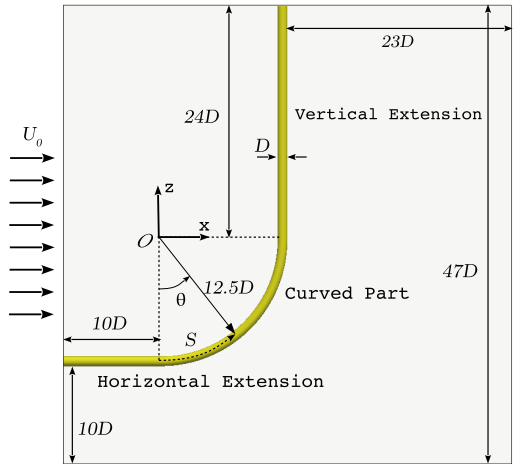

Figure (26): The configuration used for verification with DNS results. This setup is utilized for a $Re = 200$ (C01) and a $Re = 500$ (C02) flow. The configuration is derived from the M07 grid (see section 4.2) only changing to a $24D$ vertical extension.

Two cases are studied and compared, that is one with $Re = 200$ and one with $Re = 500$ which are named C01 and C02 respectively. For reference the DNS results are named accordingly FC01 and FC02 for the two Re respectively.

In the present study all simulations were run $t^* = 100U_0/D$ dimensionless time units to ensure a developed flow, then data were gathered for $1000U_0/D$ time units. The instantaneous snapshots were then extracted from the last time instant $t^* = 1100U_0/D$.

5.2 Near Wake Velocity Analysis - RE200

The time averaged flow along the cylinder span is presented in figure (27) and (28) for both the present study and the DNS data. The normalized axial flow velocity component U_{ax}/U_0 is calculated as equation (48) and then time averaged.

$$\frac{U_{ax}}{U_0} = \frac{u}{U_0}\cos(\theta) + \frac{w}{U_0}\sin(\theta) \tag{48}$$

It is measured along a concentric arc of the curved part, which radius is $13.6D$, i.e. at $0.6D$ behind the trailing edge of the curved cylinder. In a similar manner along the vertical extension, measurements are taken along a vertical line at $x/D = 13.6$. Everything in the centre plane $y/D = 0$.

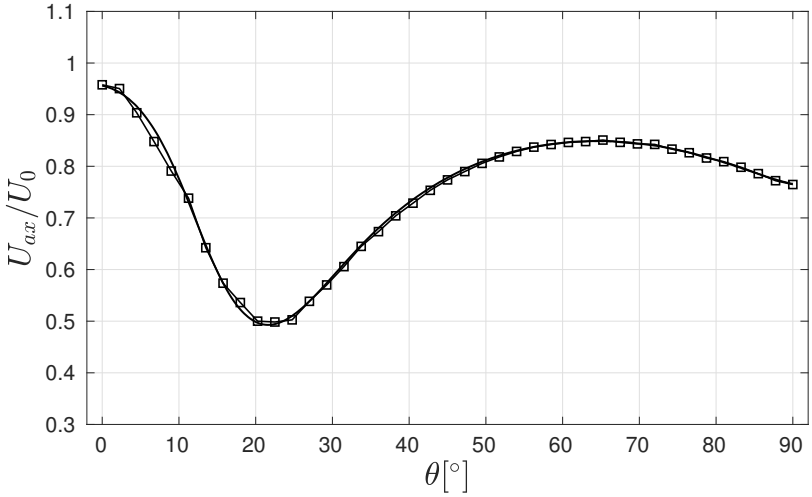

Figure (27): Variation of the time average of the axial velocity component U_{ax}/U_0 along a concentric arc of the curved part which radius is $13.6D$, i.e. $0.6D$ behind the trailing edge of the curved cylinder. Showing the present study (⊟) compared to DNS data (—) (F. Jiang, B. Pettersen, H. I. Andersson, et al. 2018). $Re = 200$.

The time averaged axial flow seems to follow the DNS solution quite well for $Re = 200$. In figure (27) we see that the end-points of the graph are visually

exactly the same for both solutions, beginnning at $U_{ax}/U_0 \approx 0.95$ for $\theta = 0°$ and ending at $U_{ax}/U_0 \approx 0.77$ for $\theta = 90°$. $U_{ax}/U_0 < 1$ indicating that the probe is inside the boundary layer at the intersection between the horizontal extension and the curved part. This is in good agreement with the boundary layer study on the horizontal extension by (F. Jiang, B. Pettersen, and H. I. Andersson 2018) for $Re = 100$, where u/U_0 was ~ 0.85 at $\delta h/D = 0.6$ from the cylinder surface.

Some deviations from the DNS can be observed where large gradients occur. Examples in figure (27) are the sudden drop at $\theta \approx 5°$ towards the graph minimum at $\theta \approx 20°$ where the graph then again increases.

Similar discrepancies are found along the vertical extension in figure (28) just around the beginning of a steady drop of U_{ax}/U_0 at $z/D \approx 8$. Near the top boundary around $z/D = 21 - 24$ a the axial flow persists further up than in the DNS solution. The axial velocity deviates from the DNS line at $z/D \approx 21$ and is almost constant until a sudden drop begins at $z/D \approx 23$ towards the boundary at $z/D = 24$. The DNS solution has a more steady decrease from $z/D = 7$ towards the boundary. This is further discussed in section (5.4).

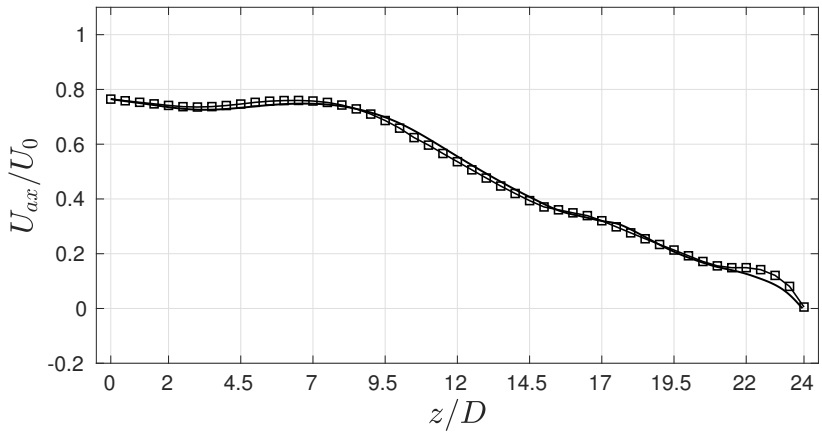

Figure (28): Variation of the time average of the axial velocity component U_{ax}/U_0 along the span of the vertical extension at $x/D = 13.6$, i.e. $0.6D$ behind the trailing edge of the vertical cylinder. Showing the present study (-□-) compared to DNS data (——) (F. Jiang, B. Pettersen, H. I. Andersson, et al. 2018).

5.3 Forces and Frequency Analysis - RE200

The force coefficients C_L and C_D of lift and drag respectively was logged separately on the three cylinder parts. In table (8) the root-mean-square of the lift coefficient $C_{L,rms}$ and the time averaged drag coefficient $\overline{C_D}$ is presented for the curved part, horizontal extension, the vertical extension and the configuration in total. All individual cylinder parts are normalized on the same projected area $A_{ref} = 37D^2$ corresponding to the projected area of the complete configuration. The total value is calculated from statistics performed on the sum of the force coefficient time series of the individual parts, such that phase differences between forces on each part is accounted for. This is in accordance with the total configuration being assumed completely rigid.

The corresponding values obtained from the DNS study (F. Jiang, B. Pettersen, H. I. Andersson, et al. 2018) are also provided in table (8) and the percentage difference between the studies are given as $|\Delta|$. Further the normalized frequency $f^*_{peak} = f_{peak}D/U_0$ represents the dominating frequency occuring in the oscillating signal of C_L, obtained by a discrete Fourier transform of the time series.

Table (8): The root-mean-square of the lift coefficient $C_{L,rms}$, the mean drag coefficient $\overline{C_D}$, and the dominating frequency of the lift force $f^*_{peak} = f_{peak}D/U_0$ given for the individual cylinder parts, total configuration and comparison values from DNS study. $|\Delta|$ is the percentage difference between the two studies. $Re = 200$.

	Curve	Horizontal	Vertical	Total	Total DNS	$\lvert\Delta\rvert$ %
$C_{L,rms}$	0.0003	0.0000	0.0215	0.0216	0.0179	20.7
$\overline{C_D}$	0.3094	0.0454	0.7201	1.0749	0.9816	9.5
f^*_{peak}	0.1220	0.1680	0.1680	0.1680	–	–

The $C_{L,rms}$ and $\overline{C_D}$ is clearly larger in the present study compared to the DNS results, with roughly an increase of $\sim 20\%$ and $\sim 10\%$ in lift and drag respectively from DNS to the present study results. This is a possible consequence of grid resolution as it was also observed as a general trend in section (4) that the magnitude of the forces increase as the grid near the cylinder and in the boundary layer especially is refined.

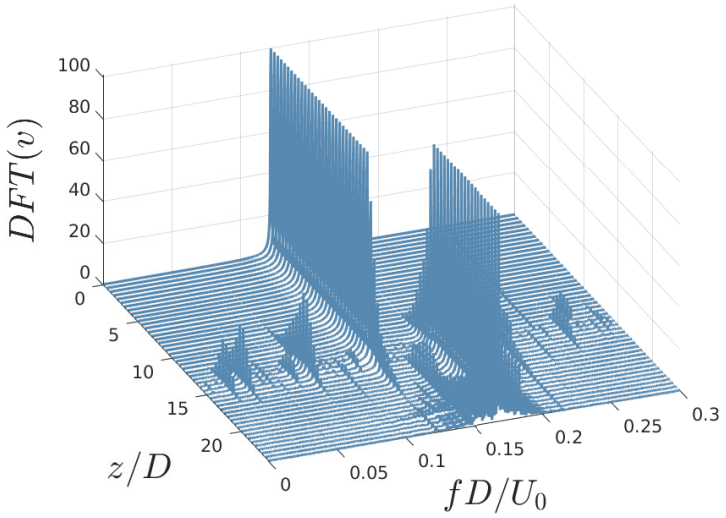

Figure (29): Frequency spectrum of frequencies present in the time series of v measured along a vertical line at $x/D = 16$ behind the vertical extension, i.e. $3D$ behind the trailing edge of the cylinder. $DFT(v)$ indicates the spectrum value in % of the largest peak present; z/D is the vertical position; fD/U_0 is the normalized frequency. $Re = 200$.

Figure (29) indicates the frequency spectrum obtained by a discrete Fourier transform of time series of v measured along a vertical line at $x/D = 16$ behind the vertical extension, i.e. $3D$ behind the trailing edge of the cylinder. The $DFT(v)$ indicates the values in percent of the largest peak present in the plot, z/D indicates vertical position and $f^* = fD/U_0$ is the normalized frequency of oscillation in v. There are predominantly two peak frequencies present in the wake, and these are related to the shedding frequency in two cells along the span. The frequency $f^* = 0.122$ dominates in the range of $z/D = [0, 14.5]$ while in the upper part of $z/D = [14.5, 24]$ the frequency is $f^* = 0.168$. Between those two frequencies there is a gradual overlap of frequency peaks in the spectrum. The DNS study (F. Jiang, B. Pettersen, H. I. Andersson, et al. 2018) reports two similar cells of frequency $f^* = 0.126$ and $f^* = 0.172$. The shedding frequencies are then somewhat lower in the present study. This agrees with figure (28) in which a slightly higher axial velocity is observed clsoe to the top boundary in the present

study. The onset of the cell of higher frequency is reported in the DNS study at $z/D \approx 15$. These cells are from here on referred to as normal shedding regimes for the concave flow configuration, after (F. Jiang, B. Pettersen, H. I. Andersson, et al. 2018). The definitions are as indicated in figure (30) where iso-surfaces of constant λ_2 (Jeong and Hussain 1995) are used for visuals of the regimes. The vortex topology is further discussed in the next section. The *regime 1* is included as the regime where there is no vortex shedding. The comparison of shedding frequencies is summarized in table (9).

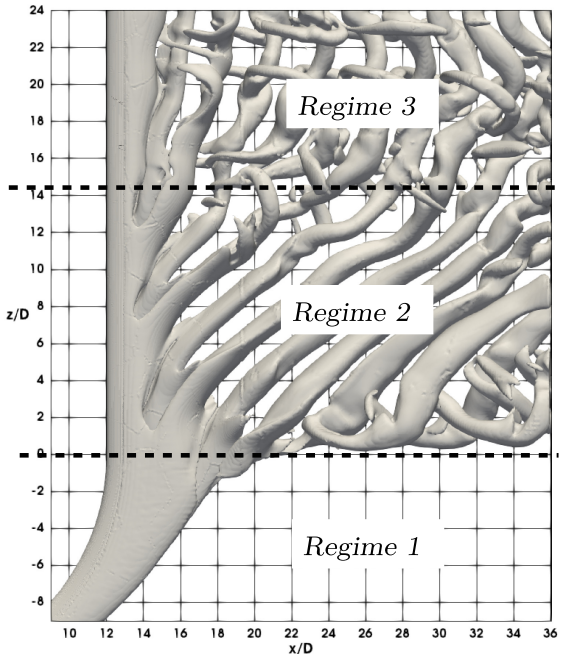

Figure (30): Iso-surfaces of $\lambda_2 = -0.1$ (Jeong and Hussain 1995) for the uniform flow at $Re = 200$ with dashed lines indicating shedding regimes.

Table (9): Summary of the comparison of shedding frequencies in regime 2 and 3 for the present study and the DNS solution.

$f^* = fD/U_0$	Present study	DNS
f^* Regime 2	0.122	0.126
f^* Regime 3	0.168	0.172
Onset of regime 3	$z/D \approx 14.5$	$z/D \approx 15$

5.4 Overall Near Wake Structure - RE200

In the case of uniform flow past the concave cylinder configuration at $Re = 200$, the wake is still characterized by a large laminar non-shedding region around the curved part. Figure (31) shows a direct comparison of instantaneous wake vortical structures using iso-surfaces of constant λ_2. The figure shows the present study to the left and the DNS results to the right. The visualization of the two are cut off at different x/D, however a dashed vertical line is added for reference at $x/D = 30$.

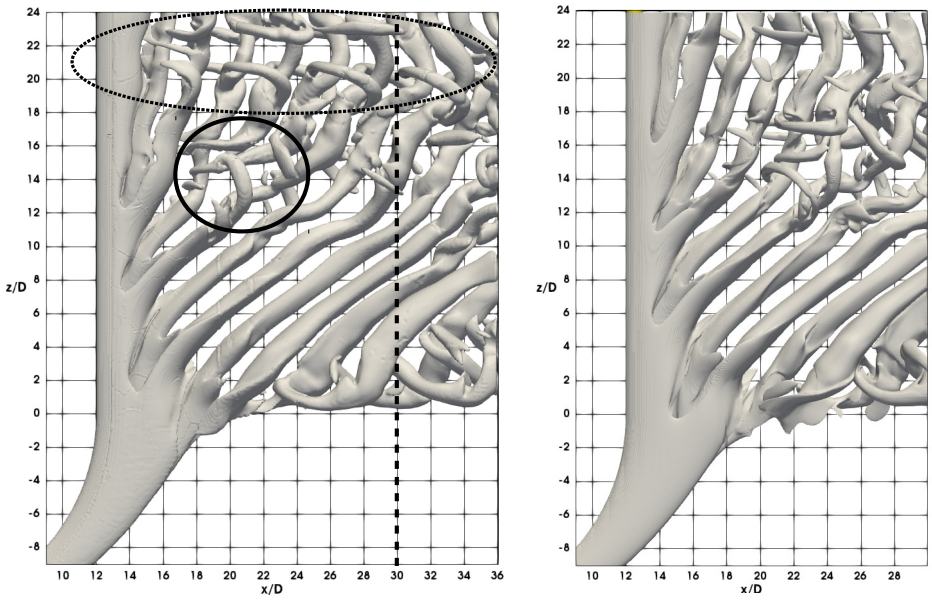

Figure (31): Wake vortical structures indicated by iso-surfaces of λ_2 for $Re = 200$. The flow is viewed in the positive y-direction. View direction is further clarified by the grid in the (x, z) plane. **Left:** Iso-surface of $\lambda_2 = -0.1$ as a result of the present study. Dashed line indicating downstream point where the DNS plot ends. **Right:** Iso-surface of $\lambda_2 = -0.01$ from unpublished DNS data (F. Jiang, B. Pettersen, H. I. Andersson, et al. 2018).

One immediate observation is that the two snapshots are taken at two different time instants, with the right plot being slightly "ahead" of the left in time. However this is of minor importance for comparison and the flow structures are

clear. On the left plot in figure (31) a vortex dislocation is indicated by a solid black circle which also can be found in the DNS plot (although not marked). A vortex dislocation occurs at the intersection between different shedding regimes as a "bridging" between two shedding frequencies (C. H. K. Williamson 1989). By looking at $z/D = 14$ in both plots in figure (31) one can see the left end of a small vorticity core related to this bridging. In the left plot it occurs slightly upstream of $x/D = 20$. In the right plot the same vortex core is observed slightly downstream of $x/D = 20$. One can observe that this bridging involves redistribution of vertical vorticity (ω_z) to both streamwise (ω_x) and cross-stream vorticity (ω_y). By visual inspection it is observed that the vortex dislocation links four vortex cores in the upper domain to two vortex cores below the dislocation. This is a result of the apparent high frequency shedding above $z/D = 14$ and the lower shedding frequency below $z/D = 14$.

The left plot lacks some details in the smallest scales of the flow when compared to the right (DNS) plot. This is clear e.g. in the mentioned vortex core at the dislocation, which results in the visualization of the vortex being broken up in two parts and is a fault of the relatively low grid resolution in the present study compared to the DNS study.

Another point of figure (31) which calls for attention is the region marked in a dashed oval. This is along the top boundary of the domain and the same pattern is not present in the DNS solution. Rather strong streamwise vorticity cores are observed even though the dominant flow is that of vortex shedding of ω_z. The pattern seems to be produced in a regular manner along the top part and is clearly a result of three-dimensional spanwise instability. Examples of three-dimensional instabilities in the wake of straight circular cylinders are given in the famous review by (C. Williamson 1996) or the recent DNS study of (H. Jiang et al. 2016) on 3D wake transitions. Especially the "mode A" instability which onsets at around $Re = 190$ (C. Williamson 1996) bears a strong resemblence to the streamwise vortex pairs observed in figure (31).

The "mode A" structure occurs even for straight cylinders with uniform inflow, however in the case of the concave curved configuration it is known that also a strong axial flow is present (section 5.2). In section (5.2) figure (28) shows

that the time averaged U_{ax}/U_0 deviates from the DNS in the upper $\sim 3D$ of the domain, and is actually stronger compared to the DNS. The measured frequencies in the wake found in section (5.3) was lower than what the DNS study reported, which supports the idea of an influence from spanwise flow.

The distribution of instantaneous vertical velocity component w in the centre plane is plotted and compared for the two studies in figure (32). There is a slight oscillation of w from negative to positive values happening in the region $z/D = [21, 24]$ in the left plot which is not present in a same manner in the DNS results (right plot).

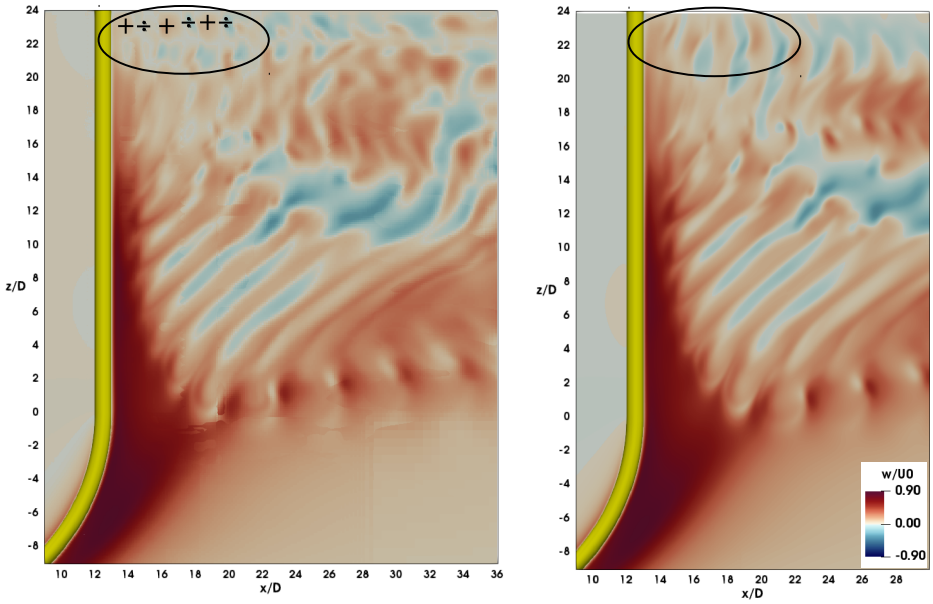

Figure (32): Instantaneous distribution of w in the $y/D = 0$ centre plane. **Left:** Result of the present study. Mild oscillation of w is indicated by a black oval in the top domain. Regions of positive and negative values are marked with plus and minus signs. **Right:** Result of the DNS study (F. Jiang, B. Pettersen, H. I. Andersson, et al. 2018). The upper region of comparison is marked by an oval.

This mild oscillation of w might be enough to trigger the 3D instability in the upper region. It seems reasonable to believe that the oscillation occurs as a result of the upper boundary condition in combination with a slightly stronger

spanwise flow. The differences in axial flow between the two studies might owe to grid effects, as a similar behaviour was observed in the poorly resolved M03 grid in the grid study (section (4)) compared to the finer grids. The time averaged axial flow along the vertical section was heavily overpredicted by the poor grid.

The phenomenon in figure (31) looks similar to flow topology for cases where the spanwise flow interferes with the slip-wall boundary (e.g. (Miliou et al. 2007)). In the DNS investigation (F. Jiang, B. Pettersen, H. I. Andersson, et al. 2018) the effect of various lengths of L_v is studied and a similar behaviour can be seen for $L_v/D = 6$ along the top boundary, however not in the exact same manner as in the present analysis.

5.5 Overall Near Wake Dynamics - RE500

At $Re = 500$ massive three-dimensional instabilities can be observed in the wake with "mode B"-like streamwise vorticity structures (C. Williamson 1996) forming along the complete span of the vertical extension as well as in the upper $\sim 4D$ of the curved part. The wake becomes then more complex than in the $Re = 200$ case, and the wake is filled with fine vortical structures. This can easily become a problem for the OpenFOAM setup used, compared to the DNS, as the grid cells are not nearly as small as what is needed to catch the finest structures present in the flow. The smallest scales present in a flow is related to the Kolmogorov microscales (Tennekes 1972) and a DNS approach is required to come close to resolving these structures (White 2006).

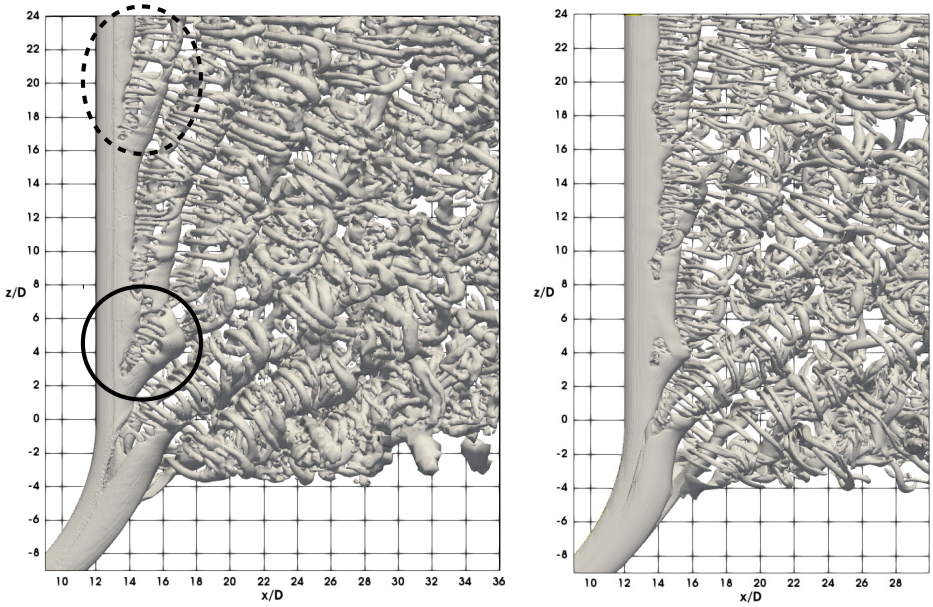

Figure (33): Wake vortical structures indicated by iso-surfaces of λ_2 for $Re = 500$. The flow is viewed in the positive y-direction. View direction is further clarified by the grid in the (x, z) plane. **Left:** Iso-surface of $\lambda_2 = -1.0$ as a result of the present study. Dashed oval indicates that more oblique vortices are shed at the top. Black circle marks a boundary between two distinct shedding frequencies. **Right:** Iso-surface of $\lambda_2 = -0.1$ from unpublished DNS data (F. Jiang, B. Pettersen, H. I. Andersson, et al. 2018).

In figure (33) the fine-scaled structures are very much visible and clear in the DNS plot to the right. Although the present study to the left is able to catch the large scale motions of the wake and some smaller scale motions close to the cylinder, the grid further downstream is clearly contributing to a dissipation of the finer scale motions. Notice that two very different magnitudes of λ_2 is used in the two plots. The OpenFOAM solution requires a plot of "stronger" $\lambda_2 = -1.0$ compared to $\Lambda_2 = -0.1$ for the DNS to display the similar structures properly.

It is noticable in figure (33) that the OpenFOAM solution exhibits a seemingly more oblique shedding than the DNS near the top boundary. This is indicated by a black dashed oval. A black solid line circle indicates a distinct boundary between two shedding frequencies occurring at $z/D = 4$, which matches well with the DNS result.

The frequency distribution along the vertical extension in the DNS study is reported as one dominant shedding regime in the lower part of the vertical extension at a frequency of $f^* = 0.127$. Above this frequency there is a continous frequency band of increasing frequency with increasing z/D until reaching a dominant frequency in the straight shedding in the upper part (F. Jiang, B. Pettersen, H. I. Andersson, et al. 2018). The regimes and wake topology can be seen in figure (34). The limits of this frequency band is visualized in figure (35) as two straight lines along with the peak frequencies of v obtained in the wake of the OpenFOAM simulation. The lower frequency regime is captured with a frequency of $f^* = 0.121$ compared to $f^* = 0.127$ in the DNS. Both studies extract the frequencies at $3D$ behind the trailing edge of the vertical extension, in the centre plane $y/D = 0$.

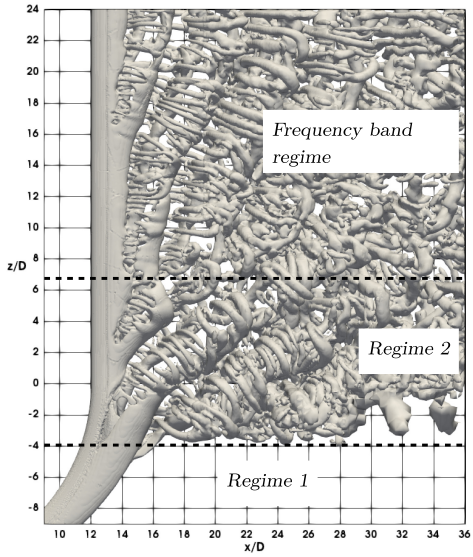

Figure (34): Iso-surfaces of $\lambda_2 = -1$ (Jeong and Hussain 1995) for the uniform flow at $Re = 500$ with dashed lines indicating shedding regimes.

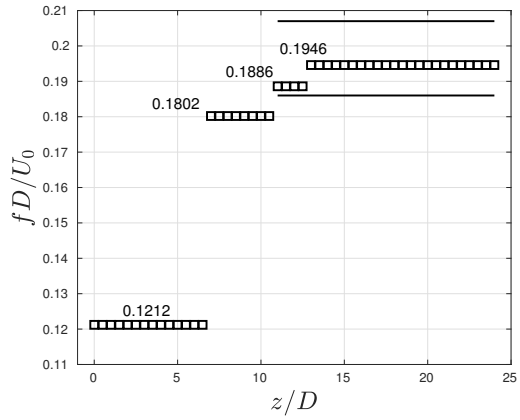

Figure (35): Distribution of peak frequencies of v in the wake along a vertical line $3D$ behind the vertical extension. (□), $f^* = fD/U_0$ present study; (—), ends of frequency band in DNS study at $f^* = 0.186$ and $f^* = 0.207$ (F. Jiang, B. Pettersen, H. I. Andersson, et al. 2018).

The OpenFOAM solution obtains once again reasonable dominant frequencies however the exact extent of the frequency band and how well it is represented has not been analysed quantitatively. Figure (36) however shows a qualitative estimation of the ends of the frequency band captured in the present study.

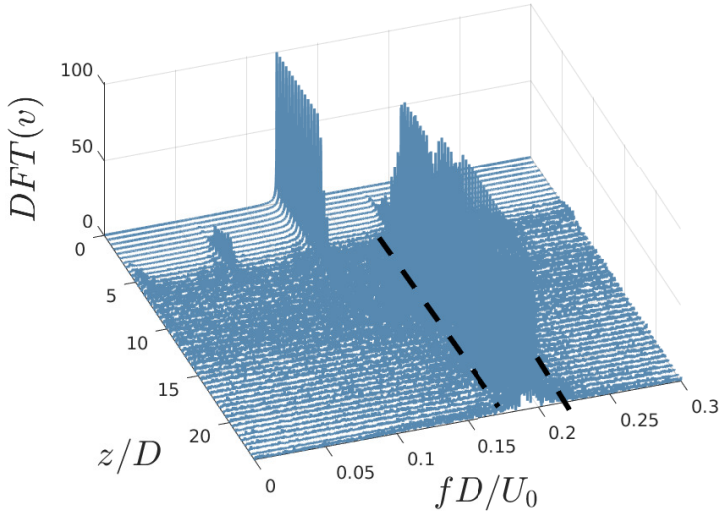

Figure (36): Frequency spectrum of frequencies present in the time series of v measured along a vertical line at $x/D = 16$ behind the vertical extension, i.e. $3D$ behind the trailing edge of the cylinder. $DFT(v)$ indicates the spectrum value in % of the largest peak present; z/D is the vertical position; fD/U_0 is the normalized frequency. (- - -), approximate width of the frequency band. $Re = 500$.

The time averaged profiles of U_{ax}/U_0 along the curved part at $Re = 500$ is presented in figure (37) and along the vertical extension in figure (38).

The curves in both studies show the same main trends in the curved part, however larger discrepancies are observed at large curvatures in the profile compared to the comparison on $Re = 200$. Both profiles begin at $U_{ax}/U_0 \approx 1.02$, which means the probes are outside the boundary layer at the intersection between the curved part and the horizontal extension. The slight large value is likely due to blockage effects (F. Jiang, B. Pettersen, H. I. Andersson, et al. 2018). As in the $Re = 200$ case the OpenFOAM solution drops sooner than the DNS in the region $\theta =$

$0 - 10°$. Otherwise the curves align well until the OpenFOAM solution deviates somewhat from $\theta \approx 75°$. The general trend seems to be preserved, however the first trough ($\sim 82°$) and the following peak ($\sim 85°$) are underpredicted and shifted to the right. The last trough at $\theta \approx 88°$ is also underpredicted, but the two graph endpoints (at curve-vertical intersection) are coinciding.

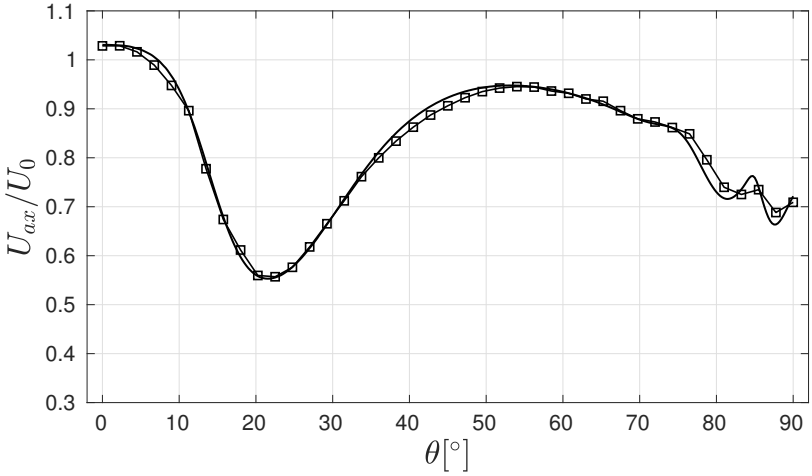

Figure (37): Variation of the time averaged axial velocity component U_{ax}/U_0 along a concentric arc of the curved part whose radius is $13.6D$, i.e. $0.6D$ behind the trailing edge of the curved cylinder. (⊟), present study; (—), DNS data (F. Jiang, B. Pettersen, H. I. Andersson, et al. 2018). $Re = 500$.

The axial flow along the vertical extension (38) shows some significant deviations from the DNS study. First the maximum at $z/D = 2$ and the details in graph curvature in this area is lost. Afterwards the OpenFOAM solution drops more sudden than the DNS at $z/D \approx 4$. Even though the main trends are captured along the span, small details are lost, and the present solution shows a constant axial flow in $z/D = 13 - 21.5$ while the DNS solution is more steadily decreasing. Similar to the $Re = 200$ case, this leads to the OpenFOAM solution dropping more rapidly towards the boundary condition.

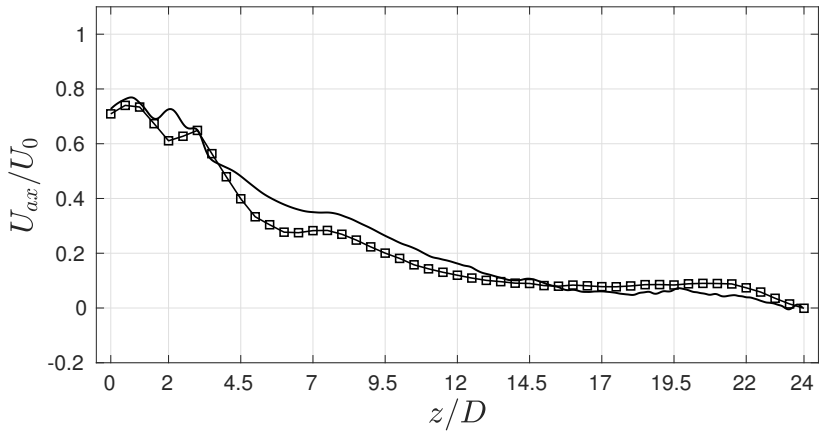

Figure (38): Variation of the time averaged axial velocity component U_{ax}/U_0 along the span of the vertical extension at $x/D = 13.6$, i.e. $0.6D$ behind the trailing edge of the vertical cylinder. (-□-), present study; (——), DNS data (F. Jiang, B. Pettersen, H. I. Andersson, et al. 2018). $Re = 500$.

The region starting at $\theta \approx 75°$ in the curved part and up to $z/D \approx 2.5$ in the vertical part is a transitional area where the dynamics are significantly different from both the lower and upper domain (F. Jiang, B. Pettersen, H. I. Andersson, et al. 2018). The wake is very unstable in this region, and it seems to be the most challenging part for the OpenFOAM study to capture.

5.6 Forces and Frequency Analysis - RE500

Regarding the logging and calculation of forces, the same approach and definitions are as given for the $Re = 200$ case. The result and comparison values from the DNS study is given in table (10).

Table (10): The root-mean-square of the lift coefficient $C_{L,rms}$, the mean drag coefficient $\overline{C_D}$, and the dominating frequency of the lift force $f^*_{peak} = f_{peak}D/U_0$ given for the individual cylinder parts, total configuration and comparison values from DNS study. $|\Delta|$ is the percentage difference between the two studies. $Re = 500$.

	Curve	Horizontal	Vertical	Total	Total DNS	$\lvert\Delta\rvert$ %
$C_{L,rms}$	0.0266	0.0000	0.0593	0.0640	0.0329	95
$\overline{C_D}$	0.2770	0.0247	0.7060	1.0076	0.9052	11.3
f^*_{peak}	0.1212	0.1212	0.1946	0.1946	–	–

Even larger errors are observed in the $Re = 500$ case compared to $Re = 200$. Now there is approximately a doubling of the $C_{L,rms}$ in the OpenFOAM solution compared to DNS. The $\overline{C_D}$ shows only a slightly increased error which is now just above $\sim 11\%$.

Blank Page

6 Simulations - The Effect of Shear Inflow

Three-dimensionalities in the wake of flow past bluff bodies are enhanced by the introduction of *non-uniform geometry*. This has been seen in previous studies of inclined cylinders where a yaw angle of the cylinder introduces slanted vortex shedding (see e.g. extensive investigation (Ramberg 1983) of yaw and finite length, or as early as (Hanson 1966)). The flow past tapered cylinders at low Reynolds numbers studied by (Gaster 1969) showed a local Reynolds number effect on the wake structure in the form of different shedding frequencies along the span as the cylinder diameter changes. Curved cylinders in the recent years studied by e.g. (Miliou et al. 2007), (Canabes 2010), (Xu and Cater 2016) and section (5) of the present study indicate complex three-dimensional flow features.

For the cylinder, the three-dimensionality of the large scale wake dynamics often involves oblique vortex shedding and the appearance of vortex shedding in cells along the cylinder span. However the introduction of *non-uniform inflow conditions* poses yet another trigger for three-dimensional effects. As seen recently by (Xu and Cater 2016) studying both uniform and logarithmic inflow on straight and curved cylinder configurations at large Reynolds numbers, (Canabes 2010) investigating shear flow in curved convex configuration and (Parnaudeau et al. 2007) studying the effect of shear flow on straight circular cylinders as well as tapered cylinders.

When shear is present in the spanwise direction of a straight cylinder, the vortex shedding takes place in spanwise cells with a constant frequency over each cell (Sumer 2006). In the review by (Griffin 1985) research show that the length of the shedding cells decrease with increased shear rate.

(Maull and Young 1973) studied the effect of shear inflow on a bluff body of length $19D$ with an oval leading edge and an extended body, and the spanwise distribution of Strouhal frequencies $f_c^* = fD/U_c$ in the wake were presented as in figure (39) as four spanwise cells. The cellular shedding frequencies was found to increase with increasing spanwise location z/D and in turn local Reynolds number $Re_l = U_0(z)D/\nu$. When the strouhal frequency was based on the local velocity along the span, the cells grouped along a frequency of $f_l^* = fD/U_0(z) \approx 0.25$.

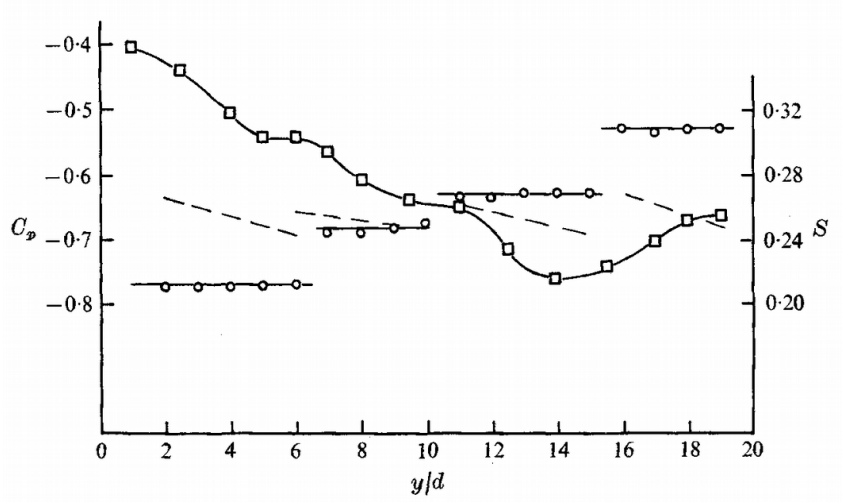

Figure (39): Distribution of Strouhal frequency f^* (figure: S) in the wake of a bluff body in uniform spanwise shear at $Re = 2.8 \cdot 10^4$, shear steepness $K = 0.025$. Taken from (Maull and Young 1973). (—○—), $f_c^* = fD/U_c$ based on median reference velocity; (- - -), $f_l^* = fD/U_0(z)$ based on local inflow velocity; (—□—), base pressure coefficient C_{pb} (figure: C_p) based on median velocity. Spanwise coordinate in figure y/d, where d is the body diameter.

(Zdravkovich 1997) reviews the main flow dynamics present in a shear flow past a circular cylinder. Two secondary flows are present along the cylinder span. A spanwise pressure gradient is established along both the leading and trailing edge. The local stagnation pressure is proportional to the local inflow velocity squared, i.e. a pressure coefficient of $C_p(z) \propto \pm U_0(z)^2$, the sign depending on which side of the cylinder is evaluated. On the leading edge side a secondary spanwise flow is driven by the pressure gradient from the high velocity end to the low velocity end. On the trailing edge side the pressure gradient is negative, such that the same phenomenon is produced, except flow runs from the low to high velocity end. The secondary flow is visualized in figure (40) for both positive and negative shear rate.

The secondary flows along the span will be referred to as *upwash* and *downwash* in this section, with flow direction corresponding to positive and negative z-direction respectively.

Further (Zdravkovich 1997) points out as the vorticity created in the free stream approaches the cylinder, the vortex filaments are bent around the cylinder surface as can be seen in figure (41a) creating also a steady downwash along the sides of the cylinder. The vortex filaments are bent around the cylinder such that they align with the free stream direction, resulting in a convection of streamwise vorticity ω_x downstream. The streamwise vorticity is illustrated in the rear view of figure (41b).

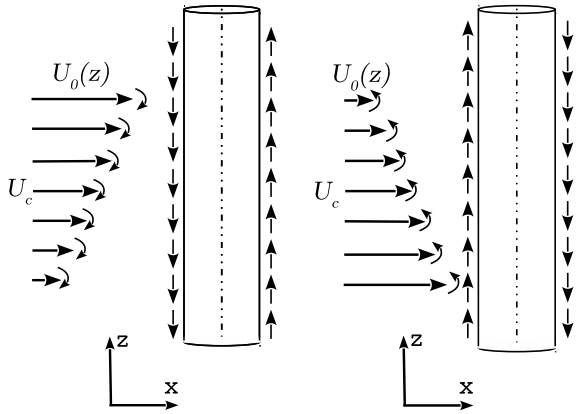

(a) SIDE VIEW (b) SIDE VIEW

Figure (40): Secondary flow along leading and trailing edge of a straight cylinder in case of: (a) Positive shear rate, and (b) Negative Shear rate. Vorticity being formed in the free stream is indicated in both cases. Figure inspired by (Zdravkovich 1997).

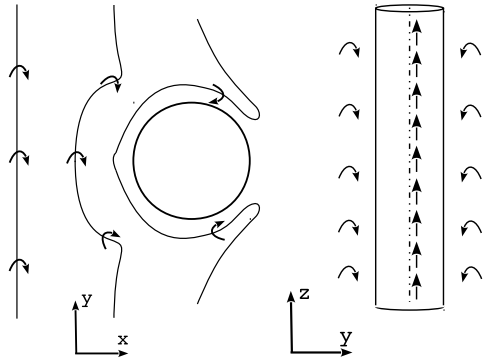

(a) TOP VIEW (b) REAR VIEW

Figure (41): (a) Vortex filements produced in the free stream at some spanwise location and being bent around the cylinder circumference. (b) Bent vortex filaments produce a downwash near the sides of the cylinder and are transported downstream as streamwise vorticity. Figure inspired by (Zdravkovich 1997).

6.1 S-series - Problem Description

The understanding of the non-uniform free-stream effect on marine structures is important for optimal design and thus a simple linear shear flow is considered in this section as a first step into non-uniform flow conditions on the curved concave cylinder configuration.

An inflow condition of a linear shear flow profile has been imposed in the concave flow direction (see figure (42)).

Parameter	
Configuration	Concave
L_h	$10D$
R	$12.5D$
L_v	$24D$
Inflow type	Spanwise Shear

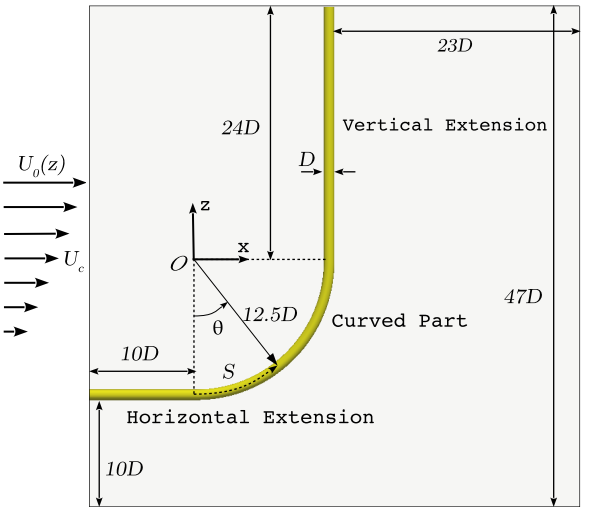

Figure (42): The configuration used for investigating shear flow. The geometrical configuration is the same M07-based grid (see section 4.2). A spanwise shear inflow is imposed at the inlet.

The shear profile imposed at the inlet boundary is represented mathematically by equation (49) with $U_0(z)$ being the inflow velocity in x-direction.

$$\frac{U_0(z)}{U_c} = K\frac{z+23}{D} + \frac{U_{bottom}}{U_c} \tag{49}$$

U_c is the flow profile median velocity occurring at $z/D = 0.5$ with its respective local Reynolds number Re_c, U_{bottom} is the velocity at the bottom of the domain,

in this case at $z/D = -23$ and K is the non-dimensional shear steepness according to equation (50).

$$K = \frac{dU_0(z)}{dz}\frac{D}{U_c} \tag{50}$$

The simulations are run on the same domain, grid and geometry as in the DNS comparison (section 5.1), that is the M07-grid from the grid study (section 4) only extended to a $24D$ vertical extension. The simulations were run $100U_c/D$ dimensionless time units with adjustable time step maintaining $Co_{max} = 5$. Furthermore data was logged for $1000U_c/D$ with a sampling period of $0.05U_c/D$. All simulations ensured a mean Courant number below ~ 0.1 and $Co_{max} \approx 3.5 - 5.0$. Instantaneous snapshots of the flow field are taken at $t^* = 1100U_c/D$.

To keep a relation to the flow conditions in section (5) a shear profile extending across the full height of the domain from $z/D = -23$ to $z/D = 24$ with extreme values of local Reynolds number being $Re_l = 200$ and $Re_l = 500$ is used.

This ensures that the grid used in the uniform flow cases earlier remains valid at least with respect to the inflow Reynolds number and that the wake flow dynamics should be comparable to the uniform inflow cases.

The values for the shear flow parameters are indicated in table (11), and it can be seen that when fixing the flow velocity extreme values and the height of the shear profile to the domain height $h/D = 47$ gives a shear steepness magnitude of $|K| = 0.0182$ in the cases S01 and S02. S01 and S02 represents the case of positive and negative shear rate respectively.

Additionally a stronger shear rate S03 was simulated. The shear profile has $K = -0.0236$, i.e. a stronger negative shear rate than S02. The shear rate results from setting $Re_l(z/D = -23) = 700$ and $Re_l(z/D = 24) = 200$.

Table (11): Shear flow parameters used in positive shear rate simulation (S01) and negative shear rate simulations (S02 and S03).

Case	U_{bottom}	Re_{bottom}	U_{top}	Re_{top}	U_c	Re_c	K
S01	2	200	5	500	3.5	350	0.0182
S02	5	500	2	200	3.5	350	-0.0182
S03	7	700	2	200	4.5	450	-0.0236

Whether the grid can handle the larger local Reynolds number imposed at the bottom is unknown and questionable, however the Renyolds number reduces to $Re_l \approx 604.3$ already at $z/D = -14$ which is $1D$ below the bottom of the horizontal extension. The simulations considered in the present study up to $Re = 500$ for the same configuration has shown that the flow remains laminar and non-shedding even up to $z/D = -4$. Thus the S03 flow configuration is considered reasonable, if not for a quantitative study, at least for the presentation of qualitative trends.

Another limitation applies for how the shear flow is applied in general. The introduction of three-dimensionality in the freestream itself poses a boundary issue. The question must be raised of whether the domain size is reasonable when the shear profile is extended from the bottom to top boundary, considering the free-slip wall boundaries. (Parnaudeau et al. 2007) omitted the bottom and top boundary condition issue by introducing a shear profile only partly along the inlet span. Extended uniform constant inflow conditions were used near the boundaries.

6.2 Results and Discussion - Shear Flow

In this section the results and findings of the shear flow cases are presented. The positive shear profile in S01 is considered first with comparisons to the uniform constant inflow conditions on the curved cylinder as well as references to past research on straight circular cylinders in a sheared free stream. The results of negative shear rate introduced in S02 and S03 are analysed with a basis in S01 and the uniform constant simulations C01 and C02.

It is perhaps beneficial as a reference for the reader that a sketch of the velocity profiles imposed at the boundary in each case is included. An overview of the three velocity profiles along with the resulting instantaneous snapshots of the wake topology illustrated by λ_2 (Jeong and Hussain 1995) in each case is found in figure (43).

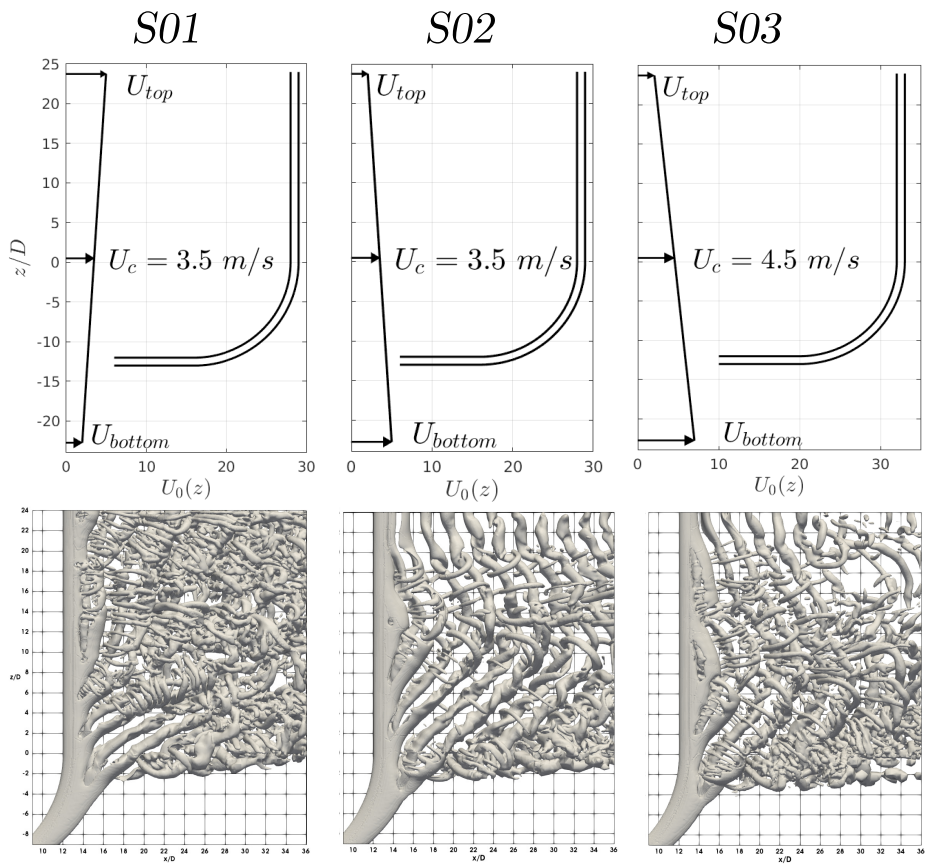

Figure (43): **Top Row:** The velocity profiles $U_0(z)$ imposed for S01, S02 and S03. Median velocity U_c is indicated at $z/D = 0.5$ for each simulation. The profiles are indicated relative to the cylinder, which is drawn to scale relative to the vertical position z/D. **Bottom Row:** Iso-surfaces of λ_2 (Jeong and Hussain 1995) for the three shear flow cases. From left to right: $\lambda_2 = -0.5$, S01; $\lambda_2 = -0.5$, S02; $\lambda_2 = -1$, S03.

Below in figure (44) and (45) the time averaged axial flow profiles are presented in the same manner as discussed previously in section (5) for the curved part and the vertical extension respectively. S01, S02 and S03 are all plotted together. As the freestream velocity is continuously varying along the cylinder, the tangential velocity component is now normalized on the median value U_c of the shear profile as U_{ax}/U_c. The normalization with respect to U_c applies in general in this section.

6.2.1 Increased Upwash in S01

The axial flow along the curved part for S01 is observed in figure (44) to be significantly lower than what is the case for S02. The velocity at the intersection with the horizontal extension at $\theta = 0°$ starts up at $U_{ax}/U_c \approx 0.73$ and $U_{ax}/U_c \approx 1.28$ for S01 and S02 respectively. This of course seems natural as the local Reynolds number occurring in the free stream at $z/D = -14$ are ~ 257.5 and ~ 442.7 for S01 and S02 respectively. However as the two profiles approach the intersection with the vertical extension at $\theta = 90°$, they match up exactly reaching a velocity of $U_{ax}/U_c \approx 0.8$.

All shear flows studied seems to experience a drop in axial velocity during the first interval of $\theta = 0° - 21°$, same as what was observed for the uniform flows C01 and C02 in section (5). After the initial drop the uniform flows and the shear flows all rise again to a maximum later in the region $\theta \approx 50° - 65°$. Figure (45) shows that S01 preserves this maximum as an almost constant line from $\theta = 65°$ to $z/D = 4$, whilst S02 experiences a monotonic decrease towards the top boundary. It is evident that some effect is driving the axial flow in S01 around $\theta \approx 70°$ to $z/D \approx 4$, overcoming the decrease in momentum experienced by S02 and the uniform flows.

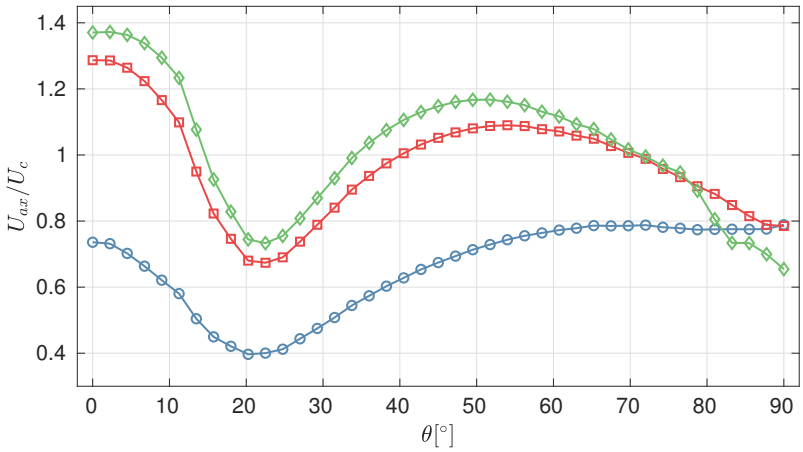

Figure (44): Variation of the time average of the axial velocity component U_{ax}/U_c along a concentric arc of the curved part which radius is $13.6D$, i.e. $0.6D$ behind the trailing edge of the curved cylinder. (—○—), S01; (—□—), S02; (—◇—), S03.

As with C01 ($Re = 200$), S01 shows a strong preservation of axial flow along the vertical extension. S01 preserves a $U_{ax}/U_c \geq 0.2$ all the way to $z/D = 22$ before dropping sharply towards the boundary. In this case this means that 20% of the local freestream velocity at $z/D = 0.5$ is found as a pure vertical velocity all the way up to $z/D = 22$. This is a large contribution considering that the local freestream in the region of the curved cylinder (below $z/D = 0$) is in general lower than U_c.

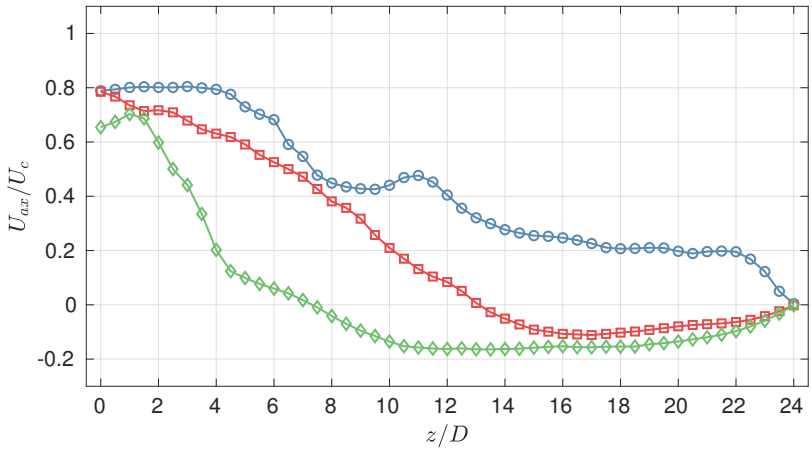

Figure (45): Variation of the time average of the axial velocity component U_{ax}/U_c along the span of the vertical extension at $x/D = 13.6$, i.e. $0.6D$ behind the trailing edge of the vertical cylinder. (—○—), S01; (—□—), S02; (—◇—), S03.

A likely parameter that is known to influence the flow in the way discribed is the pressure, and more specifically the pressure gradient in the domain. The phenomenon observed in S01 seems to be a result of a favourable pressure gradient[7]. The instantaneous pressure field is indicated for S01 and C01 in figure (46). The similar Re range around the curved part for the two cases leads to an unsurprising display of the same behaviour of a negative pressure gradient along the span on the trailing edge side.

[7]The effect of adverse and favourable pressure gradients are discussed in (White 2006)

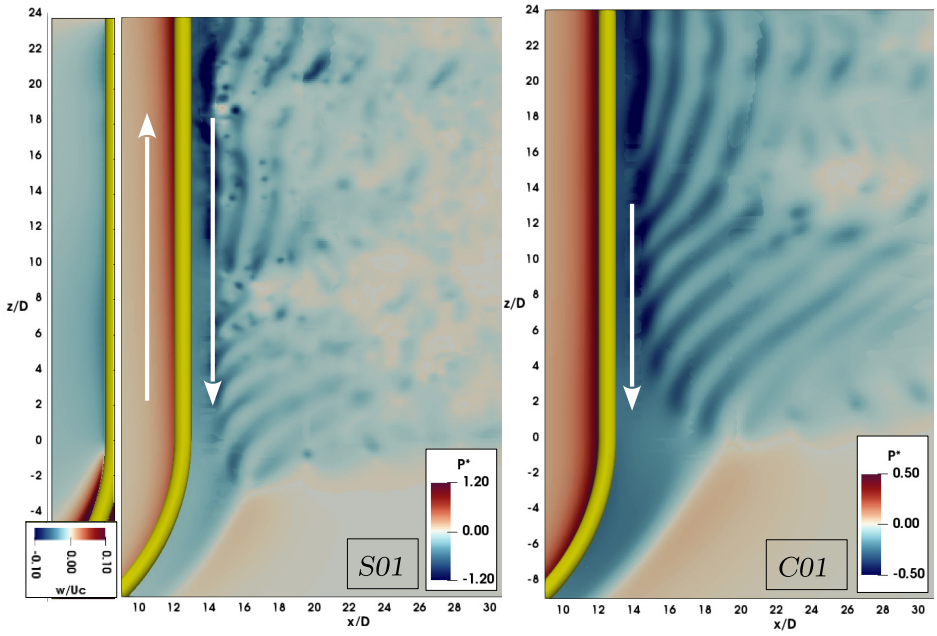

Figure (46): Instantaneous pressure field in the (x, z) centre plane. White arrows indicating direction and relative magnitude of spanwise pressure gradient. Arrows are not to scale nor based on a calculation of the gradient. $P^* = p/\rho U_c^2$ is the normalized pressure. **Left:** The S01 case with a positive shear rate in the freestream displaying strong spanwise pressure gradients along leading and trailing edge. A negative flow along the leading edge idicated in the far left plot. **Right:** The uniform flow case C01 at $Re = 200$ for comparison. A weaker spanwise pressure gradient along trailing edge and a visually uniform stagnation pressure distribution along the leading edge is shown.

The magnitude of the gradient however seems to be stronger in S01, as the contour colour indication in C01 is more uniform. Another feature of figure (46) indicates a stronger positive stagnation pressure gradient on the leading edge side in S01 compared to C01, and hence a slight negative flow along the span indicated by w/U_c to the far left in figure (46). These observations are in good qualitative agreement with effects of shear in the freestream on straight circular cylinders reviewed in (Zdravkovich 1997).

It is noticed in figure (45) that the axial flow along the vertical extension for S01 seems to be forced to abruptly decrease at $z/D = 22$ towards zero at the top boundary. This suggests that an investigation of the influence from the top

boundary condition is needed.

6.2.2 Influence of Downwash in S02 and S03

As discussed and shown in figure (44), the axial flow along the curved part in S02 shows similar trends as the uniform flows, and especially to the lower Re case C01. S03 also bears strong resemblance to S02 and the uniform flows in this region. The S02 and S03 does however deviate when the flow approaches the area known as the transitional region (section (5)) from around $\theta \approx 70°$. Here The S03 takes on characteristics found in the higher Re case C02 ($Re = 500$). At $z/D = -14$ a local Reynolds number of $Re_l \approx 442$ and $R_l \approx 604$ for S02 and S03 respectively. This means that the range of Re around the curved part in the two cases are very different in magnitude, and it seems to govern the onset of the transitional region in the intersection between the curved and vertical part.

In figure (45) the spanwise flow along the vertical extension can be compared for the cases S02 and S03. A strong decrease in vertical spanwise velocity is experienced for both cases, however S03 drops rapidly already at $z/D \approx 1.7$ going from $U_{ax}/U_c \approx 0.7$ to $U_{ax}/U_c \approx 0.1$ at $z/D \approx 4.5$. S02 decreases more slowly. In both cases axial flow velocity decreases monotonically towards a minimum at $z/D \approx 16.5$ and $z/D \approx 12.0$ for S02 and S03 respectively, taking on an average negative flow velocity. The negative trend persists all the way to the top boundary and is rather strong at the minima of $U_{ax}/U_c \approx -0.1$ and $U_{ax}/U_c \approx -0.18$ for S02 and S03 respectively.

Similarly as seen for the positive shear in S01, the velocity along the span is heavily altered. By exploring the instantaneous pressure distribution in figure (47) pressure gradients can be sketched as arrows.

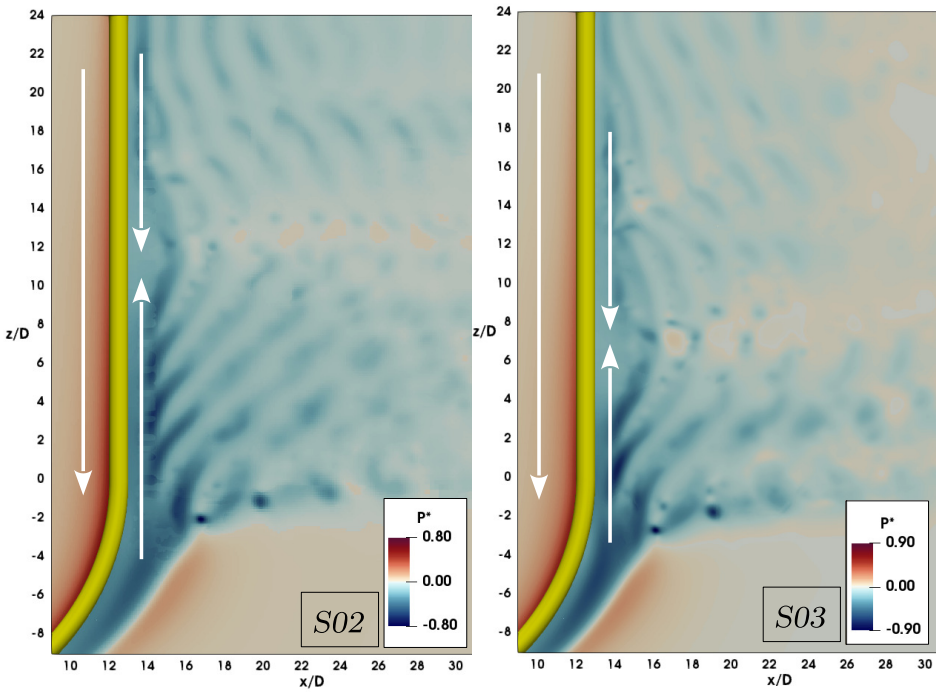

Figure (47): Instantaneous pressure field in the (x, z) centre plane. White arrows indicating direction of spanwise pressure gradient. Arrows are not to scale nor based on a calculation of the gradient. $P^* = p/\rho U_c^2$ is the normalized pressure. **Left:** The S02 case with shear rate $K = -0.0182$. **Right:** The S03 case with shear rate -0.0236.

The overall trends in pressure distribution and spanwise flow in S02 and S03 along the vertical extension matches what is predicted for shear inflow on straight cylinders. However, consentrating on the flow along the trailing edge side of the cylinder, the spanwise pressure gradient seems to change sign.

Furthermore in figure (48) the distribution of vertical velocity component w/U_c is plotted for S02 and S03. It can be observed that the upwash induced by the curved part is clearly suppressed by the downwash created by the freestream shear, and the stronger shear provides a stronger suppression.

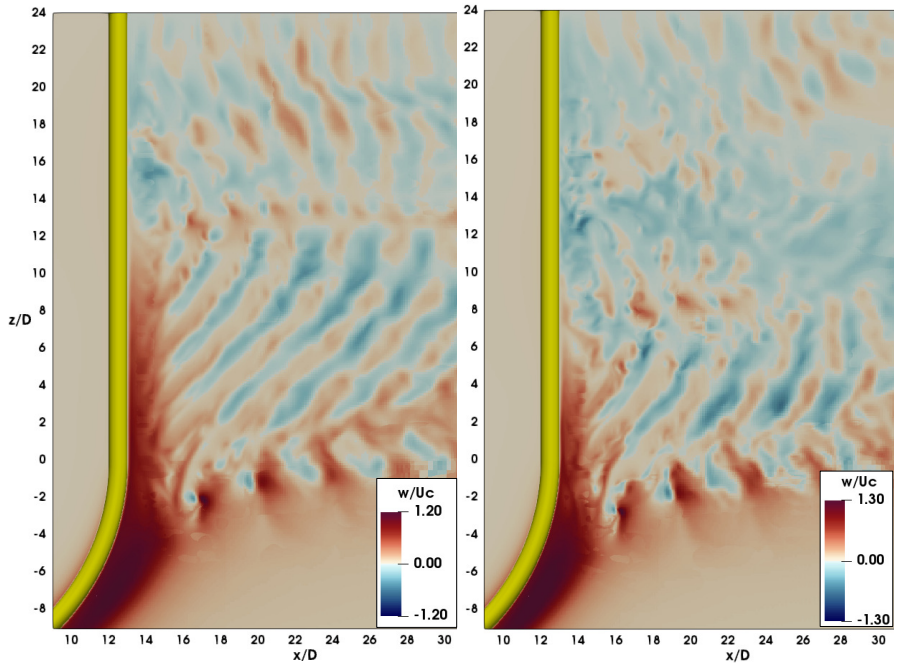

Figure (48): Instantaneous snpashot of the distribution of w/U_c in the (x, z) centre plane. The suppression of upwash from the curved part resulting from the induced downwash along the upper part of the vertical extension. **Left:** S02. **Right:** S03.

To clearly see the suppression of upwash by the shear flow, an instantaneous contour plot of three characteristic quantities of w/U_c can be seen in figure (49). On the next page in figure (50) the comparison of contour lines of instantaneous $w/U_c = 0.2$ is shown for all three shear cases, depicting the gradual induced suppression of upwash by changing the shear rate.

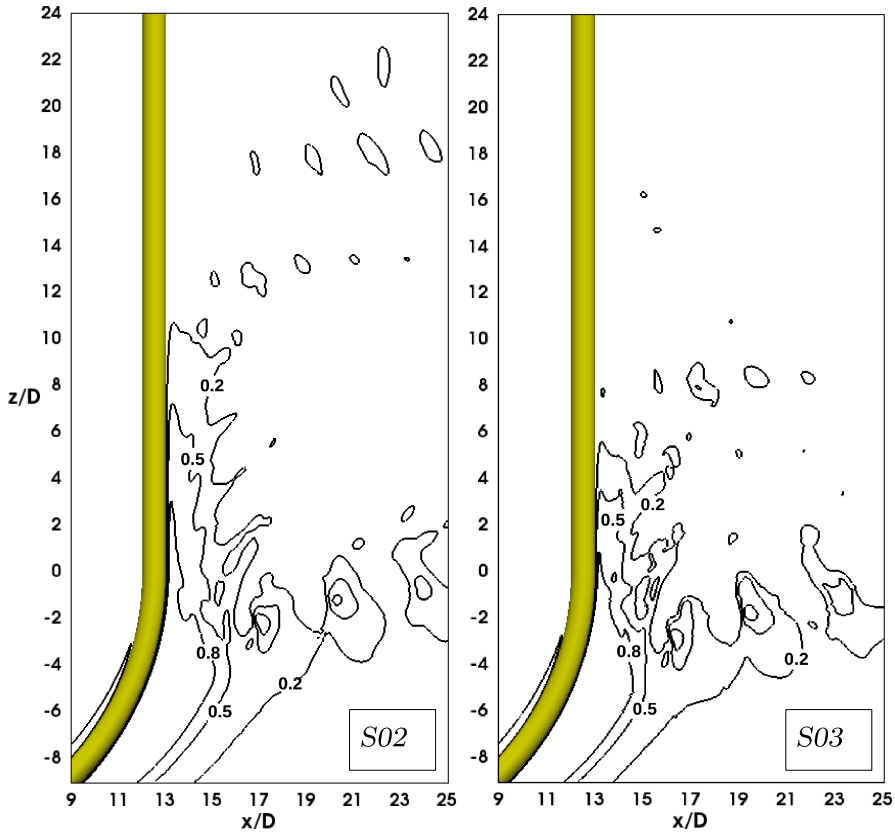

Figure (49): Contour lines of instantaneous distribution of $w/U_c = 0.2$, 0.5, 0.8. **Left:** S02. **Right:** S03.

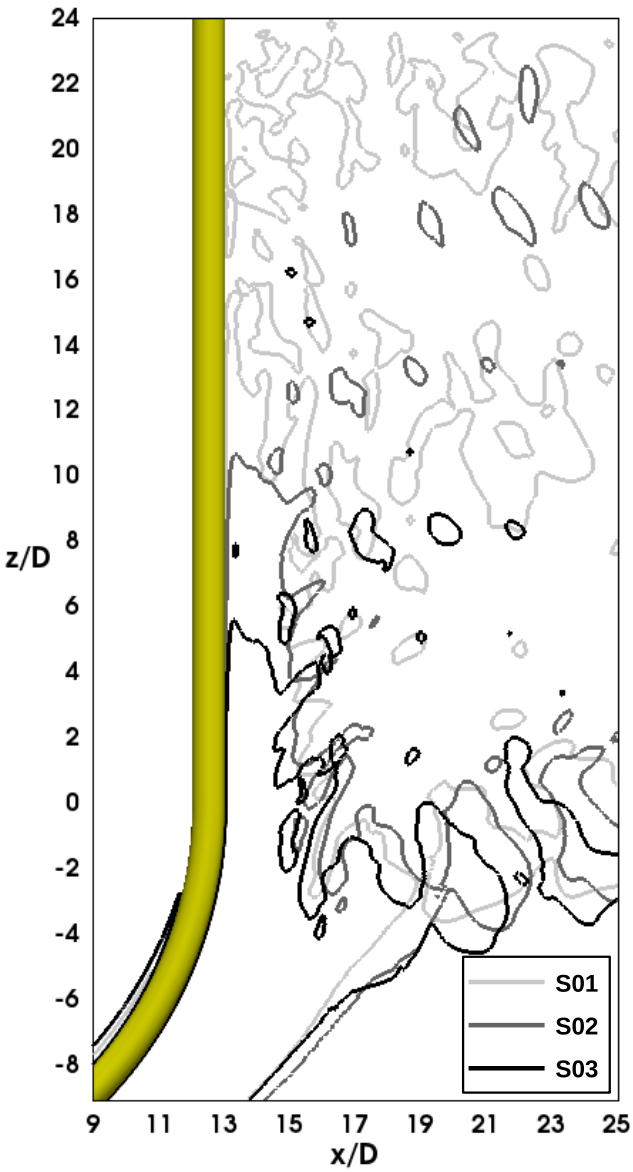

Figure (50): Contour lines of instantaneous distribution of $w/U_c = 0.2$ for all three shear flow cases. The lines are labeled by case names in the figure. S01 ($K = 0.0182$); S02 ($K = -0.0182$); S03 ($K = -0.0236$).

6.2.3 Shedding Regimes in S01

In figure (51) the shedding frequencies measured in the near wake for S01 is presented. It is extracted from the time series of v along a vertical line parallel to the vertical extension at $0.6D$ downstream of the cylinder. The frequencies are represented by normalized frequency f^* either based on U_c such that $f^* = f_c^* = fD/U_c$ or based on the local inflow velocity $U_0(z)$ such that $f^* = f_l^* = fD/U_0(z)$. An additional axis is added for reference to the local Reynolds number along the span $Re_l(z)$.

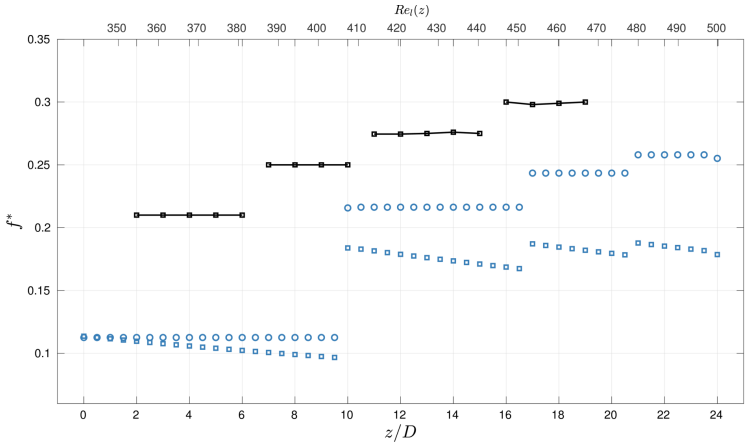

Figure (51): Strouhal number variation along span of the vertical extension for S01. The Strouhal frequency fD/U_c (○) based on the median inflow velocity U_c, and the Strouhal frequency $fD/U_0(z)$ (□) based on the spanwise varying inflow velocity $U_0(z)$. Reference Strouhal values fD/U_c (⊟) for a bluff body in uniform shear at $Re = 2.8{\cdot}10^4$, $K = 0.025$ (Maull and Young 1973).

Along with frequencies from S01 are data from (Maull and Young 1973). They found that the introduction of a continous linearly varying inflow does not result in a continuous frequency band. The shedding occurred in cells of constant frequency as indicated in figure (51). Looking back at figure (39) the values of f_l^* were found to vary within each cell however grouping around a single shedding frequency $f_l^* \approx 0.25$ related to the shedding frequency dominating in uniform flow.

In the present study a similar arrangement of shedding cells along the vertical extension can be observed, including also a variation of f_l^* within each cell. Only the upper three cells seem to have a grouping of f_l^* around a value of $f_l^* \approx 0.18$, and the first cell displays a significantly lower frequency. The group around $f_l^* \approx 0.18$ is in the region of $z/D = [10, 24]$ where $Re_l(z) \approx 410 - 500$. The uniform $Re = 500$ case of C02 showed a dominant shedding frequency in the upper part of the vertical extension of $f^* \approx 0.180 - 0.195$. Uniform inflows at lower Re exhibit slightly lower frequencies due to increased spanwise flow (F. Jiang, B. Pettersen, H. I. Andersson, et al. 2018), which might indicate that there is a local Reynolds number effect forcing the f_l^* around a shedding frequency similar to a uniform flow also for the curved cylinder problem.

For $z/D < 10$, the average of f_l^* lies at ~ 0.105. The Re_l is still quite large at $\sim 340 - 400$, and the $Re = 300$ uniform flow shows dominant frequency of $f^* = 0.122$ in this region (F. Jiang, B. Pettersen, H. I. Andersson, et al. 2018). The local Re analogy from the straight cylinder does not seem to hold close to the influence of the strong axial flow from the curved part and the transitional region.

Figure (52) relates the shedding frequencies observed in figure (51) to the wake topology illustrated by $\lambda_2 = -0.5$ (Jeong and Hussain 1995). The four shedding cells are illustrated along with an estimated location of the end of the non-shedding regime.

The occurrence of finer structures as in C02 is again apparent along the span, with streamwise vortices being formed in a way resembling mode-B type structures (C. Williamson 1996). The finer structures seems to be produced from as far up as $z/D \approx 4$, though transition seems to be apparent further downstream just above *regime 1*. Strong oblique shedding has an effect to postpone three-dimensional instabilities (C. Williamson 1996), therefore while mode B is observed up from $z/D \approx 4$, not even mode A is observed below this region.

In the lower part of *cell 1* clear slanted vortex cores are formed close to the cylinder. The vortex cores quickly exhibit instabilities when convected downstream where a wave pattern emerges along the cores resulting eventually in them break-

ing up.

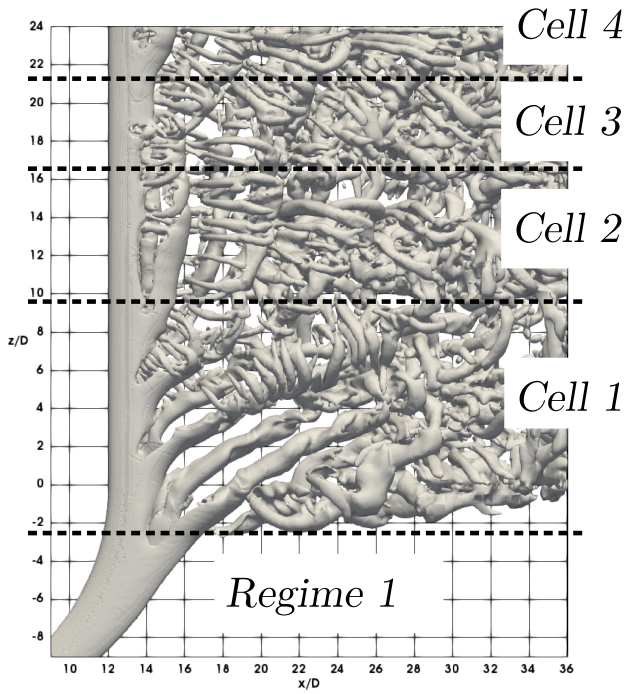

Figure (52): Plot of iso-surfaces of $\lambda_2 = -0.5$ (Jeong and Hussain 1995) for S01 indicating the shedding of vortices in cells along the span of the vertical extension. *Regime 1* being the non-shedding regime.

A more straight shedding occurs in *cell 2* and *cell 3* and *cell 4* show again more of an oblique shedding. Re_l is however in the range of 500 this far up and the problem of capturing details in the current numerical model arises.

6.2.4 Shedding Regimes in S02 and S03

The effect of a conflict between two spanwise flow regimes on the wake topology is clear in the plot of λ_2 in figure (53) for S02 and S03. The location where the downwash produced by freestream shear and the upwash from the curved cylinder meet is visible as a "bump" in the vortical structures. The location of the bump is observed to roughly coincide with the point of $U_{ax}/U_c = 0$ in figure (44) for S02 and S03.

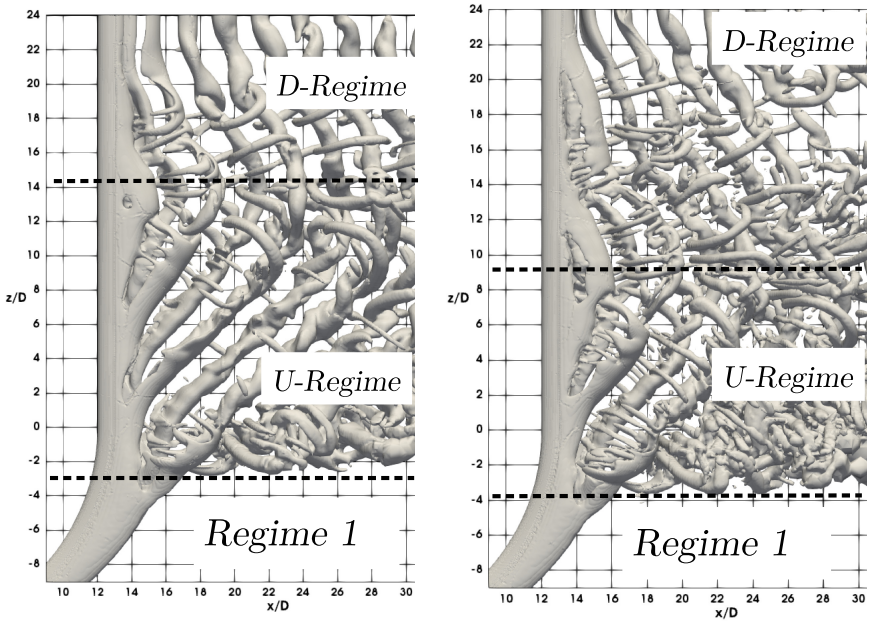

Figure (53): Plot of iso-surfaces of $\lambda_2 = -0.5$ (Jeong and Hussain 1995) for the negative shear rate simulations. The conflict between two spanwise flow regimes are evident in the vortical structures. The resulting regimes: *D-Regime* (downwash dominated); *U-Regime* (upwash dominated). Non-shedding regime *Regime 1* is indicated. **Left:** S02. **Right:** S03.

Two distinct regimes appear above and below the bump. They are named for convenience after which spanwise flow is dominant in the region, i.e. *U-Regime* where the upwash dominates and *D-Regime* where the downwash dominates. The boundary between them will be referred to as the "bump". It can be observed

that mode-A instabilities (C. Williamson 1996) seems to be characteristic of the bump region for S02 and finer streamwise vortices forms in addition in S03. In general S03 shows more finer structures than the S02, which is most likely due to a combination of a higher shear rate in the free stream and overall larger Reynolds number.

In figure (54) a tendency of a cell-like frequency distribution can be observed also for S02 and S03, as was seen in S01. The regimes set in figure (53) seems to posess a few characteristic behaviours when considering figure (54): The *U-Regime* is characterized by a constant shedding frequency until reaching the bump. The bump naturally displays the highest frequency over a short span. Directly after the bump there are cells of constant frequencies which gradually decrease towards a cell of lower constant frequency near the top boundary. Also the location of the bump shifts downwards as the shear rate increases as a consequence of the increased downwash from shear and a decreased upwash from the curved part. Additionally f_l^* groups around $f_l^* \approx 0.173$ and $f_l^* \approx 0.165$ for S02 and S03 respectively.

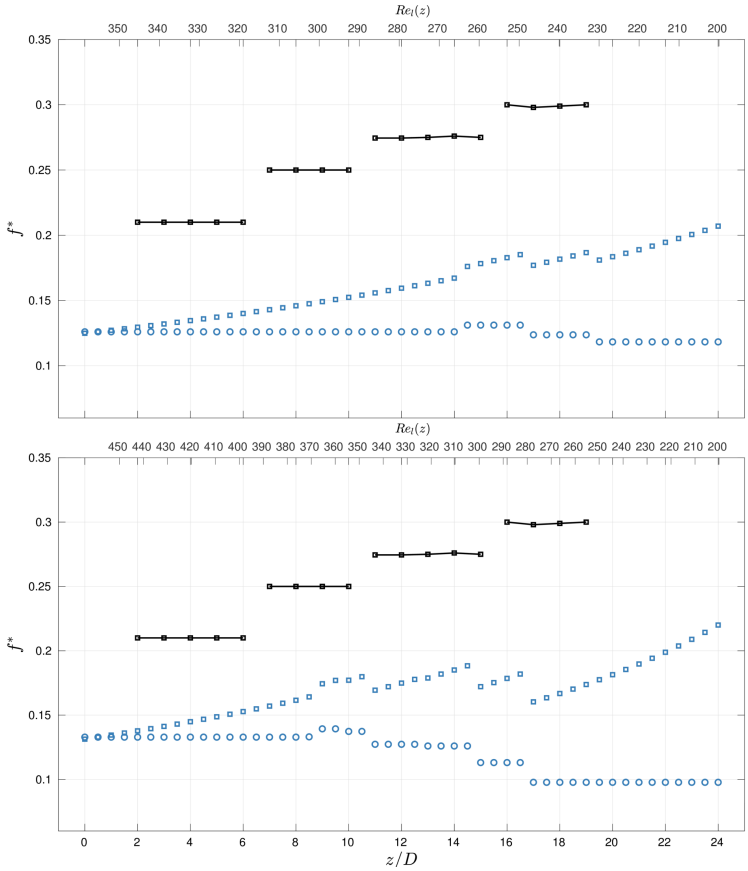

Figure (54): Strouhal number variation along the vertical extension. (○), fD/U_c; (□), $fD/U_0(z)$; (⊟), fD/U_c for a bluff body in uniform shear at $Re = 2.8 \cdot 10^4$, $K = 0.025$ (Maull and Young 1973). **Top:** S02. **Bottom:** S03.

6.3 General Thoughts and Further Work

- Furhter work: For further investigation of shear flow on the curved concave cylinder, a similar aproach as (Parnaudeau et al. 2007) could be utilized. Two constant flow conditions could be used near the top and bottom boundaries. To compare with this study the setup here could be extended by a longer L_v and extended distance b to lower boundary. The required extension of each length will likely depend on whether a positive or negative shear is introduced. Not a huge increase in computational effort if the same setup is used.

Blank Page

7 Conclusions

This thesis presents the development of a numerical model in SnappyHexMesh (SHM) (OpenFOAM 2018b) for use in the open-source CFD (Computational Fluid Dynamics) code OpenFOAM. SHM was found to be somewhat unpredictable with respect to proper generation of boundary layer grids. By experimentation with control parameters in SHM a suitable overall grid was found, however a perfect boundary layer grid was hard to obtain. This was found to be a contributor to limit the quality of the solution.

The model was verified by comparison with DNS (Direct Numerical Simulation) data obtained in an unpublished study (F. Jiang, B. Pettersen, H. I. Andersson, et al. 2018). The present model was found to reproduce overall wake flow dynamics found in DNS, however as the Reynolds number was increased details were lost due to a relatively much finer grid found in the DNS. Time averaged axial flow curves were compared with DNS for $Re = 200$ and $Re = 500$, where the former was reproduced well. Especially a transitional region near the intersection of the curved and vertical cylinder parts (F. Jiang, B. Pettersen, H. I. Andersson, et al. 2018) were found challenging for the present model at $Re = 500$. Furthermore shedding frequencies were underpredicted in the present model due to an overestimated extension of the axial flow velocity. Forces were found to be increasingly overpredicted and it was argued to be most likely an effect of grid resolution near the cylinder surface. A mode A-type instability (C. Williamson 1996) manifested itself in the region near the top boundary for $Re = 200$ most likely due to boundary condition effects. An oscillating vertical velocity near the boundary not found in DNS results was found to be a likely reason to trigger the instabilities. The vertical velocities related to the overprediction of axial flow is then a limitation of non-DNS analysis.

The effect of shear flow was investigated for positive and negative non-dimensional shear steepness $K = \pm 0.0182$ in addition the a stronger $K = -0.0236$. The positive shear rate lead to an increasing positive axial flow along the vertical extension due to upwash generated by a favourable pressure gradient along the cylinder span. This is a phenomenon occurring also for straight cylinders in shear

flow (Zdravkovich 1997). As for straight cylinders in shear inflow, a cellular shedding arrangement occurred in the wake with cells of different constant shedding frequencies. Unlike for straight cylinders a shedding region of significantly lower frequency was observed closer to the curved cylinder and was likely an effect of the stronger axial flow there.

The negative shear rates displayed a very different wake from the positive shear. The pressure gradient created by the freestream shear behind the cylinder changed sign creating thus a downwash along the vertical cylinder. The upwash inherent in the curved concave problem and the shear generated downwash was found to interact in a way that created a region of high frequency shedding along the span of the vertical part. The high-frequent shedding lead to a "bump" in the visualization of vortex cores in the wake which tended to be shifted downwards as the negative shear rate increased.

List of Figures

List of Tables

References

Assi, Gustavo R.S. et al. (2014). "Experimental investigation of the flow-induced vibration of a curved cylinder in convex and concave configurations". eng. In: *Journal of Fluids and Structures* 44, pp. 52–66. ISSN: 0889-9746.

Bearman, P. W. (1967). "The effect of base bleed on the flow behind a two-dimensional model with a blunt trailing edge." eng. In: *Aeronaut.* 18, pp. 207–224.

Canabes, Jose Patricio Gallardo (2010). *Direct Numerical Simulation of the Flow Past a Curved Circular Cylinder*. eng.

Çengel, Yunus A (2014). *Fluid mechanics : fundamentals and applications*. eng. 3rd ed. in SI units. Boston: McGraw-Hill. ISBN: 9781259011221.

Ferziger, Joel H (2002). *Computational methods for fluid dynamics*. eng. 3rd, rev. ed. Berlin: Springer. ISBN: 3540420746.

Fletcher, C. A. J (1991). *Computational techniques for fluid dynamics : 1 : Fundamental and general techniques*. eng. Berlin.

Gallardo, José P, Helge I Andersson, and Bjørnar Pettersen (2014). "Turbulent wake behind a curved circular cylinder". In: 742, pp. 192–229. ISSN: 0022-1120.

Gallardo, José P, Bjørnar Pettersen, and Helge I Andersson (2011). "Dynamics in the turbulent wake of a curved circular cylinder". In: *Journal of Physics: Conference Series* 318.6, p. 062008.

Gallardo, José P., Bjørnar Pettersen, and Helge I. Andersson (2013). "Effects of free-slip boundary conditions on the flow around a curved circular cylinder". eng. In: *Computers and Fluids* 86, pp. 389–394. ISSN: 0045-7930.

— (2014). "Coherence and Reynolds stresses in the turbulent wake behind a curved circular cylinder". eng. In: *Journal of Turbulence* 15.12, pp. 883–904. ISSN: 1468-5248.

Gaster, M. (1969). "Vortex shedding from slender cones at low Reynolds numbers". In: *Journal of Fluid Mechanics* 38.3, pp. 565–576. DOI: 10.1017/S0022112069000346.

Griffin, Owen M. (1985). "Vortex Shedding From Bluff Bodies in a Shear Flow: A Review". eng. In: *Journal of Fluids Engineering* 107.3. ISSN: 00982202.

Hanson, A. R (1966). "Vortex shedding from yawed cylinders". eng. In: *AIAA Journal* 4.4, pp. 738–740. ISSN: 0001-1452.

Harlow, Francis H. and J. Eddie Welch (1965). "Numerical Calculation of TimeDependent Viscous Incompressible Flow of Fluid with Free Surface". eng. In: *Physics of Fluids* 8.12, pp. 2182–2189. ISSN: 0031-9171.

Hayashi, T et al. (1992). "Turbulent structure in a vortex wake shed from an inclined circular cylinder". In: *Japan Society of Mechanical Engineers, Transactions B* 58.546, pp. 297–304.

Issa, R (1986). "Solution of the implicitly discretised fluid flow equations by operator- splitting". eng. In: *Journal of Computational Physics* 62, pp. 40–65. ISSN: 0021-9991.

Jeong, Jinhee and Fazle Hussain (1995). "On the identification of a vortex". eng. In: *Journal of Fluid Mechanics* 285.-1, pp. 69–94. ISSN: 0022-1120.

Jiang, F., B. Pettersen, and H. I. Andersson (2018). "Influences of upstream extensions on flow around a curved cylinder". eng. In: *European Journal of Mechanics / B Fluids* 67, pp. 79–86. ISSN: 0997-7546.

Jiang, F., B. Pettersen, H. I. Andersson, et al. (2018). "On the wake behind a concave curved cylinder". In: *Private Communication*.

Jiang, Hongyi et al. (2016). "Three-dimensional direct numerical simulation of wake transitions of a circular cylinder". In: *Journal of Fluid Mechanics* 801, pp. 353–391. ISSN: 0022-1120.

Kappler, M. et al. (2005). "Experiments on the flow past long circular cylinders in a shear flow". eng. In: *Experiments in Fluids* 38.3, pp. 269–284. ISSN: 0723-4864.

Maull, D. J. and R. A. Young (1973). "Vortex shedding from bluff bodies in a shear flow". In: *Journal of Fluid Mechanics* 60.2, pp. 401–409. DOI: 10.1017/S0022112073000236.

Miliou, A et al. (2007). "Wake dynamics of external flow past a curved circular cylinder with the free stream aligned with the plane of curvature". In: *Journal of Fluid Mechanics* 592, pp. 89–115. ISSN: 0022-1120.

OpenFOAM (2018a). *API Foam, Programmers Guide*. eng. URL: https://www.openfoam.com/documentation/cpp-guide/html/usergroup0.html.

OpenFOAM (2018b). *OpenFOAM v5 User Guide*. eng. URL: https://cfd.direct/openfoam/user-guide.

Parnaudeau, P. et al. (2007). "Direct numerical simulations of vortex shedding behind cylinders with spanwise linear nonuniformity". In: *Journal of Turbulence* 8, N13. DOI: 10.1080/14685240600767706. eprint: https://doi.org/10.1080/14685240600767706. URL: https://doi.org/10.1080/14685240600767706.

Patankar, Suhas V (1980). *Numerical heat transfer and fluid flow*. eng. Washington.

Pletcher, Richard H (2013). *Computational fluid mechanics and heat transfer*. 3rd ed. Series in computational and physical processes in mechanics and thermal sciences. Boca Raton, Fla: CRC Press. ISBN: 1591690374.

Ramberg, S. E. (1983). "The effects of yaw and finite length upon the vortex wakes of stationary and vibrating circular cylinders". eng. In: *Journal of Fluid Mechanics* 128.Mar, pp. 81–107. ISSN: 0022-1120.

Roache, Patrick J (1998). *Verification and validation in computational science and engineering*. eng. Albuquerque, N.M.

Sears, W.R. (1948). "The boundary layer of yawed cylinders". In: *J. Aero. Sci.* 15, pp. 49–52.

Shirakashi, M., S. Ueno, et al. (1984). "Vortex excited oscillations of a circular cylinder in uniform flow". In: *Bulletin of the JSME* 27.228, pp. 1120–1126. ISSN: 0021-3764.

Shirakashi, M., S. Wakiya, and A. Hasegawa (1986). "Effect of the Secondary Flow on Karman Vortex Shedding from a Yawed Cylinder". In: 29, pp. 1124–1128.

Slaouti, A. and J. H. Gerrard (1981). "An experimental investigation of the end effects on the wake of a circular cylinder towed through water at low Reynolds numbers". eng. In: *Journal of Fluid Mechanics* 112.Nov, pp. 297–314. ISSN: 0022-1120.

Smith, R. A., Woo Taik Moon, and T. W. Kao (1972). "Experiments on Flow About a Yawed Circular Cylinder". eng. In: *Journal of Basic Engineering* 94.4. ISSN: 00219223.

Sumer, B Mutlu (2006). *Hydrodynamics Around Cylindrical Structures (Revised Edition)*. Revised. Vol. v.26. Advanced Series on Ocean Engineering. River Edge: World Scientific Publishing Company. ISBN: 1-281-37328-1.

Tennekes, H (1972). *A first course in turbulence*. eng. Cambridge, Mass.

Tournier, Claude and Bernard Py (1978). "The behaviour of naturally oscillating three-dimensional flow around a cylinder". eng. In: *Journal of Fluid Mechanics* 85.1, pp. 161–186. ISSN: 0022-1120.

Vecchi, A. de, S.J. Sherwin, and J.M.R. Graham (2008). "Wake dynamics of external flow past a curved circular cylinder with the free-stream aligned to the plane of curvature". eng. In: *Journal of Fluids and Structures* 24.8, pp. 1262–1270. ISSN: 0889-9746.

Versteeg, H.K (2007). *An introduction to computational fluid dynamics : the finite volume method*. eng. 2nd ed. Harlow: Pearson/Prentice Hall. ISBN: 9780131274983.

White, Frank M (2006). *Viscous fluid flow*. eng. 3rd ed. McGraw-Hill series in mechanical engineering. Boston: McGraw-Hill Higher Education. ISBN: 9780072402315.

Williamson, C. H. K. (1989). "Oblique and parallel modes of vortex shedding in the wake of a circular cylinder at low Reynolds numbers". eng. In: *Journal of Fluid Mechanics* 206.-1, pp. 579–627. ISSN: 0022-1120.

Williamson, C.H.K. (1996). "Vortex dynamics in the cylinder wake". In: *Annual Review of Fluid Mechanics* 28, pp. 477–539. ISSN: 00664189.

Xu, Tianyu and John E. Cater (2016). "Numerical simulation of flow past a curved cylinder in uniform and logarithmic flow". eng. In: *Ships and Offshore Structures*, pp. 1–7. ISSN: 1744-5302.

Zdravkovich, M.M (1997). *Flow around circular cylinders : Vol. 1 : [Fundamentals]*. eng. Vol. Vol. 1. Oxford: Oxford University Press. ISBN: 0198563965.

— (2003). *Flow around circular cylinders : Vol. 2 : [Applications]*. eng. Vol. Vol. 2. Oxford: Oxford University Press. ISBN: 9780198565611.

Appendix

7.1 Grid Study

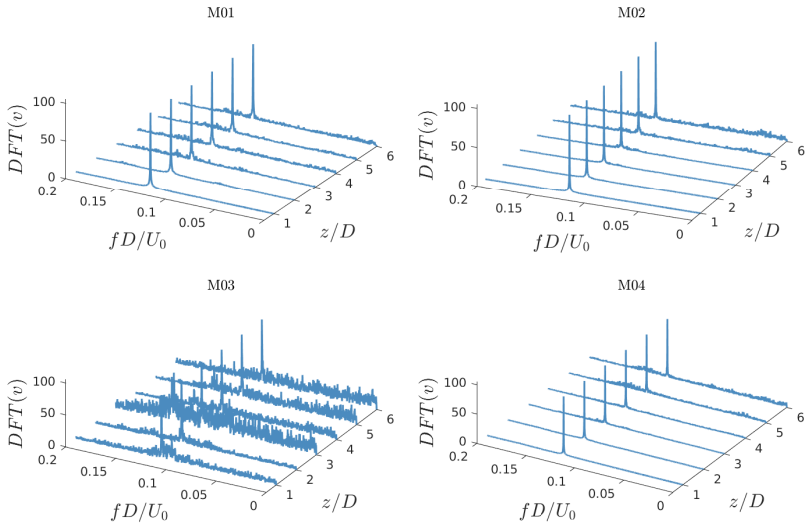

Figure (55): Frequency spectra obtained from a discrete Fourier transform of v in the near wake along the straight extension at $3D$ behind the cylinder trailing edge. For cases M01-M04.

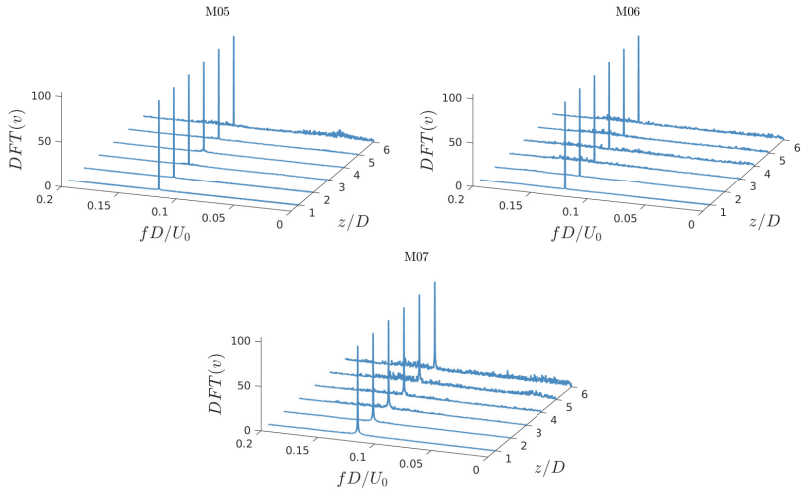

Figure (56): Frequency spectra obtained from a discrete Fourier transform of v in the near wake along the straight extension at $3D$ behind the cylinder trailing edge. For cases M05-M07.

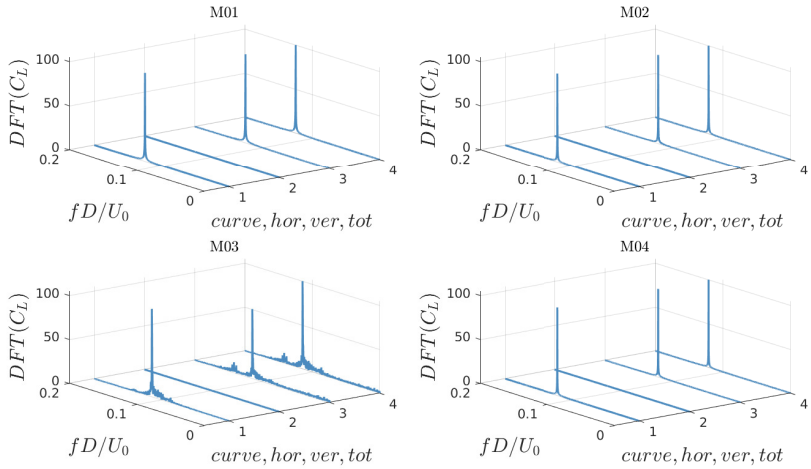

Figure (57): Frequency spectra obtained from a discrete Fourier transform of C_L for each cylinder part. The lines at $(1, 2, 3, 4)$ represents the frequency spectrum from the curved, horizontal, vertical and the total configuration repsectively. Showing spectra from case M01-M04 as indicated. Spectrum axis is normalized in % of maximum spectrum value.

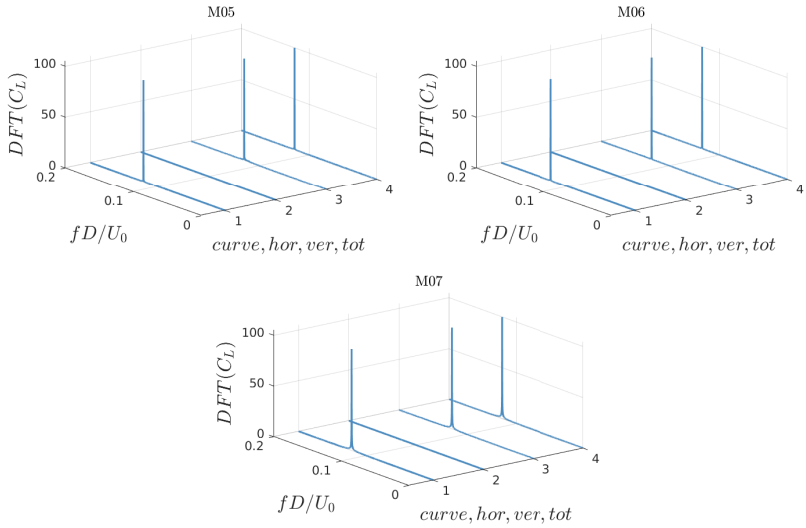

Figure (58): Frequency spectra obtained from a discrete Fourier transform of C_L for each cylinder part. The lines at $(1, 2, 3, 4)$ represents the frequency spectrum from the curved, horizontal, vertical and the total configuration repsectively. Showing spectra from case M05-M07 as indicated. Spectrum axis is normalized in % of maximum spectrum value.

7.2 Simulations - Shear Flow

7.2.1 Forces

Table (12): Results from the S-series force coefficient statistics and lift force frequency. $C_{L,rms}$ is the root-mean-square of the oscillating lift-force coefficient, $\overline{C_D}$ is the time averaged drag coefficient and f^*_{peak} is the dominating frequency of oscillation for the lift-force. Reference values included from the uniform flow cases C01 and C02.

Case	$C_{L,rms}$	$\overline{C_D}$	f^*_{peak}	Case	$C_{L,rms}$	$\overline{C_D}$	f^*_{peak}
S01	0.0629	1.2850	0.2580	C01	0.0216	1.0749	0.1680
S02	0.0335	0.8447	0.1183	C02	0.0640	1.0076	0.1946
S03	0.0369	0.7862	0.1329				

Table (13): Force analysis for S01, S02 and S03

		Curve	Horizontal	Vertical	Total
S01	$C_{L,rms}$	0.0066	0.0000	0.0628	0.0629
	$\overline{C_D}$	0.2327	0.0217	1.0305	1.2850
	f^*_{peak}	0.1126	0.1126	0.2580	0.2580
S02	$C_{L,rms}$	0.0129	0.0000	0.0323	0.0335
	$\overline{C_D}$	0.3396	0.0414	0.4637	0.8447
	f^*_{peak}	0.1260	0.1260	0.1183	0.1183
S03	$C_{L,rms}$	0.0308	0.0000	0.0257	0.0369
	$\overline{C_D}$	0.3508	0.0379	0.3975	0.7862
	f^*_{peak}	0.1329	0.1329	0.0978	0.1329